

Hydrodynamic Modeling, Optimization and Performance Assessment for Ducted and Non-ducted Tidal Turbines

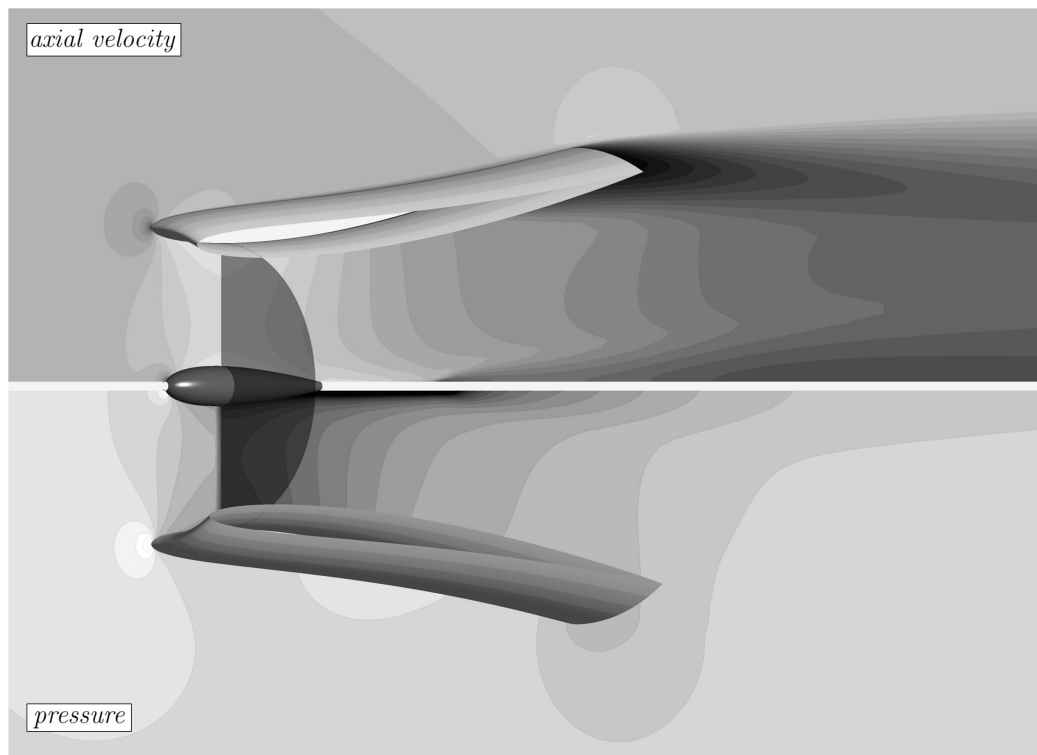
by

Michael Robert Shives
B.Eng., Carleton University, 2008

A Thesis Submitted in Partial Fulfillment of the
Requirements for the Degree of

MASTER OF APPLIED SCIENCE

in the Department of Mechanical Engineering



© Michael Shives, 2011
University of Victoria

All rights reserved. This thesis may not be reproduced in whole or in part, by photocopying or other means, without the permission of the author.

**Hydrodynamic Modeling, Optimization and Performance Assessment for Ducted and
Non-ducted Tidal Turbines**

by

Michael Robert Shives
B.Eng., Carleton University, 2008

Supervisory Committee

Dr. C. Crawford, Supervisor
(Department of Mechanical Engineering)

Dr. P. Oshkai, Departmental Member
(Department of Mechanical Engineering)

Supervisory Committee

Dr. C. Crawford, Supervisor
(Department of Mechanical Engineering)

Dr. P. Oshkai, Departmental Member
(Department of Mechanical Engineering)

ABSTRACT

This thesis examines methods for designing and analyzing kinetic turbines based on blade element momentum (BEM) theory and computational fluid dynamics (CFD). The underlying goal of the work was to assess the potential augmentation of power production associated with enclosing the turbine in an expanding duct. Thus, a comparison of the potential performance of ducted and non-ducted turbines was carried out. This required defining optimal turbine performance for both concepts. BEM is the typical tool used for turbine optimization and is very well established in the context of wind turbine design. BEM was suitable for conventional turbines, but could not account for the influence of ducts, and no established methodology for designing ducted turbines could be found in the literature. Thus, methods were established to design and analyze ducted turbines based on an extended version of BEM (with CFD-derived coefficients), and based on CFD simulation. Additional complications arise in designing tidal turbines because traditional techniques for kinetic turbine design have been established for wind turbines, which are similar in their principle of operation but are driven by flows with inherently different boundary conditions than tidal currents. The major difference is that tidal flows are bounded by the ocean floor, the water surface and channel walls. Thus, analytical and CFD-based methods were established to account for the effects of these boundaries (called blockage effects) on the optimal design and performance of turbines. Additionally, tidal flows are driven by changes in the water surface height in the ocean and their velocity is limited by viscous effects. Turbines introduced into a tidal flow increase the total drag in the system and reduce the total flow in a region (e.g. a tidal channel). An analytical method to account for this was taken from the field of tidal resource assessment, and along with the methods to account for ducts and blockage effects, was incorporated into a rotor optimization framework. It was found that the non-ducted turbine can produce more power per installed device frontal area and can be operated to induce a lesser reduction to the flow through a given tidal channel for a given level of power production. It was also found that by optimizing turbines for array configurations that occupy a large portion of the cross sectional area of a given tidal channel (i.e. tidal fences), the per-device power can be improved significantly compared to a sparse-array scenario. For turbines occupying 50% of a channel cross section, the predicted power improves by a factor of three. Thus, it has been recommended that future work focus on analyzing such a strategy in more detail.

Contents

Supervisory Committee	ii
Abstract	iii
Table of Contents	iv
List of Tables	vii
List of Figures	viii
Nomenclature	xii
Acknowledgements	xiv
Dedication	xvi
1 Introduction	1
1.1 Generating Power From the Tides	1
1.2 Using Ducts to Enhance Turbine Performance	2
1.3 Tidal Flows	5
1.4 Analysis Techniques	7
1.5 Key Contributions	9
1.6 Research Questions, Scope and Key Assumptions	9
1.7 Contextual Background	11
1.8 Thesis Organization	13
2 Model Development	15
2.1 Duct Geometries	15
2.2 Blade Element Momentum Theory For Non-Ducted Turbines	20
2.2.1 Derivation	20
2.2.2 Including Wake Swirl	23
2.2.3 Thrust and Power	24
2.2.4 Discrete Blade Effects	26
2.2.5 Implementation of BEM	27
2.2.6 Evaluation of Tip Loss for Non-Ducted Tidal Turbines	28

2.3	Blade Element Momentum Theory for Ducted Turbines	29
2.3.1	Literature Review	29
2.3.2	The 1D Duct Performance Model	30
2.3.3	Extending the Duct Model to Include Wake Swirl and Radial Variation	31
2.3.4	The Combined DuctBEM Model	32
2.3.5	Evaluating Turbine Performance for a Defined Blade	33
2.3.6	Optimizing the Blade Profile	35
2.4	Actuator Disk CFD Simulation	36
2.4.1	Software and Governing Equations	37
2.4.2	Turbulence Model	38
2.4.3	Momentum Source Terms	40
2.4.4	Simulation Domain and Boundary Conditions	43
2.4.5	Power, Thrust and Drag	44
2.4.6	Blade Properties	45
2.4.7	Mesh Definition and Grid Convergence	46
2.4.8	Initial Validation Studies	47
2.4.9	CFD-Based Blade Optimization Tool	49
2.5	Modeling Blockage and Free Surface Effects	51
2.5.1	Simulation Domain	52
2.5.2	Boundary Conditions	52
2.5.3	Simulation Setup	54
2.5.4	Computational Mesh	54
2.5.5	A New Analytical Treatment for Free Surface Effects	55
2.6	Method for Turbine Optimization in a Idealized Tidal Channel	59
2.6.1	Background	59
2.6.2	Literature Review	60
2.6.3	Methodology Overview	62
2.6.4	The Analytical Channel Model	62
2.6.5	Achievable Blockage Ratio	63
2.6.6	Accounting for Losses	64
2.6.7	Turbine Simulations	65
2.6.8	Tip Loss	67
2.6.9	Optimization of the Turbine Blades and Tip Speed Ratio	68
3	Application of the Models: Results and Discussion	69
3.1	Performance of Ducted Turbines with Ideal Rotors	69
3.1.1	Defining Extraction Efficiency	70
3.1.2	Results For Turbines with Equal Rotor Area	72
3.1.3	Results for Turbines with Equal Frontal Area	74
3.1.4	Sensitivity to Structural Drag and Tip Loss	75
3.1.5	Summary	77

3.2	Fitting Parameters for the Empirical Duct Performance Model	78
3.2.1	CFD Results	78
3.2.2	Fitting The 1D Empirical Duct Model	81
3.2.3	Boundary Layer Flow Control	84
3.2.4	Summary and Discussion	84
3.3	CFD-Based Blade Design: Sample Results	87
3.3.1	The Uniformly Loaded Case	87
3.3.2	Non-Uniform Loading Cases	87
3.3.3	Robustness of Design	88
3.3.4	Blade Geometry and Performance	89
3.3.5	Summary	91
3.4	Comparing the DuctBEM model to CFD Results	93
3.4.1	Baseline Turbine Performance	93
3.4.2	Simplified Duct Parameter Models	94
3.4.3	Optimum Blade	96
3.4.4	Summary	99
3.5	Free Surface Simulation Results	100
3.5.1	Sensitivity To the Location of the Dissipation Region	100
3.5.2	Effect of Free Surface Deformation on Power	101
3.5.3	Evaluating Free Surface Effects for Real-World Applications	103
3.5.4	Summary	103
3.6	Evaluating Optimal Power Extraction from a Real-World Tidal Channel	104
3.6.1	Turbine Power and Impact on the Tidal Flow	105
3.6.2	Extraction Efficiency	106
3.6.3	Economics	106
3.6.4	Turbine Design	108
3.6.5	Flowfield	111
3.6.6	Summary	113
4	Conclusions	115
4.1	Summary of the Work Done	115
4.2	Answers to the Research Questions	117
4.3	Recommendations for Future Studies	119
	Bibliography	121
A	Turbine Optimization Code	128
A.1	AUTORUN.m	128
A.2	process_header.cse	134
A.3	process.cse	134
A.4	output_blade.cse	136

List of Tables

Table 1.1	Timeline of milestones accomplished during this thesis work	11
Table 2.1	Summary of duct control parameters and resulting attributes	17
Table 2.2	Summary of the impact of tip loss on rotor thrust and power	28
Table 2.3	Grid convergence study results. The GCI indicates the estimated discretization error for each mesh.	47
Table 3.1	Regression model coefficients	82
Table 3.2	Summary of load optimization algorithm results for the D1 and D4 ducts. . .	88
Table 3.3	Sensitivity of C_P to the downstream location of the dissipation region boundary condition	100

List of Figures

Figure 1.1	Conceptual depiction of how a duct augments the mass flow through the turbine rotor	4
Figure 2.1	Duct geometric attributes used by the regression based model	16
Figure 2.2	Control parameters used to define the duct geometry	16
Figure 2.3	Duct area ratios and outlet angles.	17
Figure 2.4	Profiles of the duct geometries used in this thesis, scaled with constant duct length	18
Figure 2.5	Three-dimensional renderings of the ducts used in this thesis, scaled to have a constant rotor diameter	18
Figure 2.6	Diagram of relevant axial stations for ducted (top) and conventional (bottom) turbines ; 0) undisturbed freestream, 1) duct entry plane, 2) just upstream of the rotor, 3) just downstream of the rotor, 4) duct exit plane, 5) far wake and 6) very far wake.	21
Figure 2.7	Diagram of the relative velocity at a turbine blade section.	22
Figure 2.8	Depiction of dividing the flow using a series of concentric streamlines for determining the radial variation of η_{34} and $c_{p,b}$	32
Figure 2.9	duct and actuator disk	37
Figure 2.10	Blade flow angles and forces	42
Figure 2.11	Surface mesh near the duct/hub profile for the D4 duct	46
Figure 2.12	Comparison of CFD method to actuator disk theory for an ideal turbine with no duct	48
Figure 2.13	Comparison of present C_P to Hansen <i>et al.</i> [1] and effect of the gap on the baseline duct performance	49
Figure 2.14	Schematic describing the analytical free surface model parameters (reproduced from [2])	52
Figure 2.15	The effect of blockage ratio on power at $Fr = 0.22$: * denotes maxima at $Fr = 0.22$, \circ denotes maxima at $Fr = 0$. (reproduced from [2])	53
Figure 2.16	The domain and boundary conditions used for free surface simulations	53
Figure 2.17	Depiction of the wake and free surface deformation which occur when turbines operate near the water surface.	55
Figure 2.18	Flow parameters used in defining an analytical treatment for channel blockage effects	61

Figure 2.19	Image showing the maximum theoretical packing density for turbines in a single turbine fence.	64
Figure 2.20	Schematic of a tidal fence with turbines spaced at regular intervals. The flowfield is divided into a series of identical unit cells, which can be modeled using CFD simulation. The two images at the right show flow domains for un-ducted and ducted turbines.	65
Figure 3.1	Variation of duct drag coefficient with thrust coefficient for ducts D1 to D7 .	72
Figure 3.2	Variation of power coefficient with thrust coefficient for ducts D1 to D7 and for the ideal non-ducted turbine	73
Figure 3.3	Variation of extraction efficiency with thrust coefficient for ducts D1 to D7 and for the ideal non-ducted turbine	73
Figure 3.4	Depiction of separated flow region for ducts D1, D4, D5 and D7. The black region is where the flow is reversed	74
Figure 3.5	Power vs. thrust coefficient normalized by total projected frontal area	75
Figure 3.6	Variation of power and thrust coefficients with power loss coefficient, normalized by total projected frontal area	75
Figure 3.7	Variation of power and thrust coefficients with power loss coefficient, normalized by the total projected frontal area	76
Figure 3.8	Empirical model prediction of η_{34} (solid line) compared to CFD results for development cases D1-D7 (symbols)	79
Figure 3.9	Empirical model prediction of $C_{p,b}$ (solid line) compared to CFD results for development cases D1-D7 (symbols)	80
Figure 3.10	Empirical model prediction of C_P (solid line) compared to CFD results for development cases D1-D7 (symbols)	81
Figure 3.11	Correlation plots for diffuser efficiency (left) and base pressure coefficient (right); the solid line shows a 1:1 correlation	82
Figure 3.12	Empirical model prediction of η_{34} (solid line) compared to CFD results for validation cases V1-V3 (symbols)	83
Figure 3.13	Empirical model prediction of $C_{p,b}$ (solid line) compared to CFD results for validation cases V1-V3 (symbols)	83
Figure 3.14	Empirical model prediction of C_P (solid line) compared to CFD results for validation cases V1-V3 (symbols)	84
Figure 3.15	Axial velocity contours for duct D7 without, (top) and with (bottom) the gap between the actuator disk and duct surface. Note the higher velocity at the duct throat when the gap is present.	85
Figure 3.16	Contours of axial velocity for the D4 duct: Uniform loading with $C_T = 0.8$ (top), and non-uniform loading cases with $C_T = 0.80$, $C_{nu} = 1.3$ (middle) and $C_T = 0.85$, $C_{nu} = 1.3$ (bottom).	88
Figure 3.17	Determined optimal blade properties for the D1 and D4 ducts	89
Figure 3.18	Optimal local thrust and power coefficients for the D1 and D4 ducts	90

Figure 3.19	Induction factors for the optimal configurations for the D1 and D4 ducts . . .	91
Figure 3.20	Radial variation of η_{34} , $c_{p,b}$ and $c_{p,sw}$ as calculated from CFD simulation results for the optimized rotor from section 3.3 for the D4 duct	94
Figure 3.21	Results of the DuctBEM model using the radially varying $c_{b,p}$ and η_{34} extracted for the specific duct and rotor loading, compared to CFD results for the same configuration.	95
Figure 3.22	Errors in axial induction and angle of attack when using simplified representations of $c_{p,b}$ and η_{34}	96
Figure 3.23	Errors in local thrust and power coefficients when using simplified representations of $c_{p,b}$ and η_{34}	97
Figure 3.24	Optimal determined blade geometries and performance metrics.	98
Figure 3.25	The free surface profile predicted from simulations for a range of dissipation region downstream distances $x = \{10, 15, 20\}$	101
Figure 3.26	Comparison of analytical models for the effect of free surface deformation on turbine power to the CFD results for a range of C_T	102
Figure 3.27	Comparison of analytical models for the free surface deformation to the CFD results ($B_r = 0.5$, $C_T = 3.0$)	102
Figure 3.28	Comparison of analytical models for the free surface deformation to the CFD results for a range of C_T	102
Figure 3.29	Satellite image of Minas Passage and surrounding area ©Google (modified to be greyscale, labels added manually)	104
Figure 3.30	Variation of optimal turbine power (left) and resulting total power dissipation (right) with blockage ratio	105
Figure 3.31	Variation of tidal amplitude change in Minas Basin with blockage ratio (when turbines are optimized for maximum power production)	106
Figure 3.32	Variation of extraction efficiency with optimal turbine power generation (left) and variation of optimal turbine power generation with total power dissipation (right). The labels show the blockage ratio of selected data points.	107
Figure 3.33	Effect of reducing thrust coefficient of non-ducted turbine for a blockage ratio of $B_r = 0.6$. When C_T is reduced such that non-ducted turbine efficiency is equal to that of the ducted turbine, the non-ducted turbine power production is significantly higher than the ducted turbine.	107
Figure 3.34	Power produced per square meter occupied by turbines plotted against blockage ratio	108
Figure 3.35	Variation of thrust coefficient (left) and tip speed ratio (right) with blockage ratio, for maximum power production	109
Figure 3.36	Variation of optimal blade chord ratio with increasing blockage (left) and percent change in the chord ratio from the 10% blockage case (right)	110
Figure 3.37	Variation of optimal blade twist angle with increasing blockage (left) and change in the twist from the 10% blockage case (right)	110

Figure 3.38 Contour plots of the axial velocity near the turbine actuator disk. The actuator disk location is shown by the narrow rectangle, and the assumed turbine hub is clearly visible. Vectors are shown to indicate the flow direction . . . 112

Nomenclature: Latin

a	axial induction factor	f_x	axial force on an annulus
a'	tangential induction factor	f_θ	tangential force on an annulus
a_b	amplitude of tide in a basin	F_r	Froude number
a_t	amplitude of tidal forcing	F_x	axial force
A	area	g	acceleration due to gravity
A_1/A_3	inlet contraction ratio	h	water height
A_4/A_3	diffuser expansion ratio	I	turbulence intensity
A_b	basin surface area	J	objective function
A_r	rotor area	k	turbulent kinetic energy (TKE)
B	number of blades	k_t	thickness scaling parameter
B_r	blockage ratio	l	lift per unit span
c	chord length	$\frac{l}{d} = \frac{c_l}{c_d}$	lift-to-drag ratio
c_d	drag coefficient	L	lift force
c_{eq}	equality constraint	L_d	duct length
c_g	channel geometry parameter	\dot{m}	mass flow
c_l	lift coefficient	M_P	productivity metric
c_P	local power coefficient	N	number of nodes
c_T	local thrust coefficient	p	pressure
c_x	axial force coefficient	p_0	freestream pressure
c_θ	tangential force coefficient	p_v	vapour pressure
$c_{p,02}$	inlet pressure coefficient	Q	volume flow rate
$c_{p,34}$	diffuser pressure coefficient	r	radial position
$c_{p,b}$	base pressure coefficient	r_r	radius of the blade root
$c_{p,sw}$	swirl pressure coefficient	R	rotor radius
C_D	drag coefficient	R_a	tidal amplitude ratio
C_{D2}	drag coefficient using frontal area	Re	Reynolds number
C_{nu}	non-uniform loading coefficient	S_x	axial momentum source
C_P	total power coefficient	S_θ	azimuthal momentum source
C_{P2}	power coefficient using frontal area	t_d	actuator disk thickness
C_{Plost}	power dissipation coefficient	T	rotor thrust force
C_{Plost2}	power dissipation coefficient using frontal area	u'_i	average magnitude of turbulent fluctuation
C_T	total thrust coefficient	u	velocity
C_{T2}	thrust coefficient using frontal area	u_x	axial velocity
d	drag per unit span	u_θ	tangential velocity
D	drag force	w	relative velocity at the blade
f_p	Prandtl tip loss factor	x	axial position

Nomenclature: Greek

α	angle of attack	θ_2	duct airfoil incidence parameter
β	blade twist angle	$\theta_{4,in}$	inner diffuser exit angle
β_g	channel-basin geometry parameter	$\theta_{4,out}$	outer diffuser exit angle
γ	drag term	λ	tip speed ratio
γ_0	channel natural drag term	μ	normalized radius
γ_1	turbine drag term	ν	kinematic viscosity
γ^*	non-dimensional drag term	ν_t	kinematic eddy viscosity
$\delta_{i,j}$	Kronecker delta	ρ	fluid density
Δ	change in...	σ	rotor solidity
ϵ	TKE dissipation rate	σ_c	cavitation number
ζ	sea surface height	τ	bypass flow velocity ratio
η_{02}	inlet efficiency	τ_w	wall shear stress
η_{34}	diffuser efficiency	ϕ	inflow angle
η_{ex}	extraction efficiency	ω	specific dissipation of TKE
θ	azimuthal position	ω_t	frequency of tidal forcing
θ_1	duct airfoil camber parameter	Ω	rotor angular speed

ACKNOWLEDGEMENTS

I would like to thank:

Dr. Curran Crawford: His mentoring, support, encouragement, and patience contributed enormously to the quality of the research conducted and of the resulting publications, including of course, this thesis. Curran's dedication to his students is remarkable.

My wonderful girlfriend, Josée Laroche: Her moral support and encouragement gave me the fortitude to commit the required time and effort to complete this work, while her naturally active lifestyle provided necessary balance to my life.

My office mates, Michael McWilliam, and Stephen Lawton: They offered many interesting discussions and contributed a good deal of technical advice that made a significant contribution to the thesis.

Dr. Nedjib Djilali: His expertise in the field of turbulence modeling in computational fluid dynamics was invaluable.

Dr. Jody Klymak: Taking his course in physical oceanography provided me with essential background knowledge and set the context for this thesis work.

The Natural Sciences and Engineering Research Council of Canada (NSERC), The University of Victoria, and The Pacific Institute for Climate Solutions (PICS), for their generous funding throughout my studies.

There is a widely used notion that does plenty of damage: the notion of “scientifically proven”. Nearly an oxymoron. The very foundation of science is to keep the door open to doubt. Precisely because we keep questioning everything, especially our own premises, we are always ready to improve our knowledge. Therefore a good scientist is never ‘certain’. Lack of certainty is precisely what makes conclusions more reliable than the conclusions of those who are certain: because the good scientist will be ready to shift to a different point of view if better elements of evidence, or novel arguments emerge. Therefore certainty is not only something of no use, but is in fact damaging, if we value reliability.

Failure to appreciate the value of the lack of certainty is at the origin of much silliness in our society. Are we sure that the Earth is going to keep heating up, if we do not do anything? Are we sure of the details of the current theory of evolution? Are we sure that modern medicine is always a better strategy than traditional ones? No we are not, in none of these cases. But if from this lack of certainty we jump to the conviction that we better not care about global heating, that there is no evolution and the world was created six thousand years ago, or that traditional medicine must be more effective than the modern medicine, well, we are simply stupid. Still, many people do these silly inferences. Because the lack of certainty is perceived as a sign of weakness, instead of being what it is: the first source of our knowledge.

Every knowledge, even the most solid, carries a margin of uncertainty. (I am very sure about my own name ... but what if I just hit my head and got momentarily confused?) Knowledge itself is probabilistic in nature, a notion emphasized by some currents of philosophical pragmatism. Better understanding of the meaning of probability, and especially realizing that we never have, nor need, ‘scientifically proven’ facts, but only a sufficiently high degree of probability, in order to take decisions and act, would improve everybody’s conceptual toolkit.

Carlo Rovelli
Physicist, University of Aix-Marseille, France

DEDICATION

I dedicate this thesis to my grandmother, Mavis Piper. She understood the value of conserving and nurturing our precious environment and of using only what we need long before there was any talk of climate change, global warming or an energy crisis.

Chapter 1

Introduction

1.1 Generating Power From the Tides

With growing concerns about the impact of greenhouse gas emissions on the global climate, there is a pointed effort to promote the development and deployment of carbon-free and carbon-neutral electricity generation technologies. This includes promoting the proliferation of relatively mature technologies such as nuclear plants, photovoltaics and wind turbines, as well as the development of novel generation strategies. Over the last two decades, there has been a great deal of work towards developing technologies to extract energy from the tides. This is an attractive proposition because unlike solar power and wind, the tides are predictable with very high accuracy many years in advance. The tides are, of course, cyclical in nature, being governed by the gravitational pull of the moon and sun on the Earth's oceans. The predictability of tidal power production could play an important role in stabilizing electrical grids as they move towards increased penetration of less predictable wind and solar power.

The concept of extracting power from tidal energy has existed for centuries [3], with early tide mills generating mechanical power for grinding grain. In modern times, extracting power from the tides has been accomplished almost exclusively using tidal barrages such as the 240MW La Rance barrage in France, developed in 1966 and more recently, the 254MW Sihwa Lake barrage in Korea, which was opened in 2011. It has been argued that barrage schemes have an unacceptable environmental impact because they significantly reduce the amplitude of the tides and the flushing rate of the basin on the inland side of the barrage. These changes are detrimental to marine life in inter-tidal regions and can lead to excessive buildup of pollutants and silt in the basin. Additionally, the bulb turbines used in barrage schemes typically operate at high speed which can lead to high mortality rates for fish passing through the turbine. Barrage schemes also require enormous capital costs associated with the amount of material, time and the logistical difficulties of building in a dynamic marine environment. Both the environmental impact and capital costs are often cited as deterrents to tidal barrage schemes [4–7]. The environmental impact of barrages may not always be as negative as perceived, however. Rourke *et al.* [7] mention that sediment transport changes due to barrages may allow marine life to flourish in areas where it otherwise would not. Also, in the

case of the Sihwa Lake barrage, the enclosed basin had previously been isolated from the ocean by a seawall, allowing pollution to build up excessively. Building the turbines and sluice gates restored enough flushing to the basin to improve the water quality drastically [8].

In any case, the opposition to barrages on the grounds of environmental impact and capital cost have led to the development of turbines which operate by converting available kinetic energy in tidal flows into useful power. In this thesis the term *kinetic turbines*¹ is used to refer to such devices. Kinetic turbines operate with little head difference, relying instead on the flow velocity to turn the rotor. This restricts their deployment to sites where sufficiently high tidal flow speeds occur, which requires certain bathymetric features such as a channel connecting a basin to the ocean. Since they do not require a large head difference to operate, kinetic turbines do not require barrages, which alleviates issues associated with reduced basin tidal amplitude and flushing. They can also operate at much lower speeds than bulb turbines, reducing fish mortality issues [9]. They can be deployed as single turbines, in sparse arrays, or in fences spanning entire channels. This flexibility allows for an incremental development approach, allowing the generation of some revenue before committing to immense capital costs. From an investment perspective, this is much more attractive than the high capital cost and long payback period of tidal barrages.

Several conceptual designs exist for tidal kinetic turbines. Axial flow turbines have their rotational axis aligned with the flow direction, and have seen widespread use in wind power. Tidal flows always reverse direction during the tidal cycle, and to operate on both ebb and flood tides, axial flow turbines must either yaw the entire rotor by $\approx 180^\circ$, pitch the blades by 180° (and reverse the rotation direction) or use blades designed to operate in bi-directional flows. Cross flow turbines have their rotational axis perpendicular to the flow direction, and therefore do not require specific design features to operate in bi-directional flows. They also sweep out a rectangular cross sectional area (as opposed to a circle for axial flow turbines) which could allow for a greater packing density of turbines in a given tidal channel. Cross-flow turbines inherently have a lower aero/hydro-dynamic efficiency, which mitigates against these advantages. Because of this, cross flow turbines have had very little success in the wind power industry. The dominant design for tidal power also seems to be the axial flow turbine. For this reason, this thesis considers only the axial flow turbine concept. Some turbine concepts enclose the turbine in a duct, which increases the power production of the turbine for a given rotor diameter. Developers of non-ducted turbines have argued that ducted turbines do not offer a cost-effective performance advantage. This debate is the primary focus of this thesis.

1.2 Using Ducts to Enhance Turbine Performance

The primary focus of this thesis is to determine if using ducts to enhance the performance of turbines is a logical design strategy in the context of tidal power generation. The concept of ducted (or diffuser augmented) turbines has been studied in the context of wind power for decades, but with no commercially successful designs to date. More recently, a few ducted tidal turbine concepts have

¹In this thesis, the term *kinetic turbines* refers to any turbines which convert the kinetic energy of the flow to useful power (as opposed to head-driven turbines more typical of tidal barrages or hydro dams). The term kinetic is applied to turbines used for generating power in rivers, tidal currents, ocean currents and atmospheric wind

gone through the prototype stage and are nearing commercial deployment. The first in depth study of ducted turbines was done in the context of wind power by Lilley and Rainbird [10], who developed analytical models based on one-dimensional momentum theory and potential flow methods in the 1950s. Their study suggested that a reasonable duct could provide at least a 65% increase in power over an ideal unshrouded turbine with the same rotor diameter. Literature on ducted turbines was sparse until the 1970s when researchers from Grumman published a series of papers presenting a simplified one-dimensional semi-empirical model [11] and a series of experiments using wire meshes to represent the turbine, [11–13] as well as with an actual turbine [13] with a wide range of diffuser geometries. The Grumman researchers focused on using short ducts with a large expansion to reduce the overall cost of the duct and structures. These studies identified a 90% [12] power enhancement over the non-ducted case from experimental results. The Grumman researchers identified that flow separation was a limiting factor in duct performance and therefore used a slotted diffuser design for boundary layer flow control.

More recently, in the 1990s, a New Zealand company called Vortec attempted to commercialize a ducted wind turbine design [14, 15], but the project was scrapped when their seven-meter prototype did not perform as well as expected. Attempts to develop ducted wind turbines have been unsuccessful for a number of reasons, the most important of which is arguably the immense loading on the duct in storm conditions or in yawed flows. The Vortec turbine design needed heavy support structures to take the loads expected in storm conditions. Additionally, a yawing mechanism for the entire duct/turbine system was required, increasing complexity and cost. The failure of the Vortec turbine project gave strong evidence that in the context of wind turbines, the power augmentation provided by a duct could be achieved at lower cost by simply extending the rotor diameter.

There is renewed interest in ducted turbines in the context of tidal power generation since the direction and magnitude of tidal flows are quite predictable and tidal turbines would not be subject to such extreme storm loads as wind turbines. Nevertheless, depending on the deployment depth; storm surges; highly turbulent flow; wave action; and asymmetric ebb-flood tides, tidal flows can produce significantly higher loadings than the pure gravitationally-forced tides and should be studied in detail on a site-specific basis. The duct design for tidal turbines is typically bi-directional to avoid the need for a yawing mechanism. This requires special considerations in blade and duct design to ensure the turbine can operate on both ebb and flood tides. In this thesis, uni-directional ducts have been considered to allow comparison to previous numerical studies [1] and to provide an optimistic estimate of duct performance. It is expected that bi-directional ducts will have lower performance than uni-directional ones due to stagnation regions and/or flow separation from a relatively sharp leading edge. Kinetic turbines located in rivers and ocean currents could make direct use of the unidirectional ducts examined in this thesis.

There are a number of companies at the prototype stage in their development of ducted tidal turbines. Ireland’s OpenHydro has conducted tests with a high-solidity ducted turbine in the Bay of Fundy. Alstom (France) is developing a ducted turbine based on a design by Clean Current (Canada) also to be tested in the Bay of Fundy in 2012. Lunar Energy (Scotland) and several other companies are also developing similar designs. Despite significant development of ducted tidal turbine designs by several organizations, there is a lack of literature defining methods for the hydrodynamic analysis

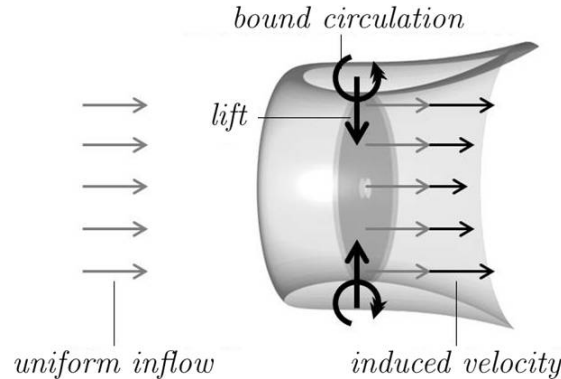


Figure 1.1: Conceptual depiction of how a duct augments the mass flow through the turbine rotor

and optimization of ducted turbines. One of the goals of this work was therefore to develop and publish methods for this purpose that were not too computationally expensive for use in an iterative design methodology. Optimization of ducted designs was required in any case to compare ducted and non-ducted turbine performance to assess the efficacy of ducts for tidal turbines.

From a physical point of view, the typical rationale behind incorporating a duct is to increase the extracted power by increasing the velocity of the flow through the rotor. In a CFD study of a simplified ducted turbine, Hansen *et al.* [1] demonstrated that the increase in power due to the duct (for a fixed rotor area) is in fact proportional to the increased mass flow through the rotor. There are a variety of explanations for how this occurs. One explanation is that the duct forces an expansion of the flow downstream of the turbine beyond that which is possible for an open rotor. This provides a reduced pressure on the downstream side of the turbine, which acts to augment the flow through the throat of the duct, and therefore increases the total mass flow through the turbine. A second explanation, depicted in figure 1.1 is that the duct acts as an annular wing, producing a lift force acting towards the center of the duct. The lift force has an associated bound circulation, which draws flow towards the duct centerline and hence augments the freestream velocity at the location of the rotor. Regardless of which explanation is used, the overall effect is to increase the power produced for a given rotor diameter. It is sometimes (erroneously) stated that the power augmentation scales with the cube of the increase to the rotor-plane velocity. In reality the augmentation scales with the mass flow increase.

There is no debate as to whether using ducts can improve the power production of turbines of a given rotor diameter in an unbounded flow. This is well established. There are also several other potential benefits of incorporating ducts into the design of tidal turbines. A grate could be included on the duct inlet to prevent large objects/animals from entering the rotor. The duct may attenuate some of the turbulence present in the ambient flow, reducing fatigue loading on the blades. It may also help to better align off-axis flows with the rotor plane, which could eliminate the need for a yawing mechanism in flows that are not perfectly bi-directional. Ducts have been shown to prevent the formation of blade tip vortices [16] which improves performance and could reduce seabed scouring. The real question that will determine whether ducted or non-ducted turbines

become dominant in the context of tidal power generation is which type of turbine can produce the most power, at the lowest cost. Unfortunately, it is very difficult to assess the costs of tidal turbines because there are very few commercial scale devices in existence, and their production costs are proprietary. However there are more physically based metrics for comparing ducted to non-ducted turbines. One is the extraction efficiency, which relates the power production to the total rate of energy dissipated from the tidal flow. Another is the power production per square meter of installed frontal area. These metrics were used as the primary means of evaluating the effectiveness of ducted turbines in this thesis. They are important when considering bounded tidal flows which unlike unbounded atmospheric winds are altered on large scales by any obstructions in the flow, such as energy extracting rotors, ducts and support structures.

1.3 Tidal Flows

Almost all design and analysis methods used for tidal kinetic turbines have been adopted from the wind industry. Bearing this in mind, it is important to understand the differences between tidal flows and wind. The major differences are highlighted in the following points.

1. Energy Density: The density of sea water is approximately $1024\text{kg}/\text{m}^3$, roughly 830 times more dense than air. Peak tidal flows considered viable for power generation are close to $2.5\text{m}/\text{s}$, roughly one-sixth of typical wind velocities in a wind farm. The kinetic energy density of a given flow scales linearly with density and with the square of the velocity. Thus, the energy density of tidal flows is on the order of 20 times that of wind. Thus, a tidal turbine may be approximately one-twentieth the size of an equally rated wind turbine.
2. Reynolds Number: Comparing the density, viscosity and expected length and velocity scales of tidal turbines and wind turbines, it can be found that the expected rotor-diameter-based Reynolds number for tidal turbines is approximately one order of magnitude less than for wind turbines. This is important because airfoil characteristics, particularly near the point of stall, are dependent on Reynolds number. The chord-based Reynolds number will depend primarily on the number of blades and operating tip-speed-ratio chosen for the rotor and should be evaluated for each specific design.
3. Cavitation: Cavitation occurs when the static pressure (p) of the water is reduced to its vapour pressure (p_v). This causes bubbles of vapour to form within the flow. These bubbles can collapse explosively causing severe damage to hydrofoils. When studying cavitation, it is useful to define a cavitation number which compares the required pressure drop for cavitation to the kinetic energy density of the incident flow at the blade ($\frac{1}{2}\rho w^2$).

$$\sigma_c = \frac{p_0 - p_v}{\frac{1}{2}\rho w^2} \quad (1.3.1)$$

This allows for the definition of a cavitation inception envelope, which is characteristic of the airfoil. Batten *et al* [17] followed this approach and showed that for a realistically sized rotor,

even with a small tip immersion of $2m$ cavitation free operation was possible with appropriate selection of airfoil and turbine operation.

4. **Biofouling:** Biofouling is the buildup of marine organisms on the turbines blades, and could increase the drag coefficient significantly. Batten *et al* [17] found that increasing the airfoil drag coefficient by 50% led to significant power reductions at high tip speed ratios. Specialized coatings have been developed (such as [18]) to prevent biofouling, but the impacts of and possible mitigation techniques for biofouling do require further study, and are likely more severe than the fouling seen on wind turbine blades.
5. **Turbulence:** Tidal flows are typically highly turbulent and dynamic. Reliable measurements of turbulence in tidal flows suitable for turbines is quite sparse in literature, however one study [19] showed 10% turbulence intensity, which is the ratio of velocity standard deviation to velocity mean. Gant and Stallard [20] note that turbulent length scales may often be on the same order of turbines themselves. This relatively high turbulence intensity and large length scales may produce large dynamic loading on turbine blades. The accurate representation of turbulence in analysis tools for turbine performance and loading is a field of ongoing research.
6. **Marine Wildlife and Debris:** As opposed to wind turbines, which may be subject to bird strikes, tidal turbine blades may be struck by fish, whales, or partially submerged sea ice and logs. In addition to the potential ecological impact, such events could seriously damage turbines. There is evidence that turbines will rotate slow enough that fish and whales will simply avoid such encounters [9]. There has also been talk of using sonar detection systems to shut-down turbines if large marine animals or other hazards are in close proximity to the turbines [9].
7. **Local Bathymetry:** In general, currents produced by the tides are not fast enough for viable energy extraction and feasible sites for energy extraction exist only where tidal flows are accelerated by local bathymetric features. Examples of where this occurs include: channels between islands or between the mainland and an island; a narrow straight leading to a large basin; estuaries; headlands; peninsulas and complex terrain features that cause a large tidal phase shift in a relatively short distance [5]. Local bathymetric features can also create localized flow accelerations and the shedding of large eddies into the main flow. Such features require regional scale modeling (such as [6, 21, 22]) to capture accurately.
8. **Feedback Effects:** Wind is driven by atmospheric pressure systems with extents on the order of hundreds of kilometers and the impact of wind power extraction, in terms of increased resistance to the flow of air through a region is negligible compared to the driving forces. Tidal flows, on the other hand, are driven by hydrostatic pressure gradients which arise from free-surface height differences, and are limited by inertial and viscous effects. It is possible for tidal turbines to increase the limiting viscous effects to a point that the flow through a given channel is reduced significantly from its natural state (i.e. with no turbines present.) For pilot projects involving a small number of turbines this impact is expected to be negligible, however recent papers [5, 23, 24] have stressed that large scale tidal energy capture will inevitably have a local impact on the velocity, phase and amplitude of tidal flows.

9. Blockage Effects: Tidal flows are bounded by the ocean floor and water surface, and usually by lateral boundaries (channel walls). Placing turbines in such a channel creates wakes of reduced velocity downstream of the turbines, but also regions of increased velocity beside the turbines. Using an analytical model, Vennell [25] showed that turbines occupying a sizable portion of the channel’s cross sectional area, if optimized for such a configuration, can operate much more effectively than isolated turbines without blockage effects. Such performance improvements have also been noted by Garrett and Cummins [26].
10. Free Surface Effects: The presence of turbines may have a local impact on the water height, as demonstrated using a computational fluid dynamics model by Sun *et al* [27]. This free-surface modification can then influence the flow through the turbine, altering its power production. Whelan, *et al* [2] devised an analytical model for such interaction, showing that the inclusion of free surface effects improves turbine performance.

Listing these differences is not intended to imply that wind turbine analysis techniques are not valid in the tidal domain, however it is important to consider that there are fundamental differences between wind and tidal flows, and that care should be taken when applying such models to a new environment.

It would not be possible to study all of the above considerations in any great depth during the course of a two-year program, so this thesis became more focused on specific areas as the work progressed. The areas that received the most attention were blockage effects, free surface effects, and the feedback effects which occur due to the presence of turbines reducing the total flow through the region they occupy. It is in the context of this last consideration that one question regarding the suitability of ducted turbines arose. When ducts are used to enhance turbine power, they also increase the drag force acting on the flow. With enough turbines, this increased drag will eventually have an appreciable effect on the flow, reducing the available resource. Thus, the apparent power increase of ducted turbines in tests where the inflow velocity is held constant likely does not reflect the actual increase when more realistic boundary conditions governing tidal flows are considered.

1.4 Analysis Techniques

At the beginning of this thesis work, a literature review was conducted to determine appropriate methods for analyzing tidal turbines at the device scale. Three categories of methods were considered; blade element momentum (BEM) theory, potential flow methods, and computational fluid dynamics (CFD).

Blade element momentum theory is an analytical/empirical method based on balancing the forces exerted by the turbine blades with the changes to the momentum of the flow. It is by far the least computationally expensive, and gives quite good accuracy for analyzing non-ducted turbines. As such, BEM has enjoyed the widest application to tidal turbines [2, 17, 28–32]. BEM is limited in that it cannot model turbine wakes accurately. In fact the wake is assumed to be cylindrical with a constant tangential velocity. Wake recovery and wake interaction therefore cannot be modeled with BEM. Additionally, at the beginning of this thesis work, there was no suitable BEM method

for analyzing ducted turbines, which involve complex flow phenomena such as flow separation. The development of such a method (which admittedly does rely heavily on empirical coefficients) became one of major accomplishments of the current thesis work.

Potential flow methods stem from inviscid flow theory and make use of singularity elements (vortex sources and momentum sinks/sources) to approximate real-world flows. Potential flow methods have not seen much application to studying tidal turbines, (one example [33] could be found.) This is thought to be due to their increased computational cost compared to BEM, and limited ability to deal with flows with non-thin boundary layers, which precludes their use in separating boundary layers. Flow separation is a vital characteristic which limits the performance of ducted turbines and it is therefore expected that applying potential flow methods to ducted turbines would grossly over-predict the possible power increase. For this reason, potential flow was not considered for this thesis. Nevertheless, potential flow methods could prove to be an extremely useful tool for studying turbine wakes and wake interaction.

Computational fluid dynamics (CFD) simulation has been widely applied to analyzing wind turbines to gain a deeper understanding of flow characteristics that cannot be taken into account by BEM or potential flow methods. At the time of the literature review, only a few studies using CFD for device scale modeling of tidal turbines were found [27, 34, 35], but since then, the application of CFD methods to tidal turbines seems to have become more widespread (a few examples include [16, 36–38]). CFD methods can represent any arbitrary geometry and offer a wide variety of boundary conditions. They solve the Navier-Stokes equations for fluid flow on a discretized domain. The computational mesh must be of sufficient density to resolve the flow accurately, which often results in very computationally expensive simulations. However, this expense may be reduced significantly by employing symmetry boundary conditions, by using simplified representations of turbines [39, 40] and by running simulations at reduced Reynolds numbers [41]. In this thesis work, the turbine rotor was represented in CFD simulations using an actuator disk approach [39], which places momentum source terms in the simulation domain at the location of the rotor. This alleviates the requirement to resolve the blade geometry explicitly, which simplifies the meshing procedure and reduces the number of elements required because the boundary layer on the blades does not need to be resolved. Typically, the forces acting on the blades are determined using a blade element approach using the evolving flowfield and tabulated airfoil coefficients. However in this thesis the inverse method was used, whereby the rotor forces were defined *a priori*, and the required blade geometry was calculated during post processing using blade element considerations. This facilitated a reduction in the number of design variables required for rotor optimization. The wide range of applicability of CFD makes it an ideal tool for analyzing complex flows through and around ducted turbines. However, the time required to run simulations is still considered too long for certain applications such as iterative design optimization and fatigue analysis, for which BEM-based methods remain the most viable option. The work done in this thesis towards establishing the performance of ducted turbines relied heavily on CFD simulations. More detail on the specific techniques employed is provided in chapter 2.

1.5 Key Contributions

The work presented in this thesis contains several key contributions to the fields of tidal turbine design/optimization and tidal power resource assessment.

- The application of actuator disk CFD simulation to determining the performance of a variety of uni-directional ducted turbines, presented at the OCEANS 2010 conference in Seattle [42]
- The determination of empirical model parameters for a 1D duct performance model, presented at the 3rd International Conference on Ocean Energy (2010) in Bilbao, Spain [43], and later published in the IMechE. Journal of Power and Energy [44]
- Merging the duct model (above) with blade element momentum theory to provide a medium fidelity but very fast semi-empirical model for ducted turbine performance analysis and blade design, submitted for publication in the IMechE. Journal of Power and Energy [45]
- Developing a novel blade optimization tool for ducted and non-ducted turbines in unbounded and constrained flows which is based on actuator disk CFD simulation, presented at the 2011 ISOPE conference in Maui, Hawaii [46]
- Developing an actuator disk CFD methodology for simulating free surface effects due to tidal turbines
- Developing a new analytical treatment for free surface effects
- Demonstrating that tidal turbines designed to take advantage of channel blockage effects can produce significantly more power per square meter of installed frontal area than those designed for unbounded flows (A reasonable estimate is a threefold improvement with turbines occupying 50% of the channel cross sectional area in a single ‘fence’)
- Demonstrating that using ducts to increase the power production of tidal turbines is less effective than increasing the rotor diameter to the same size of the duct exit
- Demonstrating that for a given level of useful power production, non-ducted turbines dissipate less total energy from the tidal flow, thus producing a lesser change in tidal amplitude and basin flushing

1.6 Research Questions, Scope and Key Assumptions

This research began with a single question. ‘Is there a real technical advantage to using ducts to increase the power generation of tidal turbines?’. To be able to address this question it was necessary to determine how to compare ducted to non-ducted concepts. Thus, meaningful metrics for comparison had to be decided upon. It also became apparent that for a fair comparison it was necessary to define optimal (or at least nearly so) designs for both ducted and non-ducted turbines. Note that a distinction is made between *ideal* and *optimal* turbine rotors. *Ideal* refers to an abstract concept of a rotor which operates perfectly, with no blade drag and no losses. On the other hand,

optimal rotors are achievable in the real world and operate within the physical constraints of real losses due primarily to drag. During the course of the work, many new questions arose. A summary of the major research questions is provided below:

1. Is there a real technical advantage to using ducts to increase the power generation of tidal turbines?
2. What are some valid metrics for comparing the performance of ducted and non-ducted turbines?
3. How can ducted and non-ducted turbines be optimized?
4. Since the boundary conditions on tide-driven flows are different than atmospheric flows (i.e. wind), are there major differences in how energy can be extracted and do these factors interact differently with ducted concepts than non-ducted concepts?
5. What is the best strategy to maximize power production of turbines, while minimizing the cost and environmental impact?

During the research, it was found that the first four research questions were inherently linked, and could not be fully addressed as individual problems. As mentioned above, a fair comparison of ducted and non-ducted turbines involves defining *optimal* turbines for both concepts. Additionally, the optimal design of an individual turbine depends on the environment in which it operates. Due to this, much of this thesis work involved developing rotor optimization methods for ducted turbines in bounded flows. Of course, the last question is of much larger scope than can be answered in a single study, however it was worth asking to provide a greater context to the research conducted, even if an answer seemed out of reach.

To answer these research questions fully, one would have to address all aspects of turbine design including hydro-dynamics, structural, manufacturability, maintainability and cost. This would have to be done in the context of real-world tidal flows, which may be highly turbulent and vary significantly from location to location. Each of these aspects is a field of research in its own right, and it would not have been possible to consider them all. Thus the scope of this thesis was limited by the following:

- Only hydro-dynamic considerations were made for turbine optimization and for defining metrics for comparing ducted to non-ducted concepts
- Tidal flows were assumed to be quasi-steady and vary in time according to a single sinusoidal signal.
- CFD simulations always sought a steady state solution
- Turbine rotors were represented by an actuator disk in CFD simulations
- Only axial flow turbines were considered

Year/Month	Milestone
2009 Oct	Literature review of analysis methods for wind/tidal turbine fluid dynamics. Choice: BEM & CFD
Nov	Preliminary work on BEM implementation using fixed point iteration
2010 Jan	Development of meshing strategy for CFD sims
Mar	CFD methodology for axial flow and axial forcing finalized
Apr	CFD grid convergence study and comparison to previous simulations
May	Initial study of turbine extraction efficiency
Jun	Literature review of analytical models for ducted turbine performance. Choice: Lawns model
Jun	Initial CFD study of effects of geometry on inlet efficiency, diffuser efficiency and base pressure coefficient
Jul	CFD methodology expanded to include wake swirl and tangential forcing
Aug	Development of CFD model for blockage effects and free surface deformation
Oct	Final CFD study of effects of geometry on inlet efficiency, diffuser efficiency and base pressure coefficient
Nov	Development of geometry-based empirical duct performance model by curve fitting CFD results
2011 Mar	Development of CFD-based blade optimization tool using Matlab&CFX
May	BEM implementation using fmincon (gradient based optimization)
Jun	Development of DuctBEM analysis and blade optimization tool
Jun	Comparison of DuctBEM to CFD simulations
Jul	Decision to compare turbines based on constant frontal area instead of constant rotor diameter
Jul	Extended CFD-based blade optimization tool to account for blockage effects and realistic tidal forcing
Aug	Case study of Minas Passage tidal turbine fence

Table 1.1: Timeline of milestones accomplished during this thesis work

- For the purpose of evaluating the effect of turbines on the flow, the case of a channel connecting a basin to the ocean was considered.
- The performance of the tested ducts was assumed to be independent of Reynolds number

1.7 Contextual Background

The organization of this thesis was challenging due to the wide variety of methods used and their application in various combinations to complete the various studies conducted. The thesis is organized such that all of the analysis methods are explained in chapter 2 and their application to a number of studies is described in chapter 3. Such an organization was chosen to provide readers with a complete, uninterrupted methodology section, but sacrifices some continuity in the presentation of the research in a chronological sense. This section provides some contextual background into the chronology of the work presented, and how the various pieces of this thesis fit together. A brief chronology is provided in table 1.1 to put the various models developed and results obtained into context.

The first phase of the work was to develop a CFD simulation strategy to model the performance of *ideal* rotors with and without ducts. This idealized treatment imposed a thrust force on the flow to model the influence of the rotor. The power was calculated as the product of the thrust force and the local velocity at the rotor plane. As the thrust force increases, the local velocity decreases. Thus, for a specific duct, there is some optimal level of thrust where the power is maximized.

This simplified ‘axial-only’ model was used in two initial studies, both of which assumed the turbines were operating in an unbounded domain (i.e. blockage and feedback effects were neglected). The first study (section 3.1) determined the *ideal* performance of turbines using a variety of ducts operating in an unbounded domain (i.e. neglecting blockage and feedback effects). The second study (section 3.2) determined the influence of changing the duct geometry on the rotor performance. These initial studies provided insight into the fundamental limits to ducted (and non-ducted) turbine performance. However a more detailed strategy was required to determine the *optimal* performance that could be achieved by real rotor designs.

The next phase of the work extended the simplified CFD method described in the previous paragraph to include the torque of the rotor which creates swirling flow in the wake. This was achieved by considering relationships between the lift and drag forces acting on the turbine blades, and the flow direction at the rotor plane. Now the power had to be calculated as the product of the torque and the rotor angular velocity, in order to compute the mechanical output power. Simply calculating output power as the product of local velocity and thrust would have yielded an ideal shaft power, which would have neglected the additional losses due to wake swirl and blade drag. Now there were essentially two inputs to the simulation, one was the thrust (which could now vary linearly with radius with a defined slope) and the other was the rotor speed. The torque depended on the local flow at the rotor plane, and the distribution of thrust force. To find the maximum power output, it was necessary to find the optimal combination of thrust loading and rotor speed. A search algorithm was defined to automate this process. Because the loading condition was now linked to the forces acting on the blades, it was now possible to determine the blade geometry which would produce the specified forces. This was a novel inverse method of blade optimization, as traditional approaches use chord and twist at a discrete number of points along the blade as design variables to specify loading indirectly. The novel approach reduced the number of design variables significantly, thereby allowing for faster optimization. The capability of this extended CFD method is demonstrated in section 3.3, which studied the impact of using non-uniform thrust loadings on ducted turbine performance.

In parallel with the development of the extended CFD model described in the previous paragraphs, an advanced BEM method (referred to as Duct BEM and defined in section 2.3) was pursued with the goal of producing an analytical/empirical method of accounting-for the influence of the duct on the flow and rotor performance. The motivation for this model was to develop a faster analysis method suitable for future design work, by avoiding the computational expensive of CFD simulations. Future work could also apply the method to studying dynamic loading due to inflow turbulence and non-uniform inflow. The Duct BEM model development followed a similar progression to the CFD based models described above. First an idealized model (section 2.3.2) was developed that only considered the thrust force of the turbine rotor. This idealized model depended on parameters

which were determined using CFD simulations as described in section 3.2. The Duct BEM model was later extended to consider the torque of the rotor (section 2.3.3), and the results of this model are compared to its analogous CFD model in section 3.4, which shows a good general agreement.

The next phase of the work involved incorporating methods to account for channel blockage, and free surface deformation on the performance of turbines. A new type of CFD simulation was implemented to determine the free-surface deformation associated with power extraction by turbines, and the impact of this deformation on the turbine performance. Additionally, an analytical model was developed for the same scenario. These models are defined in section 2.5, and were employed to determine whether it was necessary to include free surface deformation in calculating the power output of tidal turbines. It was found that free surface deformation had a minor impact on turbine performance compared to the impact of blockage effects. Thus, it was decided that further work would focus on incorporating blockage effects into the turbine design methods, but more detailed study of free surface deformation would be saved for future studies. Blockage effects were included in the CFD rotor design method by altering boundary conditions to restrict the flow domain to have a finite cross-sectional area. A treatment for blockage effects was not developed for the Duct BEM model because of time constraints and because the applicability of the performance parameters to blocked flows was uncertain.

The final stage of the work was to incorporate feedback effects into the CFD rotor design methodology. The goal of this was to provide a method for designing turbines to operate in a ‘tidal fence’ configuration (a line of turbines spanning a portion of a tidal channel cross section) using a known tidal forcing as a realistic boundary condition. This method is described in section 2.6, and was accomplished using a published analytical model for basin-channel dynamics. The resulting CFD-based rotor design methodology allowed the optimization of the turbine thrust loading and rotor speed, while considering blockage and feedback effects, in the context of a real world tidal channel. Once the performance of the tidal fence was optimized, the required blade geometry was calculated during post processing. This model was used to conduct a case study of the power extraction potential of Minas Passage in the Bay of Fundy as described in section 3.6.

1.8 Thesis Organization

This thesis is organized into four chapters. The remaining chapters are organized as follows:

Chapter 2 provides details of the methods used for analyzing tidal turbines and tidal flows. This includes descriptions of: the standard blade element momentum BEM formulation, and its adaptation for ducted turbines; the actuator disk CFD simulation method; the treatment of blocked flows and free surface effects using analytical and CFD-based methods; and the inclusion of realistic tidal forcing in determining the power production of turbines in a real channel.

Chapter 3 discusses a series of studies which were conducted using the methods described in chapter 2. These studies included: an assessment of ideal turbine performance and extraction efficiency in unbounded flows; the determination of model parameters for a semi-empirical extension of BEM for ducted turbines (DuctBEM); a demonstration of the CFD-based blade optimization tool; comparing the results of DuctBEM to the actuator disk CFD method; an evaluation of free

surface effects for tidal power generation; and a case study of tidal turbines in Minas Passage, Bay of Fundy.

Chapter 4 contains a summary of the work done, answers to the research questions and recommendations for future work.

Chapter 2

Model Development

This chapter describes the methods and models used for conducting the research studies presented in this thesis. Section 2.1 defines the method used to define the considered duct geometries, and shows all of the ducts used throughout this thesis. Section 2.2 describes the standard blade element momentum (BEM) theory for calculating the performance of non-ducted turbines in unbounded flows. Section 2.3 describes the adaptation of BEM for ducted turbines in an unbounded domain, which relies on empirically determined model coefficients which characterize the influence of the duct on the axial flow through the rotor. Section 2.4 describes the actuator disk CFD method used in this thesis including a grid independence study, initial validation and a rotor optimization technique which makes use of the CFD simulations. Section 2.5 describes methods used for analyzing the effects of channel blockage and free surface effects including analytical treatments and an actuator disk CFD model which uses a volume of fluid approach to represent the free surface. Finally, Section 2.6 describes a method to incorporate channel blockage effects and a realistic tidal forcing for a particular real-world channel into the actuator disk CFD simulations. This allows optimizing turbines for a variety of channel blockage ratios in a real-world application.

2.1 Duct Geometries

Several different duct geometries were analyzed during the course of this thesis to study how the duct shape affects the performance in terms of the increased power, diffuser efficiency and flow separation behavior. The ducts were created by modifying a NACA0015 airfoil using a series of transformations. This method was adapted from [1], and initially was used to allow a comparison to their original simulations. The method continued to be used because it allowed defining a wide range of duct geometries with modifying only a few key parameters. The geometric features expected to impact the duct performance were the diffuser expansion ratio A_4/A_3 ; the inlet contraction ratio A_1/A_3 ; the duct airfoil thickness ratio; and the inner and outer diffuser surface angles $\theta_{4,in}$, $\theta_{4,out}$ as depicted in figure 2.1.

A baseline geometry (D2) was designed to replicate the duct used in [1] for model comparison. The ducts were based on a NACA 0015 airfoil which was first scaled in thickness by a factor k_t . A

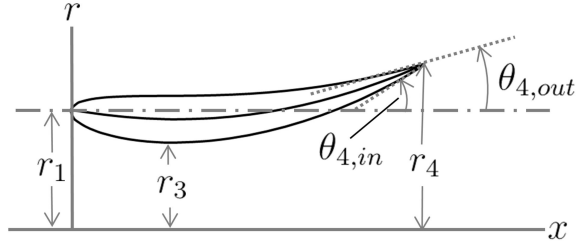


Figure 2.1: Duct geometric attributes used by the regression based model

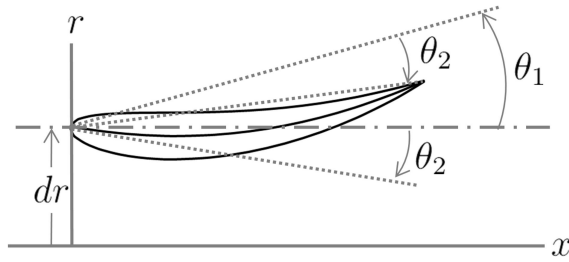


Figure 2.2: Control parameters used to define the duct geometry

camber was then applied by rotating the geometry about the leading edge through a linearly varying angle (0° at the leading edge to θ_1 at the trailing edge). A full body rotation through θ_2 was then applied to the entire cross section. Finally the airfoil was translated by dr to control the throat area A_3 . The set of control parameters $(k_t, \theta_1, \theta_2, dr)$ used to define the duct shape are depicted in figure 2.2. This methodology allowed full control over a wide variety of duct area ratios and angles.

The above control parameters and resulting duct area ratios and outlet angles are summarized in table 2.1 for all of the ducts used in this study. Figure 2.3 gives a graphical representation of the resulting geometric features. The ducts were classified into two subsets during the development of the empirical duct model described in section 3.2. One set was used for developing the empirical duct model using curve-fitting (identified by the letter D) and the other for validating the model once its definition was complete (identified by the letter V). The resulting 2D duct profiles are shown in figure 2.4 where the duct length L is held constant. Three-dimensional renderings of the ducts are provided in figure 2.5, where the ducts have been scaled to have a constant rotor diameter.

There are several ways to scale the resulting geometries which provide different perspectives when comparing different duct geometries. In most studies of ducted turbines [12, 13, 15, 47–51] the rotor diameter has been held constant, and increasing the duct expansion ratio (A_4/A_3) generally leads to increased power. It is also possible to hold the duct length constant, however this scaling makes it difficult to compare various designs. The third option, which is starting to appear in the literature [16, 49] is to hold the total projected frontal area of the device constant. This option is thought to give a more reasonable comparison between various ducted concepts, and in comparing to non-ducted designs for two reasons. The first is that the turbine’s total frontal area is what limits the number of devices which will physically fit within a transect of a given channel. The second is that the cost

Duct	Control Parameters				Duct Attributes			
	k_t	θ_1 [deg]	θ_2 [deg]	d_r [m]	A_4/A_3	A_1/A_3	$\theta_{4,in}$ [deg]	$\theta_{4,out}$ [deg]
D1	0.45	8.08	0.00	0.83	1.47	1.07	19.95	11.37
D2	0.45	8.08	0.00	0.50	1.84	1.12	19.95	11.37
D3	0.45	8.08	0.00	0.35	2.36	1.18	19.95	11.37
D4	0.45	8.08	0.00	0.28	2.87	1.24	19.95	11.37
D5	1.00	8.08	-18.92	0.62	1.84	1.73	27.57	10.27
D6	1.00	8.08	-11.65	0.58	2.36	1.50	34.84	17.54
D7	1.00	8.08	-5.00	0.56	2.87	1.34	41.49	24.19
D8	0.40	15.0	-3.00	1.09	1.50	1.05	29.53	22.24
D9	0.40	15.0	-3.00	0.60	2.00	1.10	29.53	22.24
D10	0.40	15.0	-3.00	0.43	2.56	1.15	29.53	22.24
V1	0.54	10.35	0.00	0.55	2.00	1.13	25.04	14.96
V2	0.28	14.25	0.00	0.44	2.62	1.07	30.06	24.93
V3	0.28	6.86	0.00	0.25	2.61	1.15	16.02	10.64

Table 2.1: Summary of duct control parameters and resulting attributes

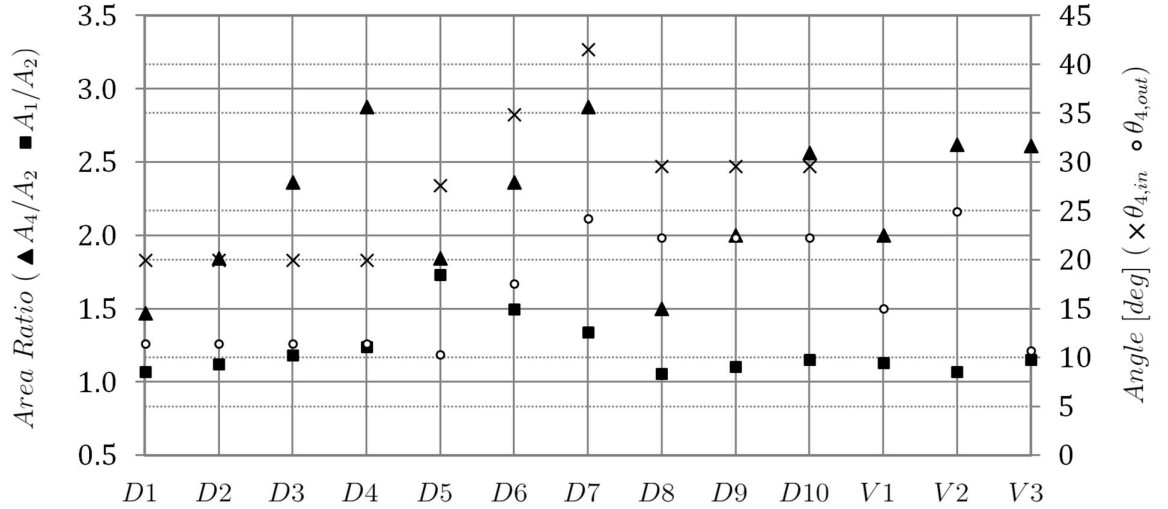


Figure 2.3: Duct area ratios and outlet angles.

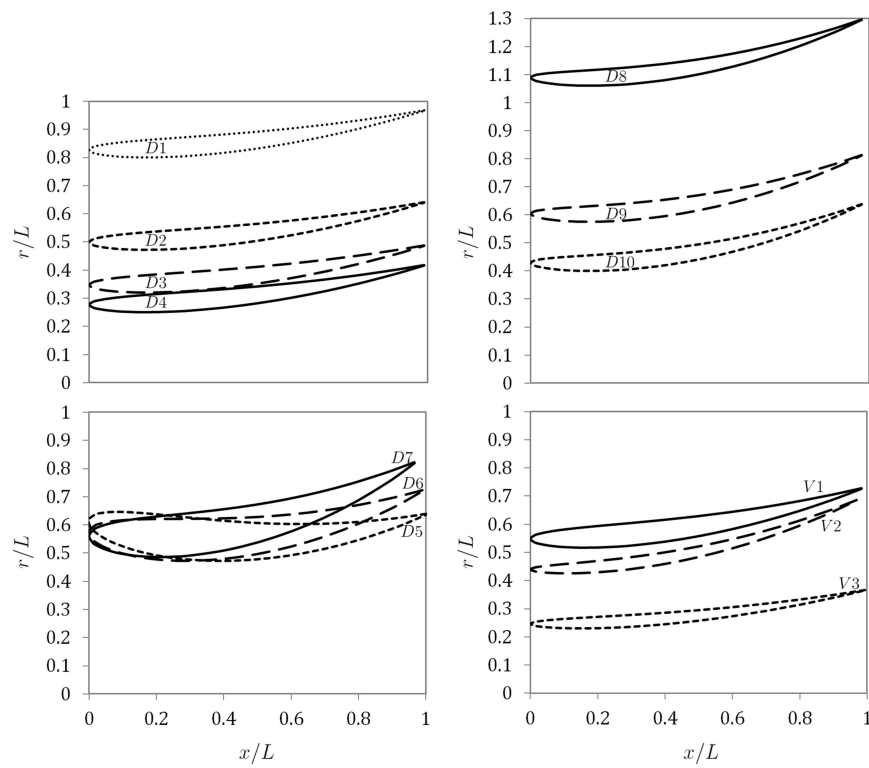


Figure 2.4: Profiles of the duct geometries used in this thesis, scaled with constant duct length

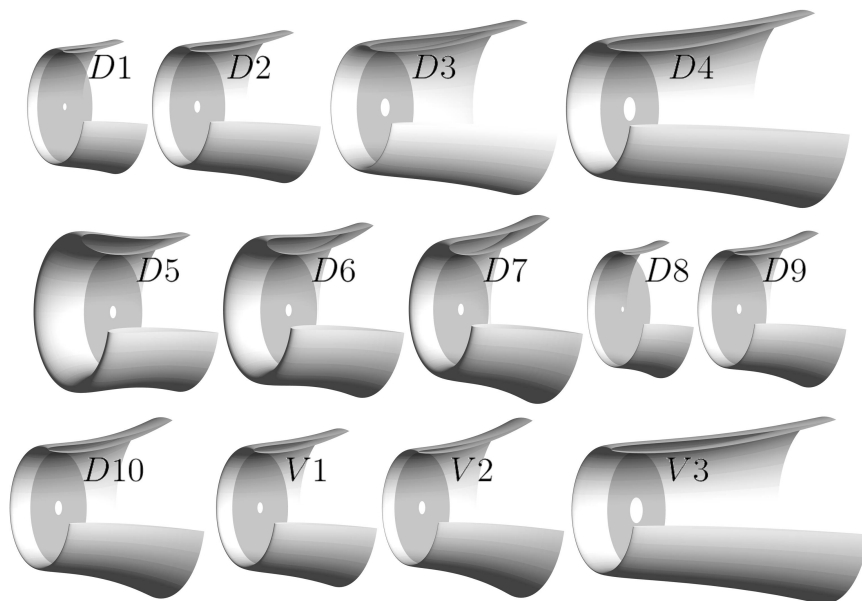


Figure 2.5: Three-dimensional renderings of the ducts used in this thesis, scaled to have a constant rotor diameter

of a ducted turbine is more likely to be similar to a non-ducted turbine of equal total frontal area, rather than one of equal rotor diameter. In this thesis, the turbine performance is presented using non-dimensionalized parameters (for example the power coefficient C_P) so the physical dimensions of the tested ducts becomes irrelevant (provided Reynolds number independence is assumed). The perspective taken (i.e. whether the rotor diameter, or total frontal area is held constant) comes into the equations via the choice of which area is used in normalizing the thrust, power and all other performance parameters, as shown below, in which A_r is the rotor area, and A_f is the device frontal area.

constant rotor diameter	constant frontal area
$C_P = \frac{\text{Power}}{\frac{1}{2}\rho u_0^3 A_r}$	$C_P = \frac{\text{Power}}{\frac{1}{2}\rho u_0^3 A_f}$

Initial studies in this thesis work chose to use a constant the rotor area, however through the course of the work it was decided that using a constant frontal area gave a more fair comparison as discussed above. Both perspectives are presented in various sections of this thesis.

To represent more realistic turbine geometries, a crude hub was also included in some duct designs selected for blade design optimization using the DuctBEM and CFD-based optimization tools. Similar to the ducts, the hub geometry was created by modifying the NACA 0015 airfoil. The thickness was altered such that the maximum cross sectional area of the hub was 2% of the duct throat area. The hub length was set to 40% of the duct length, and the hub was translated axially such that its maximum radius occurred at the duct throat location. This is not likely the optimal hub geometry, and could certainly be improved upon in future work. The ducts were designed to cover a reasonable range of feasible geometries. It is realized that the geometries do not cover a full search space for all duct parameters, however time constraints dictated using a small subset of all possible designs. In fact most duct designs for tidal power application are bi-directional, whereas the ones studied in this thesis are uni-directional, which would require a yawing mechanism to be able operate in both the ebb and flood tides. It is expected that bi-directional ducts will have significantly reduced performance compared to uni-directional ones due to flow recirculation inside an inlet which is much larger than the required capture area, and separation of the exterior flow off a relatively sharp leading edge. Thus, the performance of the ducts studied in this thesis here are likely somewhat optimistic compared to real-world turbines for tidal power applications.

2.2 Blade Element Momentum Theory For Non-Ducted Turbines

A summary of the blade element momentum (BEM) theory is given in this section. BEM has been used extensively in the design and analysis of wind turbines for decades [52, 53] and is often used for modeling and designing kinetic marine turbines [2, 17, 28–32]. This widespread application is primarily due to its surprisingly high accuracy, and minimal computational expense. In this thesis BEM was used to define the ideal performance of non-ducted turbines operating in an unbounded domain. It was expanded-upon to define the DuctBEM model in section ??, and provided much of the theory used in defining the actuator disk CFD simulation methodology described in section 2.4.

BEM is an analytical/empirical method based on balancing the forces exerted by the turbine blades with the changes in the momentum of the flow. The simplest formulation (known as uniform axial actuator disc theory) consists of a balance between the turbine’s axial force and the change in axial momentum of the flow. This can be used to determine the ideal turbine performance, but neglects losses due to blade drag and kinetic energy transfer to the swirling wake. The basic BEM equations also include an equation balancing the torque applied to the flow by the turbine to the change in the angular momentum of the flow. Traditionally in BEM formulations, several semi-empirical corrections are appended to the basic set of equations to improve agreement with experimental data. These corrections attempt to account for: 1) the breakdown of momentum theory at high rotor loading, 2) discrete blade effects (tip loss) and 3) 3D flow effects on a rotating blade.

2.2.1 Derivation

The full derivation of BEM theory is presented in numerous texts on wind turbines such as [54]. A brief derivation is provided here; for more detail please refer to an appropriate text. Figure 2.6 shows the axial locations used throughout this thesis which are denoted in the equations using subscripts, and do deviate somewhat from standard texts owing to the inclusion of the duct treatment.

The turbine is represented as an infinitesimally thin disk occupying the swept area of the turbine, located between stations 2 and 3 in figure 2.6. As the flow approaches the disk it decelerates and the enclosing streamtube expands. Across the disk there is a finite pressure drop ($p_2 - p_3$), but the velocity is unchanged. The turbine’s axial force, commonly called thrust T , is equal to the product of this pressure drop and the disk area A_2 . Using steady flow 1D momentum theory on the bounding streamtube between stations 0 and 5,¹ a relationship between the change in axial momentum and the axial force (T) applied to the flow by the turbine can be defined as follows:

$$\begin{aligned} \sum F_x &= \sum (\dot{m}_i u_i)_{out} - \sum (\dot{m}_i u_i)_{in} \\ -T &= \dot{m} (u_5 - u_0) \\ (p_2 - p_3)A_2 &= \rho A_2 u_0 (1 - a)(u_0 - u_5) \end{aligned} \tag{2.2.1}$$

¹This approach inherently neglects all viscous and pressure forces acting on the boundary of the streamtube. Mikkelsen [39] showed that the pressure forces are negligible.

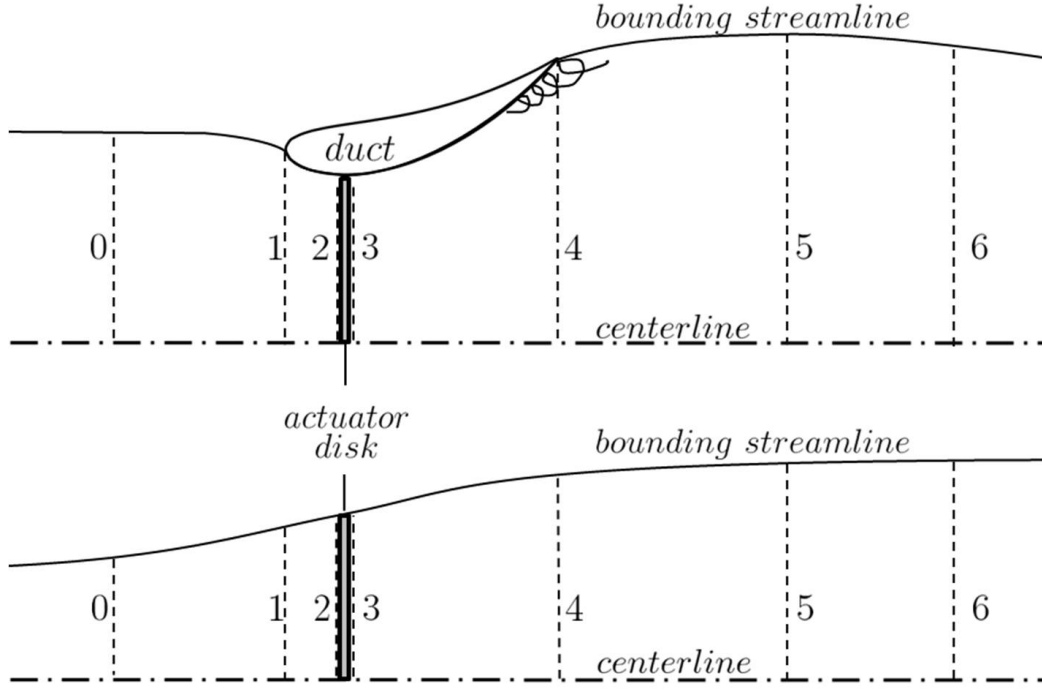


Figure 2.6: Diagram of relevant axial stations for ducted (top) and conventional (bottom) turbines ; 0) undisturbed freestream, 1) duct entry plane, 2) just upstream of the rotor, 3) just downstream of the rotor, 4) duct exit plane, 5) far wake and 6) very far wake.

Note that the actuator disk is assumed to be infinitely thin such that $u_2 = u_3$. Also, an axial induction factor a is defined such that $u_2 = u_0(1 - a)$. The far wake (station 5) is defined as the location where the pressure in the wake has recovered to ambient, i.e. $p_5 = p_0$. With this in mind, using Bernoulli's equation downstream from 0 to 2 and then upstream from 5 to 3 yields the following:

$$\begin{aligned}
 p_0 + \frac{1}{2}\rho u_0^2 &= p_2 + \frac{1}{2}\rho u_2^2 \\
 p_0 + \frac{1}{2}\rho u_5^2 &= p_3 + \frac{1}{2}\rho u_2^2 \\
 \therefore \frac{1}{2}\rho (u_0^2 - u_5^2) &= p_2 - p_3
 \end{aligned} \tag{2.2.2}$$

Substituting for $p_2 - p_3$ in equation 2.2.1 then yields:

$$\begin{aligned}
 \frac{1}{2}\rho (u_0^2 - u_5^2) A_2 &= \rho A_2 u_0(1 - a)(u_0 - u_5) \\
 (u_0 - u_5)(u_0 + u_5) &= 2u_0(1 - a)(u_0 - u_5) \\
 u_5 &= u_0(1 - 2a)
 \end{aligned} \tag{2.2.3}$$

Note that this derivation implies a shear layer along the bounding streamline depicted in figure 2.6, but neglects the resulting viscous forces in the axial momentum equation.

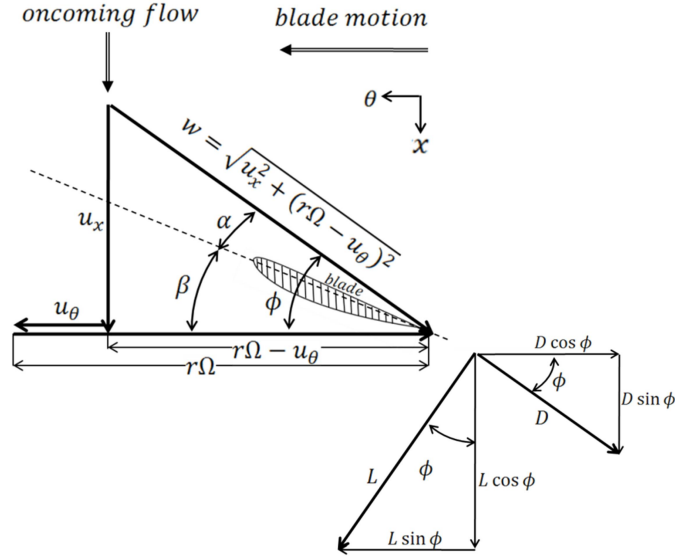


Figure 2.7: Diagram of the relative velocity at a turbine blade section.

In addition to the balance of axial force and axial momentum, it is necessary to account for the balance of rotor torque and angular momentum. For this purpose, and to account for radial variation of the axial force, it is useful to divide the disk into infinitesimal annular disks of radius r , thickness dr and area $2\pi r dr$. Note that the derivation of equations 2.2.1, 2.2.2 and 2.2.3 also holds for such an annulus. Combining equations 2.2.1 and 2.2.2 and defining the local thrust on a single annulus as f_x gives a new expression for the balance of axial force and momentum for each annulus:

$$f_x = \rho 2\pi r dr u_0^2 2a(1-a) \quad (2.2.4)$$

A tangential induction factor a' is defined such that the tangential velocity at the rotor plane is $u_\theta = r\Omega a'$, (where Ω is the rotor angular speed and r is the radial position) and just downstream of this location the tangential velocity is $u_{\theta,3} = r\Omega 2a'$. The rate of change in angular momentum of the fluid passing through an annulus is equal to the product of the local tangential force f_θ and radius r .

$$\begin{aligned} f_\theta r &= \dot{m} \Delta u_\theta r \\ f_\theta r &= \rho 2\pi r dr u_0 (1-a) 2\Omega a' r^2 \end{aligned} \quad (2.2.5)$$

The local axial and tangential forces acting on the flow in each annulus (f_x, f_θ) can be related to the blade lift and drag forces, which are determined using tabulated lift and drag coefficients (c_l, c_d). The flow velocity relative to the blade has various components as illustrated in figure 2.7. The angle between the relative velocity w and the rotor plane is the inflow angle ϕ . This angle also relates the blade lift and drag to f_x and f_θ . For an infinitesimal section (of constant radius) of a set of B turbine blades of chord length c centered at r with length dr , the axial and tangential forces are defined by:

$$f_x = \frac{1}{2} \rho w^2 B c c_x dr \quad (2.2.6)$$

$$f_\theta = \frac{1}{2} \rho w^2 B c c_\theta dr \quad (2.2.7)$$

where:

$$c_x = c_i \cos \phi + c_d \sin \phi \quad (2.2.8)$$

$$c_\theta = c_i \sin \phi - c_d \cos \phi \quad (2.2.9)$$

With the blade forces defined, and defining the local blade solidity $\sigma = \frac{Bc}{2\pi r}$, it is possible to express the *axial* momentum/force balance by combining equations 2.2.4 and 2.2.6:

$$\begin{aligned} \rho 2\pi r dr u_0^2 2a(1-a) &= \frac{1}{2} \rho w^2 B c c_x dr \\ \frac{a}{1-a} &= \frac{w^2}{4u_0^2(1-a)^2} \frac{Bc}{2\pi r} c_x \\ \frac{a}{1-a} &= \frac{\sigma c_x}{4 \sin^2 \phi} \end{aligned} \quad (2.2.10)$$

For the above, note that $\sin \phi = \frac{u_0(1-a)}{w}$. Defining the normalized radius $\mu = r/R$ where R is the turbine tip radius, and the tip speed ratio $\lambda = \frac{R\Omega}{u_0}$ the *angular* force/momentum balance is written by combining equations 2.2.5 and 2.2.7:

$$\begin{aligned} \rho 2\pi r dr u_0(1-a) 2\Omega a' r^2 &= \frac{1}{2} \rho w^2 B c c_\theta r dr \\ \frac{a'}{1+a'} &= \frac{w^2 c_\theta}{4u_0^2(1-a)\lambda\mu(1+a')} \frac{Bc}{2\pi r} \\ \frac{a'}{1+a'} &= \frac{\sigma c_\theta}{4 \sin \phi \cos \phi} \end{aligned} \quad (2.2.11)$$

For the above, $\cos \phi = \frac{\lambda\mu u_0(1+a')}{w}$. Equations 2.2.10 and 2.2.11 represent a system of non-linear equations that are most often solved independently for each annulus using fixed point iteration. Note that in this thesis work, a non-linear sequential quadratic programming optimization algorithm called *fmincon* available in Matlab was used instead of the typical fixed point iteration, as discussed in section 2.2.5.

2.2.2 Including Wake Swirl

Some authors such as Burton *et al.* [54] note that the swirling wake downstream of the rotor produces a reduction in pressure that should be accounted for in the axial force/momentum balance equation. This is achieved by equating the pressure drop due to swirl to the change in dynamic head in the azimuthal direction. This gives the effective axial pressure force on an annulus due to swirl as:

$$f_{x,sw} = \frac{1}{2} \rho (2a'\Omega r)^2 2\pi r dr \quad (2.2.12)$$

To derive the impact of this term on the system of equations to be solved, it is beneficial to first re-write the *angular* momentum/torque balance as:

$$\begin{aligned} 2\pi r u_0 (1-a) 2\Omega a' r &= \frac{1}{2} w^2 B c c_\theta \\ \frac{a' \lambda \mu}{1-a} &= \frac{w^2}{4u_0^2 (1-a)^2} \frac{Bc}{2\pi r} c_\theta \\ \frac{a' \lambda \mu}{1-a} &= \frac{\sigma c_\theta}{4 \sin^2 \phi} \end{aligned} \quad (2.2.13)$$

Noting that the pressure reduction due to wake swirl acts in a direction opposite to the turbine axial force, it is included in the *axial* force/momentum relationship:

$$2\pi r u_0^2 2a(1-a)r = \frac{1}{2} w^2 B c c_x - \frac{1}{2} (2a'\Omega r)^2 2\pi r$$

Manipulating this gives;

$$\frac{a}{1-a} = \frac{w^2}{4u_0^2 (1-a)^2} \frac{Bc}{2\pi r} c_x - \left(\frac{a' \lambda \mu}{(1-a)} \right)^2$$

Noting that equation 2.2.13 defines an expression for the the rightmost term above and substituting yields (with some further simplification) a new form of the axial momentum governing equation:

$$\frac{a}{1-a} = \frac{\sigma}{4 \sin^2 \phi} \left[c_x - \frac{\sigma c_\theta^2}{4 \sin^2 \phi} \right] \quad (2.2.14)$$

When accounting for wake swirl in the axial momentum balance, equations 2.2.11 and 2.2.14 are solved simultaneously, again typically using fixed point iteration independently for each annulus, but using *fmincon* in this thesis.

2.2.3 Thrust and Power

When the solution has converged, the rotor performance can be determined by calculating the thrust and power coefficients (C_T, C_P), defined as:

$$C_T = \frac{\text{Thrust}}{\frac{1}{2} \rho u_0^2 A_r} \quad (2.2.15)$$

$$C_P = \frac{\text{Power}}{\frac{1}{2} \rho u_0^3 A_r} \quad (2.2.16)$$

where A_r is the rotor swept area. To find these quantities, it is useful to first define local thrust and power coefficients (c_T, c_P). The local thrust coefficient is found by normalizing the total axial force acting on a single annulus (equation 2.2.6) by the freestream dynamic pressure and the annular area $2\pi r dr$:

$$\begin{aligned} c_T &= \frac{\frac{1}{2} \rho w^2 B c c_x dr}{\frac{1}{2} \rho u_0^2 2\pi r dr} \\ &= \sigma c_x \left(\frac{w}{u_0} \right)^2 \end{aligned} \quad (2.2.17)$$

The local power produced by a single annulus is the product of the torque $f_{\theta}r$ and rotor angular speed Ω . This is normalized by the upstream kinetic power density $\frac{1}{2}\rho u_0^3$ and annular area $2\pi r$.

$$\begin{aligned} c_P &= \frac{\frac{1}{2} \rho w^2 B c c_{\theta} r \Omega dr}{\frac{1}{2} \rho u_0^3 2\pi r dr} \\ &= \sigma c_{\theta} \lambda \mu \left(\frac{w}{u_0} \right)^2 \end{aligned} \quad (2.2.18)$$

If the balance between the rotor torque and the flow's angular momentum, and the impact of wake swirl on the axial momentum/force balance are not considered (i.e. axial actuator disk theory), then the local thrust coefficient may be found by considering the change in axial momentum of the flow, given in equation 2.2.4 . This results in:

$$\begin{aligned} c_{Tideal} &= \frac{\rho 2\pi r dr u_o^2 2a(1-a)}{\frac{1}{2} \rho u_0^2 2\pi r dr} \\ &= 4a(1-a) \end{aligned} \quad (2.2.19)$$

In this axial only treatment, the local power is determined by the product of the total axial force acting on an annulus and the local axial velocity at that annulus. This gives the ideal local power coefficient as:

$$\begin{aligned} c_{Pideal} &= \frac{\frac{1}{2} \rho w^2 B c c_x u_0 (1-a) dr}{\frac{1}{2} \rho u_0^3 2\pi r dr} \\ &= \sigma c_x (1-a) \left(\frac{w}{u_0} \right)^2 \end{aligned} \quad (2.2.20)$$

$$= c_T (1-a) \quad (2.2.21)$$

$$= 4a(1-a)^2 \quad (2.2.22)$$

The total thrust and power coefficients (C_T, C_P) are found by integrating the product of the local thrust/power coefficients and the local annular area divided by the total disk area:

$$(C_T, C_P) = \int_0^R (c_T, c_P) \frac{2\pi r}{A_r} = \int_0^1 (c_T, c_P) 2\mu d\mu \quad (2.2.23)$$

The blade element momentum equations are most often applied to a discretized domain of N concentric radial annuli. Thus the above integral is evaluated numerically as a weighted sum;

$$(C_T, C_P) \approx \frac{\sum_{i=1}^N (c_{T_i}, c_{P_i}) A_i}{\sum_{i=1}^N A_i} \quad (2.2.24)$$

where A_i is the area of the i^{th} annulus.

2.2.4 Discrete Blade Effects

Generally, there is azimuthal variation in the axial induction at the rotor plane. This results in a discrepancy between the induction used to account for the change in the fluid momentum as it passes through the rotor, and the induction used to calculate the blade forces. This azimuthal variation is typically accounted for using a so-called tip loss model, the most common being the Prandtl tip loss model [54]. Note that this model is formulated to relate the average induction in the far wake (at station 5) to the local induction at the blade. Thus it is an empirical factor that attempts to account for a range of phenomena including finite-length blade effects with discrete numbers of blades.

The Prandtl tip loss model was used for non-ducted turbine modeling to assess the impact of tip loss on the optimal power production of a reasonable tidal turbine. The model defines a tip loss factor f_p which is a ratio of the induced axial velocity on a wake sheet trailed from the blade to the azimuthally averaged velocity. This ratio is defined at the far wake location (5), but the model assumes that the same ratio applies at the rotor plane. The azimuthally averaged velocities are used to define the mass flow through the rotor, and the change in axial and tangential velocities. Also the pressure change in the wake due to swirl is found based on the azimuthally averaged tangential velocity. The angle of attack used to find the blade forces is calculated using the blade local velocity. By defining the axial induction at the blade a , the azimuthally averaged induction is $f_p a$. This requires modifying the axial momentum equation as follows:

$$\begin{aligned} \text{blade force} - \text{swirl pressure force} &= \text{mass flow} \quad \Delta u \\ \frac{1}{2} \rho w^2 c_x N c dr - \frac{1}{2} \rho (2 f_p a \Omega r)^2 2 \pi r dr &= \rho u_0 (1 - f_p a) 2 \pi r dr \quad u_0 2 f_p a \end{aligned} \quad (2.2.25)$$

dividing by $\frac{1}{2} u_0^2 2 \pi r dr$

$$\begin{aligned} c_x \frac{N c}{2 \pi r} \frac{w^2}{u_0} - \left(\frac{2 f_p a \Omega r}{u_0} \right)^2 &= 4 f_p a (1 - f_p a) \\ \sigma c_x \frac{w^2}{u_0^2} &= 4 [f_p a (1 - f_p a) + (\lambda \mu f_p a')^2] \end{aligned} \quad (2.2.26)$$

The angular momentum equation becomes:

$$\begin{aligned} \text{blade torque} &= \text{mass flow} \quad \Delta u_{\theta r} \\ \frac{1}{2} \rho w^2 c_{\theta} N c r dr &= \rho u_0 (1 - f_p a) 2 \pi r dr \quad 2 f_p a' r \Omega r \end{aligned} \quad (2.2.27)$$

dividing by $\frac{1}{2} u_0^2 2 \pi r dr$

$$\sigma c_{\theta} \frac{w^2}{u_0^2} = 4 f_p a' \lambda \mu (1 - f_p a) \quad (2.2.28)$$

The tip loss factor f_p is given by;

$$f_p = \cos^{-1} \left(e^{\frac{B(\mu-1)}{2\mu \sin \phi}} \right) \cos^{-1} \left(e^{\frac{B(\mu-\mu_r)}{2\mu \sin \phi}} \right) \quad (2.2.29)$$

where the first expression defines a tip loss, and the second defines a hub loss which occurs when the blade root is located at some non-zero normalized radius μ_r . The derivation of the tip loss factor will not be shown in this thesis for brevity. Please refer to [55] for more details.

2.2.5 Implementation of BEM

The BEM equations were used in a non-linear sequential quadratic programming (SQP) optimization in Matlab to determine the optimal blade geometry and performance for a non-ducted tidal turbine in an unbounded flow. This approach was used instead of the traditional fixed point iteration method to be consistent with the DuctBEM model described in section 2.3, for which a stable formulation for fixed point iteration could not be found.

The optimization used the axial/tangential induction factors and blade solidity at $N = 42$ discrete points (a_i, a'_i, σ_i) along the blade as the design variables. The algorithm used the following set of equations to define the blade forces and turbine performance based on the induction factors and solidity:

$$\phi_i = \tan^{-1} \left(\frac{1 - a_i}{\lambda \mu_i (1 + a'_i)} \right) \quad (2.2.30)$$

$$\frac{w_i}{u_0} = \sqrt{(1 - a_i)^2 + \lambda^2 \mu_i^2 (1 + a'_i)^2} \quad (2.2.31)$$

$$c_{x_i} = c_l \cos \phi_i + c_d \sin \phi_i \quad (2.2.32)$$

$$c_{\theta_i} = c_l \sin \phi_i - c_d \cos \phi_i \quad (2.2.33)$$

$$c_{T_i} = \sigma_i c_{x_i} (w_i/u_0)^2 \quad (2.2.34)$$

$$c_{P_i} = \sigma_i c_{\theta_i} (w_i/u_0)^2 \lambda \mu_i \quad (2.2.35)$$

The optimal lift-to-drag ratio was assumed to be achieved over the entire turbine blade. This occurs with a constant angle of attack α and corresponding c_l and c_d . Thus these parameters were defined *a priori*. The tip speed ratio λ was also defined *a priori* and the optimal tip speed ratio was found by manual tuning. The tip loss factor was found using equation 2.2.29

The objective function was defined as the negative of the sum of the local power coefficients at each annulus. The negative was taken because *fmincon* is formulated to minimize the objective function.

$$J = - \sum_{i=1}^N c_{p_i} \quad (2.2.36)$$

Note that this is not the same as the total power coefficient C_P defined in equation 2.2.24. It was found that using C_P produced non-smooth profiles of induction and blade properties, and less-optimal results than equation 2.2.36. The reason for this is not fully understood but it is thought to be due to the uneven weighting of the contribution of each annulus towards the total power. Since the inner annuli are weighted less than the outer ones, the optimization algorithm would not recognize small decreases in the power of the inner annuli, because these changes would be dwarfed by those of the outer annuli. Indeed, the non-smooth behavior was limited to approximately $r/R < 0.3$, which supports this explanation. In any case, since the model does not capture any interaction effects between adjacent annuli, maximizing each individual c_{p_i} is the same as maximizing their sum, which is also the same as maximizing a weighted sum (i.e. C_P).

The *fmincon* function uses the convention $c_{eq_i} = 0$ for equality constraints, which were defined to constrain the model to adhere to the axial and angular momentum balances defined by equations

	C_T	C_P
no tip loss	0.9492	0.5373
with tip loss	0.9233	0.5086
% change	-2.73 %	-5.34%

Table 2.2: Summary of the impact of tip loss on rotor thrust and power

2.2.26 and 2.2.28:

$$c_{eq\{1:N\}} = \sigma_i c_{x_i} w_i^2 / u_0^2 - 4[f_{p_i} a_i (1 - f_{p_i} a_i) + (\lambda \mu_i f_{p_i} a_i')^2] \quad (2.2.37)$$

$$c_{eq\{N+1:2N\}} = \sigma_i c_{\theta_i} w_i^2 / u_0^2 - 4f_{p_i} a_i' \lambda \mu_i (1 - f_{p_i} a_i) \quad (2.2.38)$$

Once the optimization was complete, the total thrust and power coefficients were found using the weighted sum defined by equation 2.2.24.

2.2.6 Evaluation of Tip Loss for Non-Ducted Tidal Turbines

The impact of tip loss on the performance of an optimized non-ducted turbine was assessed by comparing the BEM optimization results for a blade using the DU91-W2-250 airfoil. It is felt that the relatively low maximum lift-to-drag ratio ($l/d = 40$) of this airfoil is representative of the achievable performance of tidal turbine blades which require adequate thickness to withstand high loads, and may be subject to bio-fouling in operation. The optimal performance with tip loss was found by varying the specified tip speed ratio. The value $\lambda = 3.0$ (within ± 0.25) gave the highest C_P . The optimal performance neglecting tip-loss was found at the same tip speed ratio by fixing $f_p = 1$ in the algorithm. The thrust and power coefficients from these runs are summarized in table 2.2.

Thus the expected reduction in optimum power which arises due to tip loss for turbines using the selected airfoil is approximately 5.3%, and this was associated with a 2.7% reduction in the rotor thrust. This result was later applied in analyzing the power production potential of the Minas Passage in the Bay of Fundy, described in section 3.6.

2.3 Blade Element Momentum Theory for Ducted Turbines

It was desired to extend the capability of BEM to ducted rotors. The primary motivation for doing so was to provide a reasonably accurate method for analyzing and designing ducted turbines without the computational expense of using CFD simulations. The standard BEM treatment of the balance between axial momentum change and axial force represented by equation 2.2.14 is not valid for ducted turbines because of the duct’s influence on the flow. Thus, a new formulation was required to define the relationship between the velocity at the rotor and the turbine thrust. The strategy taken was to parameterize the effect of the duct on the flow in terms of efficiency and pressure coefficient terms. These terms were determined for a range of duct geometries through CFD simulation. Curve fitting techniques were then used to define the efficiency and pressure coefficients based only on key features of the duct geometry. The resulting parameterized duct model could then be implemented in a BEM framework. While CFD was used in determining the duct efficiency and pressure coefficient terms, the final DuctBEM model can be used without running further simulations. This provides a useful tool with reasonable accuracy for the preliminary design of ducted turbines, and which could be extended to study blade loading with dynamic inflow.

The mass flow increase provided by the duct (and thus the power augmentation for a given rotor area) is influenced by four primary factors: (1) the diffuser expansion ratio A_4/A_3 , (2) the degree of flow separation from the diffuser surface, (3) the base pressure reduction at the diffuser exit caused by obstruction of the flow, and (4) viscous losses within the entire duct.

2.3.1 Literature Review

Analytical models have been developed to characterize the performance of ducted turbines by Lilley and Rainbird [10], Foreman et al.[11], Lawn [48], van Bussel [49] and Jamieson [56]. However, all of these models require empirical parameters to capture the effects of flow separation, base pressure, and viscous loss. At present, there is little experimental or numerical data to support a fundamental understanding of how these factors vary with changes to duct geometry.

The models presented by Jamieson and van Bussel are based on a modified version of the standard axial flow actuator disk momentum analysis [54]. Van Bussel’s model was developed to identify ideal duct performance and thus neglects viscous loss and flow separation effects. The model includes a duct expansion parameter and a base pressure speedup factor. Jamieson’s model calculates an ideal zero-thrust induction factor at the rotor plane. This parameter incorporates the diffuser expansion ratio and base pressure effects (at the zero thrust condition). Jamieson employed an efficiency term to account for “non-ideal” duct geometries, where the ideal duct would have no flow separation, a constant base pressure coefficient and zero viscous loss. The models by Jamieson and van Bussel provide a useful extension of the standard actuator disk theory to the ducted case, but do not identify the physical parameters governing the duct performance in concrete terms.

The model by Lilley and Rainbird identifies the major effects of base pressure and viscous loss but is more complex and more reliant on assumptions than models by Lawn and Foreman et al. The model put forth by Lawn, which is similar to prior work by Foreman et al., provides a straightforward analysis of the pressure variation through the duct and identifies each major factor with a unique

term. It is relatively straightforward to identify the base pressure, flow separation and viscous effects from CFD results and to apply them to Lawn's model. As well, it was straightforward to incorporate this model into a blade element momentum (BEM) framework for the purpose of blade design and fatigue analysis once the empirical coefficients were calibrated from actuator disk CFD simulations.

2.3.2 The 1D Duct Performance Model

The duct performance model framework by Lawn [48] was adapted slightly for this thesis. The model analyzed only the axial flow through the turbine. Unlike the typical BEM treatment, this initial model did not consider a series of concentric streamtubes, but only considered one streamtube enclosing the entire flow passing through the turbine rotor. Due to this, the flow velocity was assumed to have no variation in the radial direction, and could only vary axially. Only the thrust of the rotor was considered (not the torque), and this force was also assumed to be uniform radially. Thus, all of the velocities, pressures, forces and model parameters found by this model are radial averages, indicated by an overbar.

The model was developed by analyzing the variation of pressure through the duct. From the freestream condition (p_0, u_0) the flow either expands or contracts approaching the rotor disk plane (station 2 in figure 2.6). The variation in pressure is related to the change in velocity by Bernoulli's equation modified with an efficiency term:

$$\bar{c}_{p,02} = \frac{\bar{p}_2 - \bar{p}_0}{\frac{1}{2}\rho u_0^2} = \bar{\eta}_{02} \left(1 - \frac{\bar{u}_2^2}{u_0^2} \right) \quad (2.3.1)$$

which parameterizes viscous loss in the inlet section. Note that this definition of the efficiency is based on a flow expansion (by convention) and therefore will have values greater than unity when used for an inlet contraction with viscous loss.

The pressure change across the actuator disk is defined according to the standard definition of the thrust coefficient C_T :

$$C_T = \frac{\bar{p}_2 - \bar{p}_3}{\frac{1}{2}\rho u_0^2} \quad (2.3.2)$$

Note that Lawn [48] defined a turbine resistance coefficient relating the thrust to the local velocity at the rotor plane (u_2) however this approach has not been followed in this analysis to facilitate a more straightforward comparison to CFD results.

The pressure change through the diffuser is found using an analogous equation to the duct inlet:

$$\bar{c}_{p,34} = \frac{\bar{p}_4 - \bar{p}_3}{\frac{1}{2}\rho \bar{u}_3^2} = \bar{\eta}_{34} \left(1 - \frac{\bar{u}_4^2}{\bar{u}_3^2} \right) = \bar{\eta}_{34} \left(1 - \frac{A_3^2}{A_4^2} \right) \quad (2.3.3)$$

Note that by continuity $\frac{\bar{u}_4}{\bar{u}_3} = \frac{A_3}{A_4}$ (and $A_2 = A_3$ since the actuator disk is assumed infinitesimally thin.)

The pressure difference between the far wake, defined where full expansion back to $p = p_0$ has occurred, and the diffuser outlet is parameterized as a base pressure coefficient $\bar{c}_{p,b}$. This definition reflects the assumption of full pressure recovery in the wake to the freestream value, and is an idealization required for this analytical model. In reality, as turbine arrays begin to extract

significant amounts of energy from the flow, the downstream pressure will be measurably reduced from the freestream value owing to the restricted domains of tidal channels.

$$\bar{c}_{p,b} = \frac{p_0 - \bar{p}_4}{\frac{1}{2}\rho u_0^2} \quad (2.3.4)$$

Summing the pressure changes from the undisturbed free stream to the far wake and equating to zero, it is then possible to define the following relationships:

$$\bar{\eta}_{02} \left(\frac{\bar{u}_2^2}{u_0^2} - 1 \right) + C_T - \bar{c}_{p,b} - \bar{c}_{p,34} \frac{\bar{u}_2^2}{u_0^2} = 0 \quad (2.3.5)$$

$$\frac{\bar{u}_2}{u_0} = \sqrt{\frac{\bar{\eta}_{02} + \bar{c}_{p,b} - C_T}{\bar{\eta}_{02} - \bar{c}_{p,34}}} \quad (2.3.6)$$

Defining the ideal turbine power extraction as the product of the turbine thrust and the radially averaged axial velocity at the rotor plane, the power coefficient is defined as:

$$C_{P_{ideal}} = C_T \frac{\bar{u}_2}{u_0} \quad (2.3.7)$$

The base pressure coefficient and efficiency terms are not generally known and need to be found experimentally or through simulations for a given duct geometry, which was done for the ducts D1-D10 with the results given in section 3.2.

2.3.3 Extending the Duct Model to Include Wake Swirl and Radial Variation

The initial 1D parameterization adapted from [48] was later expanded upon to allow for radial variation of the thrust coefficient, base pressure coefficient and diffuser efficiency. Radial variation of these terms was accounted for using the same strategy as BEM, which involves dividing the actuator disk into concentric annuli centered at r and of thickness dr . The previous model also neglected the pressure reduction associated with wake swirl, which was included using the same treatment for open flow turbines discussed in section 2.2.2.

To include the effect of wake swirl on the pressure variation through the duct, the standard BEM assumptions regarding tangential induction were used. Just downstream of the rotor, the tangential velocity is $2a'r\Omega = u_0\lambda\mu(2a')$. Given that the swirling wake causes a reduction in pressure, it has an influence on the axial momentum/force balance and hence the two sets of equations are coupled. This effect is accounted-for using a swirl pressure coefficient defined as:

$$c_{p,sw} = \frac{\frac{1}{2}\rho u_{\theta 3}^2}{\frac{1}{2}\rho u_0^2} \quad (2.3.8)$$

$$= 4(a'\lambda\mu)^2 \quad (2.3.9)$$

The model applies a local thrust coefficient c_T , a local base pressure coefficient $c_{p,b}$ and a local diffuser efficiency η_{34} to each individual annulus to account for radial variations. (The swirl pressure coefficient is also local to each annulus). The local diffuser efficiency and base pressure

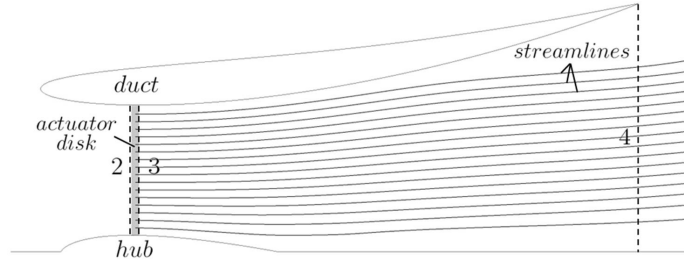


Figure 2.8: Depiction of dividing the flow using a series of concentric streamlines for determining the radial variation of η_{34} and $c_{p,b}$.

coefficients must be determined from simulation results or experimental data. This requires dividing the experimental/simulated flow using a series of concentric streamlines as depicted in figure 2.8, and determining the local pressures and velocities at stations 3 and 4 for each streamline. The local diffuser efficiency is then:

$$\eta_{34} = \frac{p_4 - p_3}{\frac{1}{2}\rho u_3^2 \left(1 - \left(\frac{A_3}{A_4}\right)^2\right)} \quad (2.3.10)$$

The simulations/experiments used in determining the base pressure coefficient and diffuser efficiency may or may not include tangential forcing terms. For example, porous disk type experiments [11, 12, 48] have no tangential forcing terms, while real rotor experiments [13] do. When the duct parameters are found from simulations/experiments with tangential forcing, the pressure measurements at the duct exit p_4 are influenced by both base pressure and wake swirl effects, giving:

$$c_{p,b} + c_{p,sw} = \frac{p_0 - p_4}{\frac{1}{2}\rho u_0^2} \quad (2.3.11)$$

Thus, when determining $c_{p,b}$ from simulation results or experimental data, it is necessary to isolate the base pressure effect by measuring the wake swirl velocity just downstream of the rotor plane. Then the base pressure coefficient can be found using:

$$c_{p,b} = \frac{p_0 - p_4}{\frac{1}{2}\rho u_0^2} - \frac{u_{\theta,3}^2}{u_0^2} \quad (2.3.12)$$

The axial induction factor can then be found using the following equation:

$$(1 - a) = \sqrt{\frac{1 - c_T + c_{p,b} + c_{p,sw}}{1 - c_{p,34}}} \quad (2.3.13)$$

2.3.4 The Combined DuctBEM Model

The duct performance model was incorporated into the blade element momentum method by replacing the standard axial momentum/force balance with equation 2.3.13. The combined model maintains the standard treatment for the angular momentum/torque balance given by equation 2.2.11. In the DuctBEM model, c_T is found based on blade forces using equation 2.2.17, $c_{p,sw}$ is

determined using equation 2.3.9, and $c_{p,b}$ and η_{34} are found using curve fits to simulation results or experimental data. The data points for these curve fits are determined from simulations or experiments using equations 2.3.10 and 2.3.12. The fidelity of the model depends on the accuracy of these curve fits, while its generality depends on the range of operating conditions and duct geometries used to derive the model.

During this thesis work, the duct geometries described in section 2.1 were used in CFD simulations to determine the inlet efficiency, diffuser efficiency and base pressure coefficient using the initial 1D duct treatment in section 2.3.2. The efficiency terms and base pressure coefficients were then defined in terms of geometric features of the ducts using curve fitting. This is described in detail in section 3.2. The result was a highly general model, in that it covered a wide range of duct geometries and operating thrust coefficients, but which lacked some accuracy because it assumed 1D flow and neglected all radial variations by taking area averages. A much more detailed and accurate determination of the model coefficients which included the radial variation of the duct performance parameters was done for the D4 duct with a specific rotor loading configuration (section 3.4). This was used to test that the DuctBEM model produced physically realistic solutions. Much effort would be required to develop a detailed and accurate duct performance model valid over a range of rotor loading configurations and duct designs. Thus it was useful to observe the relative error produced by making various simplifying assumptions in the development of the duct performance model. This is described in section 3.4.

2.3.5 Evaluating Turbine Performance for a Defined Blade

A stable formulation for equations 2.2.11 and 2.3.13 using fixed point iteration has not been determined to date. Instead, an optimization algorithm provided by Matlab called *fmincon* was used to solve the coupled equations formulated as a non-linear optimization problem. This provided the ability to determine the performance of a pre-defined blade and duct (dealt with in the current section), as well as the option to optimize a blade for a given duct (dealt with in section 2.3.6). In the optimization, the domain was discretized radially using $N+1$ nodes, and therefore $i = \{1 \dots N\}$ concentric annuli.

For determining the performance of a pre-defined blade geometry, the active variables in the optimization were the axial and tangential induction factors at each annulus (a_i, a'_i) , where the subscript i refers to the i^{th} annulus. The set of equations used to define the turbine performance at

each iteration is summarized below:

$$\phi_i = \tan^{-1} \left(\frac{1 - a_i}{\lambda \mu_i (1 + a'_i)} \right) \quad (2.3.14)$$

$$\frac{w_i}{u_0} = \sqrt{(1 - a_i)^2 + \lambda^2 \mu_i^2 (1 + a'_i)^2} \quad (2.3.15)$$

$$\alpha_i = \phi_i - \beta_i \quad (2.3.16)$$

$$c_{li} = c_l(\alpha) \quad (2.3.17)$$

$$c_{di} = c_d(\alpha) \quad (2.3.18)$$

$$c_{xi} = c_l \cos \phi_i + c_d \sin \phi_i \quad (2.3.19)$$

$$c_{\theta i} = c_l \sin \phi_i - c_d \cos \phi_i \quad (2.3.20)$$

$$c_{Ti} = \sigma_i c_{xi} (w_i/u_0)^2 \quad (2.3.21)$$

$$c_{Pi} = \sigma_i c_{\theta i} (w_i/u_0)^2 \lambda \mu_i \quad (2.3.22)$$

The optimization used equations 2.3.13 and 2.2.11 as equality constraints. These were reformulated to adhere to the *fmincon* convention $c_{eq,i} = 0$ as follows:

$$c_{eq,\{1\dots N\}} = 1 - c_{Ti} + c_{p,b_i} + c_{p,sw_i} - (1 - c_{p,34_i})(1 - a_i)^2 \quad (2.3.23)$$

$$c_{eq,\{N+1\dots 2N\}} = a'_i 4 \sin \phi_i \cos \phi_i - (1 + a'_i) \sigma_i c_{\theta i} \quad (2.3.24)$$

The objective function was specified as an error function based on the axial momentum equation:

$$J = \sum_{i=1}^N \{1 - c_{Ti} + c_{p,b_i} + c_{p,sw_i} - (1 - c_{p,34_i})(1 - a_i)^2\} \quad (2.3.25)$$

Note that this objective function was somewhat redundant since it is effectively the same as the axial momentum constraint. The *fmincon* function requires an objective function to be specified and this seemed the most appropriate. Note that due to this redundancy, it is possible to omit the axial momentum constraint represented by equation 2.3.23 however doing so resulted in slower convergence of the algorithm, and less smooth profiles of induction along the blade; although the computed C_P and C_T were essentially unchanged. The algorithm seeks to minimize the objective function while satisfying the constraints within a user defined tolerance. It was found that a tolerance of 1×10^{-5} allowed the optimization to run quickly, without diminishing the accuracy of the optimal solution.

The solution strategy employing *fmincon* has a significant advantage over traditional fixed-point-iteration schemes in that it enforces the constraints set by equations 2.3.23 and 2.3.24 at *all* annuli simultaneously, whereas fixed-point-iteration solves each annulus independently of all others. This all-at-once approach allows model parameters to depend on quantities which are integrated over the entire streamtube (i.e. C_P and C_T). This was important in applying the 1D empirical duct performance model described more fully in section 3.2 because it defines the base pressure coefficient based on the global thrust coefficient C_T . It is also conceivable that within this all-at-once framework the interaction of adjacent annuli through viscous shear and turbulent mixing could be approximated,

although this would likely take a rather crude form.

2.3.6 Optimizing the Blade Profile

The above optimization algorithm was easily adapted to optimize the blade geometry for maximum power. Since for this type of problem, the blade geometry is not known *a priori*, an additional active variable was required for the optimization procedure. In this thesis, the local solidity σ was used. Note that as in the implementation of the non-ducted BEM method, the optimum lift-to-drag ratio $(l/d)_{max}$ was assumed to be achieved over the whole blade length. This was accomplished by prescribing $\alpha = \alpha_{opt}$, (the optimum angle of attack, which depends on the chosen airfoil) for all radial locations. Due to this treatment, the blade twist is not required as an active variable, but is rather determined in a post-processing step.

The domain was divided into N radial segments, and the active variables for the optimization were (a_i, a'_i, σ_i) with $i = \{1 \dots N\}$. Note that as before the tip speed ratio was specified *a priori* although this could be included as an additional design variable. This is a very tractable problem even for fairly large N . In this work $N = 42$ was used and the Matlab algorithm ran in approximately 3 seconds on a desktop computer.

It was found that in some situations, an additional constraint had to be implemented to bound the thrust coefficient C_T to stay within reasonable limits.

$$C_T \leq C_{Tmax} = 1.2 \quad (2.3.26)$$

This limit was used to constrain the optimization algorithm from searching infeasible areas of the design space with very large rotor thrust.

Thus, the constraints consisted of equality constraints represented by equations 2.3.23 and 2.3.24 and the inequality in equation 2.3.26. As done in implementing the non-ducted BEM method, the objective function was defined as the negative of the sum of the local power coefficients at each annulus.

$$J = - \sum_{i=1}^N c_{p_i} \quad (2.3.27)$$

A CFD-based blade optimization method was also developed and is described in section 2.4.9. The DuctBEM blade optimization technique described in this section was applied to a selected duct geometry and the resulting performance and blade geometry were compared to the CFD-based method in section 3.4.

2.4 Actuator Disk CFD Simulation

Computational fluid dynamics (CFD) simulations were used to determine the impact of a range of duct geometries (described in section 2.1) on the performance of tidal turbines. CFD was also used to assess free surface effects (section 2.5) and blockage effects (section 2.6). CFD provides a very versatile environment for analyzing ducted turbines because it offers the ability to resolve the relatively poorly-understood influence of ducts on the flow explicitly, while resolving the better understood influence of the turbine rotor using a simplified representation called an actuator disk approach.

The actuator disk CFD approach used in this thesis has been successfully applied by a number of researchers and is widely recognized as a valid modeling tool. In a review paper on the state of the art of wind turbine aerodynamics, Hansen *et al.* [52] identified fifteen papers using the actuator disk CFD approach. Since then, many more researchers have used the approach to study a wide variety of phenomena. Examples include: Sun *et al.* [27] who studied the interaction of free-surface deformation and tidal power extraction, Harrison *et al.* [36] who modeled tidal turbine wake recovery and Singh and Dinavahi [57] who performed shape optimization of a ducted propulsion system. The actuator disk CFD approach produces results which typically agree very well with experimental data. Mikkelsen [39] for example, showed a very good agreement between CFD results and experimental data for the Nordtank NTK 500/41 wind turbine with LM 19.1m blades. More recently, Réthoré, *et al.* [58] showed that the actuator disk CFD flowfield agrees very well with the exact analytical solution of the inviscid flow through an actuator disk provided by Conway [59] for a turbine operating with a thrust coefficient of $C_T = 0.4484$.

This method avoids resolving the turbine blades explicitly, instead defining the forces exerted by the blades on the flow via momentum source terms which are added to the discretized Navier-Stokes equations within a defined region in the simulation domain. This region takes the form of a disk of the same radial extent as, and located coincident with the turbine rotor, as pictured in figure 2.9. The blade forces are distributed uniformly in the azimuthal (θ) direction, but are allowed to vary radially. This is very similar in concept to blade element momentum theory, except that the relationship between the applied force and the change to the momentum of the flow is solved through numerical simulation which includes far fewer empirically based corrections than used in BEM. Thus CFD simulations explicitly resolve viscous effects, wake expansion, radial flows, and swirl effects, which are either neglected or corrected-for in BEM models. CFD simulations resolve the influence of ducts explicitly. The actuator disk approach neglects discrete blade effects because the blade forces are uniformly distributed in the azimuthal direction. For ducted turbines, this has been shown to be an acceptable approximation because the dominant flow structure responsible for discrete blade effects (i.e. tip vortices) do not form due to the presence of the duct [16]. For non-ducted turbines, empirical corrections based on the Prandtl tip loss model have been formulated [60] for application to the actuator disk CFD method.

Most applications of this approach have involved evaluating the performance of turbines with existing blade profiles, and calculate the blade forces based on the local angle of attack and relative flow velocity. The implementation in this thesis is somewhat different, in that it defines the forces

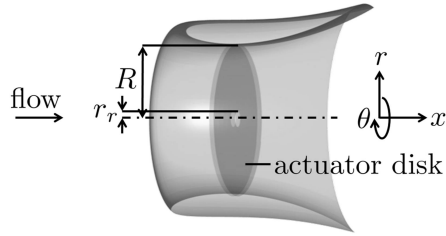


Figure 2.9: duct and actuator disk

of the rotor in terms of a user-defined thrust distribution. The torque is then found based on the evolving flow direction, and a prescribed rotor speed and airfoil lift-to-drag ratio. This allows CFD-based turbine optimization to be conducted in a search space consisting of very few design variables (in this thesis only three were used). This is very important because each function evaluation (i.e. simulation) takes a significant amount of time to complete, and an increased number of design variables will always increase the number of function evaluations required to arrive at an optimal solution drastically, regardless of the optimization algorithm used.

This section describes the implementation of the actuator disk method in a commercially available computational fluid dynamics (CFD) solver. Initially, the method only applied a thrust force to the flow, neglecting the rotor torque. Power was calculated as the product of thrust and local axial velocity. This implementation represented the *ideal* rotor performance. This initial implementation was used in studies of ducted turbine extraction efficiency (section 3.1) and in determining duct performance parameters for an empirical duct model (section 3.2). The method was later extended to include rotor torque, and power was then calculated as the product of torque and rotor speed. This extended version was used by an automated search algorithm which was used to determine the optimal rotor loading, tip speed ratio and blade geometry for an arbitrary duct (section 2.4.9). The search algorithm was later extended to include additional constraints and a different objective function (section 2.6.9), and then used in a case study of the potential power extraction from Minas Passage.

This section is organized as follows. First the solver and governing equations, turbulence closure, momentum source terms, simulation domain and boundary conditions are described. Subsequent sections deal with the calculation of rotor thrust and power, calculation of blade geometry, mesh definition, grid convergence study, validation studies, and the CFD-based blade optimization algorithm.

2.4.1 Software and Governing Equations

The actuator disk method was implemented in the general purpose CFD solver ANSYS CFX. A brief summary of the solver properties is given here, please refer to the product documentation [61] for more details. CFX uses a finite volume Navier-Stokes solver formulated in primitive variables (velocity and pressure). The advection scheme chosen for all simulations was the “high resolution” option, which is a blend between the 2nd order accurate central-difference-scheme CDS and the 1st

order accurate upwind scheme, where the blend factor is determined throughout the simulation and favors the CDS scheme except in situations where the stability of the solution may be compromised. CFX uses a co-located grid and avoids even-odd decoupling with a modified Rhie/Chow interpolation. The software uses a fully implicit discretization and a coupled solver which uses an incomplete lower upper (ILU) factorization technique. This is an iterative solver which approaches the exact solution to the discretized equations over the course of many iterations. This approach allows the specification of a timestep for steady state simulations, however this term serves only to underrelax the governing equations. The solver is accelerated using an algebraic multigrid technique called additive correction.

The software has options for a variety of simulation approaches, however the Reynolds-averaged Navier Stokes (RANS) equations were used for all simulations presented here. The flow was assumed to be incompressible, which is certainly valid for hydro-kinetic turbines. As well, simulations always sought steady state solutions, which by definition neglect variations in time. For steady, incompressible flows, the RANS equations can be expressed in a compact form using Einstein notation:

$$\frac{\partial \bar{u}_i}{\partial x_i} = 0 \quad (2.4.1)$$

$$u_j \frac{\partial \bar{u}_i}{\partial x_j} = \frac{\partial}{\partial x_j} \left[-\frac{\bar{p} \delta_{ij}}{\rho} + \nu \frac{\partial \bar{u}_i}{\partial x_j} - \overline{u'_i u'_j} \right] + \frac{\bar{S}_i}{\rho} \quad (2.4.2)$$

where $\delta_{ij} = 1$ for $i = j$ and equals zero otherwise. S_i is a momentum source term, used to impose the blade forces on the flow as described in section 2.4.3.

The simulations in this thesis also neglected thermal effects, allowing the energy equation to be neglected. Thus, the dissipation of turbulent kinetic energy did not contribute to heat production, nor did viscous shear. The impact of heat production is negligible because as demonstrated by [62], the heat produced by a turbine is insufficient to cause a noticeable temperature increase.

2.4.2 Turbulence Model

The Reynolds averaging process introduces additional stress terms (Reynolds stresses $\overline{u'_i u'_j}$) into the instantaneous Navier-Stokes equations, as documented in numerous CFD texts such as [63]. The Reynolds stresses are modeled using a turbulence model and several options exist. In all simulations presented here, the k - ω SST model by Menter [64] was used due to its well documented [65–68] superior performance in adverse-pressure gradient flows compared to other two-equation turbulence closures. The choice to use the SST model is discussed in more detail in [44]. The turbulence model must perform well in adverse pressure gradient flows, because the diffuser section of the duct creates a strong adverse pressure gradient as the flow expands.

While the SST model gives the best performance in this type of flow, compared to other two-equation closures, it is known to produce inaccurate results for massively separated flows, which are inherently unsteady. This is a limitation of using steady RANS simulations, and results must be treated with caution when large separated regions occur. This is a concern for some of the simulations, which produced large separated flows in the duct diffusing section. Note that from a design perspective such flow behavior is undesirable because it compromises performance and creates

undesirable cyclic loading. Thus, accurate modeling of such flows is not critical for design work or analyzing well-designed machines, as long as the onset of unstable separation can be detected. Note that large unsteady separated regions can be modeled more accurately using large eddy simulation (LES) or scale adaptive simulation (SAS), as discussed in [68], however this has not been pursued due to the greatly increased computational expense compared to RANS simulation.

The SST model uses the eddy viscosity concept, which computes the Reynolds stress terms $\overline{u'_i u'_j}$ as being proportional to the mean rates of deformation:

$$\overline{u'_i u'_j} = -\nu \left(\frac{\partial \bar{u}_i}{\partial x_j} + \frac{\partial \bar{u}_j}{\partial x_i} \right) + \frac{2}{3} \rho k \delta_{ij} \quad (2.4.3)$$

where k is the turbulent kinetic energy per unit mass defined as:

$$k = \frac{1}{2} \overline{(u'_i)^2} \quad (2.4.4)$$

Note that this treatment applies an equal two-thirds of the turbulent kinetic energy to each of the normal Reynolds stresses (i.e. for $i = j$). This therefore assumes that the normal Reynolds stresses are isotropic, which is known to be erroneous even in simple two-dimensional flows. Nonetheless, eddy viscosity models have been extensively tested with surprisingly good results for a wide variety of flows. There is always a tradeoff between accuracy and computational expense, and eddy viscosity turbulence models balance these well within the present constraints on computational resources.

The SST turbulence model was developed as a combination of the ‘standard’ k - ϵ model most commonly attributed to Launder and Spalding [69] and the Willcox k - ω [70] model to take advantage of their strengths and mitigate their weaknesses. Namely, the k - ϵ model performed well for free shear flows but not in the viscous sub-layer of boundary layers. The k - ω model worked well in the viscous sublayer, but it was very sensitive to specified boundary conditions. The SST model uses a blending function F_1 to implement the k - ω model near no-slip boundaries, and a re-formulated version of the k - ϵ model outside of the boundary layer. The model solves a transport equation for the turbulent kinetic energy k ;

$$\frac{\partial k}{\partial t} + \bar{u}_i \frac{\partial k}{\partial x_i} = \frac{\partial}{\partial x_i} \left[\left(\nu + \frac{\nu_t}{\sigma_k} \right) \frac{\partial k}{\partial x_i} \right] + P_k + P_{k,b} - \beta' k \omega \quad (2.4.5)$$

where P_k is the shear production term defined below, and $P_{k,b}$ is the buoyant production term, which has been neglected for all simulations, except for the free surface simulations described in section 2.5.

$$P_k = \nu_t \frac{\partial \bar{u}_i}{\partial x_j} \left(\frac{\partial \bar{u}_i}{\partial x_j} + \frac{\partial \bar{u}_j}{\partial x_i} \right) \quad (2.4.6)$$

A second transport equation is solved for the specific dissipation ω :

$$\frac{\partial \omega}{\partial t} + \bar{u}_i \frac{\partial \omega}{\partial x_i} = \frac{\partial}{\partial x_i} \left[\left(\nu + \frac{\nu_t}{\sigma_\omega} \right) \frac{\partial \omega}{\partial x_i} \right] + \alpha \frac{\omega}{k} P_k + P_{\omega,b} + \beta \omega^2 + (1 - F_1) \frac{2}{\sigma_{\omega 2}} \frac{\partial k}{\partial x_i} \frac{\partial \omega}{\partial x_i} \quad (2.4.7)$$

The turbulent kinetic energy k and specific dissipation ω evolve as the solution progresses. Using dimensional arguments, it is possible to define the eddy viscosity using; $\nu_t = \frac{k}{\omega}$. The SST model also applies a limiter on ν_t to approximate the correct transport of the shear stress in boundary layers. Please refer to [64] for details. The eddy viscosity is then;

$$\nu_t = \frac{a_1 k}{\max(a_1 \omega, S F_2)} \quad (2.4.8)$$

where S is defined as an invariant measure of the strain rate;

$$S = \sqrt{2 S_{ij} S_{ij}} \quad (2.4.9)$$

$$S_{ij} = \frac{1}{2} \left(\frac{\partial \bar{u}_i}{\partial x_j} + \frac{\partial \bar{u}_j}{\partial x_i} \right) \quad (2.4.10)$$

The blending function F_1 is:

$$F_1 = \tanh(\arg_1^4) \quad (2.4.11)$$

$$\arg_1 = \min \left[\max \left(\frac{\sqrt{k}}{\beta' \omega y}, \frac{500 \nu}{y^2 \omega} \right), \frac{4 \rho k}{C D_{k\omega} \sigma_{\omega 2} y^2} \right] \quad (2.4.12)$$

$$C D_{k\omega} = \max \left(2 \rho \sigma_{\omega 2} \frac{1}{\omega} \frac{\partial k}{\partial x_i} \frac{\partial \omega}{\partial x_i}, 1 \times 10^{-10} \right) \quad (2.4.13)$$

The blending function F_2 is:

$$F_2 = \tanh(\arg_2^2) \quad (2.4.14)$$

$$\arg_2 = \max \left(\frac{2 \sqrt{k}}{\beta' \omega y}, \frac{500 \nu}{y^2 \omega} \right) \quad (2.4.15)$$

The coefficients used in the SST model are found by blending those belonging to the k - ω regime and those of the standard k - ϵ model according to:

$$\phi = F_1 \phi_1 + (1 - F_1) \phi_2 \quad (2.4.16)$$

where ϕ represents any of the coefficients in the SST model, ϕ_1 represents the coefficient tuned for the k - ω regime and ϕ_2 represents the coefficient from the transformed k - ϵ model. Note that in the k - ω regime the SST model uses a value of 1.176471 for the turbulent Schmidt number σ_{k1} whereas the original Willcox k - ω model used a value of 2. Otherwise the coefficients (as shown below) are identical.

$\alpha_1 = 5/9,$	$\alpha_2 = 0.44$
$\beta_1 = 0.0750,$	$\beta_2 = 0.0828$
$\sigma_{k1} = 1.176471$	$\sigma_{k2} = 1$
$\sigma_{\omega 1} = 2$	$\sigma_{\omega 2} = \frac{1}{0.856}$
$\beta' = 0.0900$	

2.4.3 Momentum Source Terms

The blade forces were included into the domain through the momentum source term S_i in equation 2.4.2. In CFX, the momentum source terms are defined on a per-unit volume basis. In this thesis, the rotor forces were defined in terms of a prescribed thrust loading. This differs from typical implementations of the actuator disk approach which define blade forces based on tabulated airfoil

lift and drag coefficients and the evolving flow velocities. For a uniform thrust loading, the axial momentum source term is given by:

$$S_{x,uni} = -\frac{C_T \rho u_0^2}{2t_d} \quad (2.4.17)$$

where C_T is the user-specified thrust coefficient and t_d is the finite thickness of the actuator disk region (which is a feature of the designed mesh).

The simulations in this thesis allowed for a thrust loading which varied linearly with radius r . This was implemented by defining a non-uniform loading coefficient C_{nu} , which is a ratio of the loading at $r = 0$ to the uniform loading. Thus, $C_{nu} > 1$ gives higher loading at the root than at the tip. Using this parameter, a rotor with an equivalent total C_T to the uniformly loaded case will apply a momentum source governed by:

$$S_x = S_{x,uni} \left[C_{nu} + \frac{3(R^2 - r_r^2)}{2(R^3 - r_r^3)} (1 - C_{nu})r \right] \quad (2.4.18)$$

It is possible to specify actuator disk simulations that only include axial forcing terms. This is consistent with the axial-only BEM formulation, and requires calculating power production from the product of the axial force and axial velocity. Such an approach represents ideal turbine performance, and was used for the studies presented in sections 3.1 and 3.2. The axial-only approach does not represent the true physics of a turbine which generates power from the blade torque and cannot be used for blade design because the azimuthal velocity of the flow is required to calculate the blade twist and chord distributions. Additionally, such an approach would not account for the effects of blade drag or wake swirl.

The blade forces acting in the azimuthal direction can be defined in terms of the prescribed thrust loading, the evolving flowfield, and a specified lift-to-drag ratio as derived in the following. This formulation specifies the tangential force without *a priori* knowledge of the chord and twist distribution, allowing the optimum blade geometry to emerge from the simulation. Note that this differs from the typical implementation of the actuator disk CFD approach ([39] for example), where the blade geometry is pre-defined and the blade forces are found from the evolving flowfield and tabulated airfoil data. The novel approach taken here allows the rotor to be optimized in a search space consisting of only three design variables, which define the thrust loading distribution and rotor speed.

To describe the relationship between axial and tangential force, it is useful to observe a diagram of the relevant flow velocities and angles from the perspective of a turbine blade cross section (figure 2.10). The turbine blade generates lift l perpendicular to the resultant velocity w , and drag d parallel to w . The lift and drag are transformed into the (x, θ) frame by rotating through the inflow angle ϕ , as shown in figure 2.10.

The tangential and axial forces on the blade can be expressed by:

$$f_\theta = l \sin \phi - d \cos \phi \quad (2.4.19)$$

$$f_x = l \cos \phi + d \sin \phi \quad (2.4.20)$$

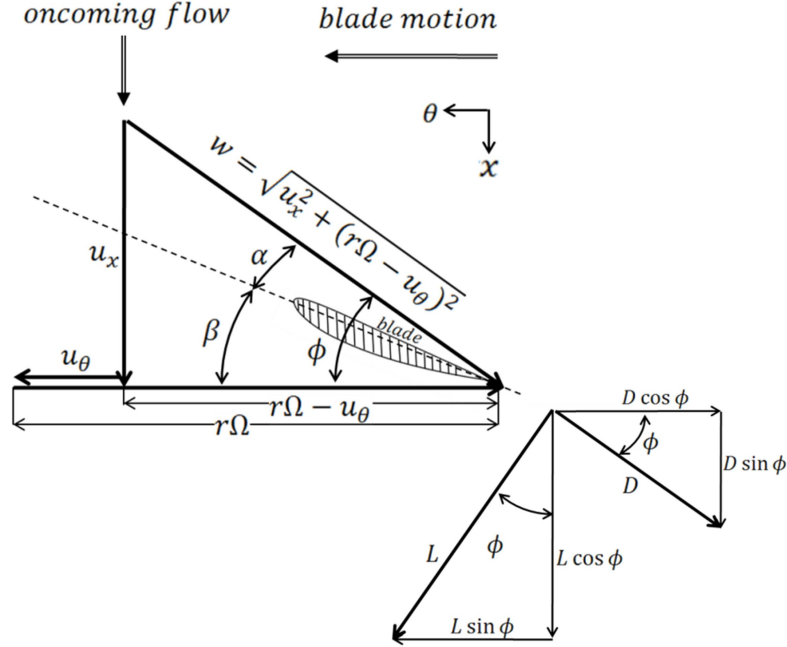


Figure 2.10: Blade flow angles and forces

For a given airfoil cross section the lift and drag vary with angle of attack α , and there is a certain value of α which maximizes the lift to drag ratio l/d . The optimum blade design is such that the local angle of attack at all radial locations will be the one that maximizes the lift to drag ratio. If a certain airfoil has been selected, and lift and drag polar data are available, the maximum l/d will be known. If multiple airfoil sections are to be used, then l/d can be defined as a function of r . The sin and cos terms in equations 2.4.19 and 2.4.20 can be defined as:

$$\sin \phi = \frac{u_x}{w}, \quad \cos \phi = \frac{r\Omega - u_\theta}{w} \quad (2.4.21)$$

It is then possible to define the ratio of tangential to axial force as a function of flow velocities, radial position and blade angular velocity:

$$\frac{f_\theta}{f_x} = \frac{\frac{l}{d}u_x - (r\Omega - u_\theta)}{\frac{l}{d}(r\Omega - u_\theta) + u_x} \quad (2.4.22)$$

This expression makes it possible to define the tangential force at any radial location along the blade as a function of the specified local axial force, blade angular speed, and the computed local velocity. The same fraction applies to the required momentum source term for the simulation:

$$S_\theta = S_x \frac{\frac{l}{d}u_x - (r\Omega - u_\theta)}{\frac{l}{d}(r\Omega - u_\theta) + u_x} \quad (2.4.23)$$

This methodology allows the turbine loading configuration to be fully described using only four user inputs; the thrust coefficient C_T , the non-uniform loading coefficient C_{nu} , the tip-speed-ratio

λ , and the airfoil lift to drag ratio $\frac{l}{d}$.

2.4.4 Simulation Domain and Boundary Conditions

Except for simulations involving blockage and free surface effects (described in section 2.5), the actuator disk simulations employed in this thesis assumed axi-symmetric flow, following the strategy of Hansen *et al.* [1]. The mesh was a 6° slice of the entire flow domain and periodic boundary conditions were enforced to simulate the entire 360° domain. The mesh was created by sweeping a 2D structured surface mesh through a 6° rotation in two elements. Strictly speaking, the axi-symmetric model only needs to be one element thick, however CFX requires at least two elements to calculate gradients when applying the periodic boundary condition. No model for the transition from laminar to turbulent flow was used as the flow was assumed to be turbulent along the entire duct surface.

The domain distances were normalized based on the duct length $L = 1m$. The inlet was $5L$ upstream of the duct leading edge and enforced a uniform velocity of $1m/s$ and turbulence intensity of 1%. The fluid was sea water with density $1024kg/m^3$ and dynamic viscosity $1.5 \times 10^{-3} Pa s$. The Reynolds number (Re) based on duct length was 7×10^5 . This Re and level of turbulence intensity were chosen for consistency with water-tunnel, and tow-tank tests. Actual turbines will be significantly larger and situated in faster flows of $2-5m/s$, with a higher turbulence intensity of approximately 10% [19]. Airfoil stall performance is typically improved at higher Re , so real devices using ducts with airfoil profiles may experience less flow separation than presented here. Hansen *et al.* [1] used $Re = 5 \times 10^7$ and as shown in section 2.4.8 obtained performance results very similar to the current study, indicating only a small Reynolds number dependence. Higher ambient turbulence intensity in real flows will also lead to less flow separation due to increased mixing within the boundary layer, as verified in section 2.4.7. Taken together, it is therefore likely that the relatively low Re and turbulence levels used in the current study provide a somewhat conservative estimate on achievable duct performance. The outlet was $10L$ downstream of the trailing edge and enforced $p = p_0$. As in [1] an inner radial boundary employing a free-slip condition was located at $0.05L$ to avoid a singularity in azimuthal velocity at the centerline. The outer radial boundary was located at $r = 5L$ and was treated using the opening for entrainment option, which approximates an infinite domain. The sensitivity of the simulated C_P to moving the outer radial boundary to $10L$ was less than 2% for the largest duct; and it was decided that the additional accuracy of moving this boundary did not justify the extra computational expense.

The actuator disk was simulated as a momentum sink where momentum source terms were applied to each computational element. The disk was located at the duct throat and had a finite thickness of t_d equal to 5% of the turbine radius r . A finite thickness was required by CFX since source terms are applied to a subdomain which must occupy a volume in space. Multiple elements were defined through the thickness of the disk to allow the velocity field to evolve smoothly through the disk.

2.4.5 Power, Thrust and Drag

After a simulation had run, the rotor thrust and power, as well as the duct drag were calculated in a post-processing step. Note that the rotor thrust was defined as a simulation input, and its calculation during post-processing was done to verify that the momentum source terms were applied correctly. As in the BEM method, both the local and total thrust and power coefficients were defined.

The total thrust coefficient C_T was calculated as the volume integral of the axial momentum source S_x over the simulation domain, normalized by the upstream flow kinetic energy density and rotor cross sectional area A_r .

$$C_T = \frac{\int_V S_x dV}{\frac{1}{2}\rho u_0^2 A_r} \quad (2.4.24)$$

The duct drag coefficient C_D was calculated as the integral of the wall shear stress τ_w and pressure p (acting in the axial direction) over the surface of the duct (using the built in *Force* function in CFX), normalized by the upstream kinetic energy density and rotor cross sectional area A_r .

$$C_D = \frac{\int_S Force(x) dS}{\frac{1}{2}\rho u_0^2 A_r} \quad (2.4.25)$$

Note that the duct drag was normalized with the rotor area to facilitate easy comparison to the thrust coefficient and to allow it to be added to C_T directly to determine a total axial force coefficient.

The total power coefficient C_P was calculated as the volume integral of the product of the azimuthal source term S_θ , radius r and rotational speed Ω , normalized by the upstream kinetic power density and rotor cross sectional area A_r .

$$C_P = \frac{\int_V S_\theta r \Omega dV}{\frac{1}{2}\rho u_0^3 A_r} \quad (2.4.26)$$

In the case of a purely axial momentum approach, which represents an ideal turbine, the total power coefficient was calculated as the volume integral of the product of the axial source term S_x and axial velocity u_x , normalized by the upstream kinetic power density and rotor cross sectional area A_r .

$$C_P = \frac{\int_V S_x u_x dV}{\frac{1}{2}\rho u_0^3 A_r} \quad (2.4.27)$$

The local thrust coefficient c_T was calculated as the total thrust on an annulus of radius r and infinitesimal thickness dr , normalized by the freestream kinetic energy density and the annular area $2\pi r dr$. This was found in relation to the user-specified rotor loading configuration.

$$\begin{aligned} c_T &= \frac{S_x t_d 2\pi r dr}{\frac{1}{2}\rho u_0^2 2\pi r dr} \\ &= \frac{\frac{-C_T u_0^2}{2t_d} \left[C_{nu} \frac{3(1-\mu^2)}{2(1-\mu^3)} (1 - C_{nu}) \mu \right] t_d}{\frac{1}{2}\rho u_0^2} \\ c_T &= C_T \left[C_{nu} + \frac{3}{2} \left\{ \frac{1 - \mu_r^2}{1 - \mu_r^3} \right\} (1 - C_{nu}) \mu \right] \end{aligned} \quad (2.4.28)$$

The local power coefficient c_P was defined as the power generated in the annulus, normalized by the freestream kinetic power density and the annular area. The local power was a product of the total tangential force on the annulus, the angular speed Ω and radius r .

$$c_P = \frac{S_\theta r \Omega t_d 2\pi r dr}{\frac{1}{2} \rho u_0^3 2\pi r dr} \quad (2.4.29)$$

$$= \frac{S_x t_d 2\pi r dr}{\frac{1}{2} \rho u_0^2 2\pi r dr} \frac{S_\theta r \Omega}{S_x u_0} \quad (2.4.30)$$

The first term of this expression is equal to the local thrust coefficient defined above. The second term is defined by equation 2.4.23. The last term can be defined in terms of the normalized radius $\mu = r/R$ and tip speed ratio $\lambda = R\Omega/u_0$. Thus, the local power coefficient can be defined in terms of the local thrust coefficient as:

$$c_P = c_T \left[\frac{\frac{l}{d} u_x - (r\Omega - u_\theta)}{\frac{l}{d} (r\Omega - u_\theta) + u_x} \right] \lambda \mu \quad (2.4.31)$$

2.4.6 Blade Properties

In the actuator disk CFD simulations, C_T , λ , C_{nu} and the blade lift to drag ratio $\frac{l}{d}$ were defined as input parameters. After a simulation converged, the blade geometry was calculated from the flow results and these input parameters.

The chord was found by considering a second definition (other than the one defined in equation 2.4.28) for the local thrust coefficient based on the axial force produced by a set of B turbine blades.

$$c_T = \frac{\frac{1}{2} \rho w^2 B c c_x dr}{\frac{1}{2} \rho u_0^2 2\pi r dr} \quad (2.4.32)$$

$$= \sigma c_x \left(\frac{w}{u_0} \right)^2 \quad (2.4.33)$$

where $\sigma = \frac{Bc}{2\pi r}$ is the blade solidity and $c_x = c_l \cos \phi + c_d \sin \phi$. The relative velocity w and inflow angle ϕ were known from the specified rotor speed Ω and the simulated axial and azimuthal velocities:

$$w = \sqrt{u_x^2 + (r\Omega - u_\theta)^2} \quad (2.4.34)$$

$$\phi = \arctan \left(\frac{u_x}{r\Omega - u_\theta} \right) \quad (2.4.35)$$

The lift and drag coefficients were taken from tabulated airfoil data, corresponding to the optimal lift-to-drag ratio. The blade solidity was found from equation 2.4.33, and then the chord was found for a chosen number of blades using the definition of solidity.

The blade twist distribution was more straightforward to find. For the selected optimum angle of attack α , known from airfoil data, the twist angle β (as shown in fig 2.10) is given by:

$$\beta = \phi - \alpha \quad (2.4.36)$$

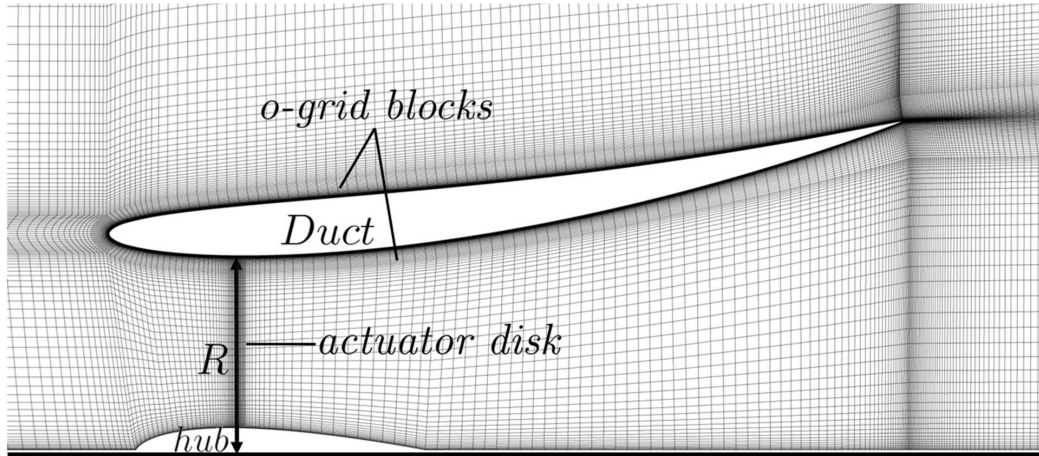


Figure 2.11: Surface mesh near the duct/hub profile for the D4 duct

2.4.7 Mesh Definition and Grid Convergence

To ensure minimal grid resolution error, the effect of grid refinement on the power coefficient was studied using the D2 duct geometry. Adequate resolution of the boundary layer along the duct was considered crucial. The grid refinement study was conducted following guidelines published in the Journal of Fluids Engineering [71].

Three meshes of progressively greater refinement were developed. The meshing strategy was a C-grid approach as shown in figure 2.11. The baseline mesh used a first layer spacing perpendicular to the duct surface of 0.08 mm in the boundary layer O-grid blocks except at the trailing edge, where the first layer spacing was 0.12 mm. The larger spacing at the trailing edge allowed more nodes to be concentrated in the expected region of flow separation and was not expected to be detrimental to the boundary layer solution due to normal boundary layer growth. The simulated y^+ value was less than 5 over the duct surface for all geometries except for where the flow accelerates around the leading edge, where it was maintained at less than 15. Note that CFX uses an automatic wall treatment to ensure a smooth transition between integrating-to-the-wall (strictly valid for $y^+ < 2$) and using wall functions (appropriate for approximately $y^+ < 30$). This transition allows some additional accuracy associated with integrating-to-the-wall, without the strict meshing requirement of $y^+ < 2$. Normal to the duct surface, the mesh spacing followed a bi-geometric expansion law with a ratio of 1.1. It is recommended [72] to use at least 10 nodes within the boundary layer to take advantage of the reduction of error when using this strategy. There were typically 20 or more nodes within the boundary layer for the simulations presented here. The O-grid blocks extended downstream to the domain outlet, providing a refined area over which the wake shear layer evolved.

Outside of the O-grid, the radial spacing (seen as vertical in figure 2.11) matched the O-grid outer layer spacing and expanded according to the bi-geometric law with a ratio of 1.1. The radial spacing at the domain centerline was 25 mm and at the outer radial bound it was 150 mm.

The axial spacing varied from 150 mm at the inlet (5L upstream of the leading edge) to 2 mm at the leading edge. This refinement was required to provide reasonable mesh spacing within the O-grid

Param.	$I_{inlet} = 1\%$	$I_{inlet} = 20\%$
C_{P1}	0.8141	0.8532
C_{P2}	0.8137	0.8531
C_{P3}	0.8126	0.8533
$C_{P_{ext}}^{21}$	0.8153	0.8533
GCI_{fine}^{21}	0.18%	0.03%
GCI_{med}^{21}	0.24%	0.04%
GCI_{coarse}^{21}	0.41%	0.01%

Table 2.3: Grid convergence study results. The GCI indicates the estimated discretization error for each mesh.

blocks at the leading edge. The axial spacing in the actuator disk was 2 mm. Through the interior of the duct the spacing was limited to a maximum of 12 mm. At the trailing edge, the spacing was 0.5 mm which provided refinement in the region where the fast exterior flow first meets the slower interior flow. At the domain outlet the spacing was 150 mm. The bi-geometric expansion law with a ratio of 1.1 was used to determine the mesh spacing between the locations described above.

A coarse mesh was created by multiplying all the spacings by 1.4 and reducing the number of nodes. A fine mesh was created in the same manner. The number of nodes in each 2D mesh were, $N_1 = 169164$, $N_2 = 85256$, $N_3 = 44451$.

For grid convergence, the power coefficient was chosen as the target variable. The first set of simulations was run using an inlet turbulence intensity of 1%. It was thought that the level of turbulence could affect the grid convergence results, so a second set of simulations were run with an inlet turbulence intensity of 20%. The grid convergence study results are summarized in table 2.3. In the table, C_{P_i} gives the resulting power coefficient calculated using the i^{th} mesh. The term $C_{P_{ext}}^{21}$ gives the expected value of C_P on a grid with infinite cells, found by Richardson extrapolation. The grid convergence index (GCI) gives an estimate of the discretization error for a given mesh.

The above results showed that even with the coarse mesh, the expected discretization error was less than 1%. It is likely that coarser meshes could be used without introducing much additional grid resolution error. The medium mesh was used for all further simulations to ensure reasonable grid convergence when applying this meshing strategy to different duct geometries, and because it gave reasonable simulation runtimes of 15 to 40 minutes when run with four partitions on an Intel Core™ i7 2.67 GHz CPU. It was expected to find an improved power coefficient for the 20% turbulence case (as can be seen in table 2.3) due to increased mixing in the boundary layer delaying the onset of flow separation in the duct.

2.4.8 Initial Validation Studies

The actuator disk CFD methodology was validated for the case of an ideal non-ducted rotor, reproducing the standard actuator disk theory well as shown in Fig. 2.12. For this comparison, only axial source terms were applied, and the power coefficient was calculated from the product of the axial force and axial velocity. This is consistent with the axial-only BEM treatment for ideal turbines.

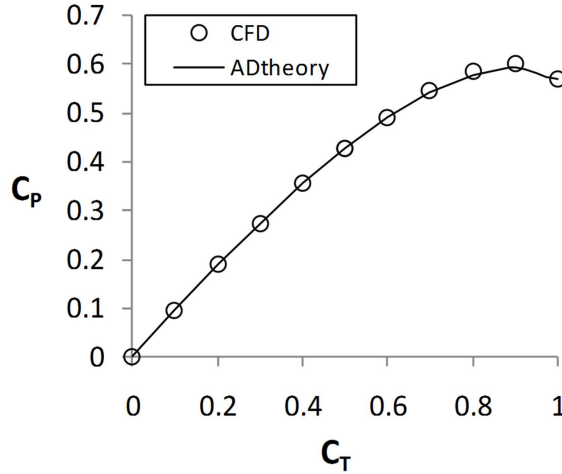


Figure 2.12: Comparison of CFD method to actuator disk theory for an ideal turbine with no duct

(Note that the Glauert empirical thrust correction [54] with $C_{T,1} = 1.7$ was applied to the theory curve for $C_T > 8/9$ to account for momentum theory breakdown at high thrust).

It should be noted that the axial only actuator disk CFD approach neglects wake swirl, discrete blade effects, and turbulence generation by the turbine. As a first order effect, wake swirl converts some of the kinetic energy of the upstream axial flow into tangential kinetic energy; this energy is therefore not captured by the turbine. As a second order effect, a high swirl velocity in the wake can produce a reduced pressure, assisting to draw more flow through the turbine. These effects are not typically large since the induced tangential velocity is typically low. Discrete blade effects will produce the well-known helical wake structure with an azimuthal variation of induction. For open flow (i.e. non-ducted) turbines this results in some loss of power due to induced drag from strong vortices trailed from the blade tips. Ducts inhibit the formation of tip vortices, so this is less of a concern for ducted turbines. Turbulence produced by the turbine blades will result in increased mixing downstream of the rotor, likely with minimal impact on the overall flowfield.

As a second validation, a simulation was run with the goal of reproducing the results of Hansen *et al.* [1]. This was done using the D2 duct geometry, which was a close replica of that used in [1]. For consistency with the prior work this initial simulation incorporated a small gap of width $0.08r$ between the outer radius of the actuator disk and the surface of the duct. This gap accelerated the boundary layer flow and delayed flow separation. This effect would not be expected in a real turbine with a discrete number of blades unless the solidity ratio was very high. Therefore, except where otherwise noted, the results presented in this thesis are for simulations where the actuator disk extended all the way to the duct. The effect of the gap is discussed further in section 3.2.3. The $C_P - C_T$ relationship was compared to results from [1] as shown in figure 2.13. The maximum C_P in the present simulation was 3% lower than the previous study. This discrepancy was likely due to minor differences in duct geometry, mesh and Reynolds number but was considered acceptable in terms of verifying the CFD methods employed relative to previous studies. Figure 2.13 also shows simulation results for the same duct without the gap, where the maximum power coefficient was 7%

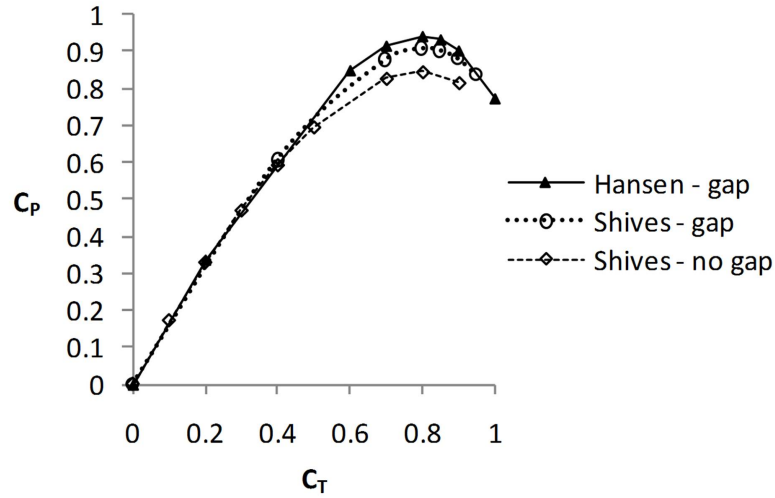


Figure 2.13: Comparison of present C_P to Hansen *et al.* [1] and effect of the gap on the baseline duct performance

less than the present case with the gap.

2.4.9 CFD-Based Blade Optimization Tool

Given that the CFD simulations defined the rotor loading configuration with only four input variables, it seemed reasonable to develop an automated algorithm that would progressively alter the input parameters to run simulations while searching for the configuration that gave maximum power.

A simple algorithm was developed to find the optimum combination of C_T , λ and C_{nu} for a selected lift to drag ratio (i.e. a selected blade airfoil). The design search space consisted of three dimensions (one for each design variable) and was discretized with user defined spacings. The algorithm was written in the Matlab environment. Starting from an initial guess of the optimum operating parameters, the algorithm runs an initial simulation. Then, with λ and C_{nu} fixed, C_T is increased by an increment of Δ_{C_T} and a new simulation is run. The algorithm then chooses whether to search towards higher or lower C_T , depending on whether C_P has increased or decreased from the first simulation. Simulations are then run at C_T intervals of Δ_{C_T} until a maximum C_P point is bracketed. It would be possible to use a polynomial curve fit to define the optimum C_T , however in the interest of keeping the required number of simulations to a minimum, the optimum C_T is taken as the best simulated value. C_T is then fixed, and the same strategy is used to optimize λ using increments of Δ_λ , and then C_{nu} using increments of $\Delta_{C_{nu}}$. The entire process is then iterated until no change in the optimized operating parameters occurs for an entire loop. Simple logic statements are used to avoid re-running simulations for combinations of C_T , λ and C_{nu} which have already been tested. The algorithm was later adapted to include a new objective function and additional constraints for use in a model which includes realistic boundary conditions for a tide-driven flow through a channel and accounts for blockage effects (section 2.6) and the final adapted version of this code is provided as Appendix A.

It is possible to run this algorithm with rather large increments to bracket the optimum design within a relatively large region of the search space. Then the chosen increments can be reduced to refine the search. The required resolution of the search space (Δ_{C_T} , Δ_λ , $\Delta_{C_{nu}}$) depends on the rate of change of the target variable (in this case C_P) with the design variables. This variation was found to be slow enough with the chosen increments for the ducted turbines studied in this thesis. A potential alternative to the described methodology is the golden section algorithm. Gradient based optimization is considered too complex and computationally expensive for this application since objective function gradients are not available in the CFD framework.

2.5 Modeling Blockage and Free Surface Effects

Power extraction from the tides is significantly different from wind power because tidal flows are bounded by channel sides and a dynamic free surface. Wind turbines extract power from the bottom layer of the atmospheric boundary layer. In wind power extraction the flow is bounded by the ground only. In contrast, tidal flows are bounded by the seabed, channel walls and the surface of the water. Tidal flows are driven by changes in sea surface height. When turbines are present in tidal flows, their presence will induce changes in the sea surface and therefore the flow field will be altered from the case of a flat surface. This section describes work done towards developing a CFD model that shows the relationship between power extraction and effects due to channel blockage and free surface deformation.

Blockage effects are most commonly studied in the context of correcting wind/water tunnel data to provide improved estimates of turbine performance in unbounded flows (for example [73]). For a given upstream flow velocity, a turbine contained in a tunnel of confined area has better performance than the same turbine in an unbounded flow. This occurs because the flow approaching the rotor cannot expand as much as in the case of an unbounded domain resulting in increased mass flow through the rotor, and increased power. In this thesis it is argued that turbines optimized for blocked flows could have significantly increased performance over those designed to operate in sparse arrays. Free-surface deformation complicates blockage effects because one of the walls of the space enclosing the flow is dynamic. The model in this section was primarily derived to determine the importance of including free surface deformation while modeling blockage effects. The model used for optimizing turbines in a real tidal channel described in section 2.6 used actuator disk CFD simulations with modified boundary conditions to conduct a more in-depth study of blockage effects on turbine power production.

The free surface model developed here provides insight into the interaction of power extraction and free-surface effects. A 2D analytical model of power extraction with a free surface has been developed by Whelan *et al.* [2]. In the model, the deformation of the free surface acts to increase the power extraction by accelerating the flow at the site of power extraction. Figure 2.14 shows the geometry and model parameters used in their analytical model.

A blockage ratio is defined as the ratio of turbine area to the upstream channel flow area (i.e. $B_r = s_t/z_1$). In the case of no free surface deformation, turbines in a constricted channel will enjoy a performance enhancement over turbines in an unbounded flow. This arises from the acceleration of the flow passing beside the turbine in a constricted domain. In the case where free surface deformation occurs, the analytical model by Whelan *et al.* predicts further performance enhancement in addition to the blockage effects. The degree to which free surface effects are important depends on the Froude number:

$$Fr \frac{u_0}{\sqrt{gz_1}} \tag{2.5.1}$$

which relates the freestream velocity u_0 to the surface wave propagation speed. Figure 2.15 shows the analytical relationship developed by Whelan *et al.* between the power coefficient and axial induction factor for a range of blockage ratios when $Fr = 0.22$. Maxima are also shown for the case when $Fr = 0$ and are lower than when free surface effects occur.

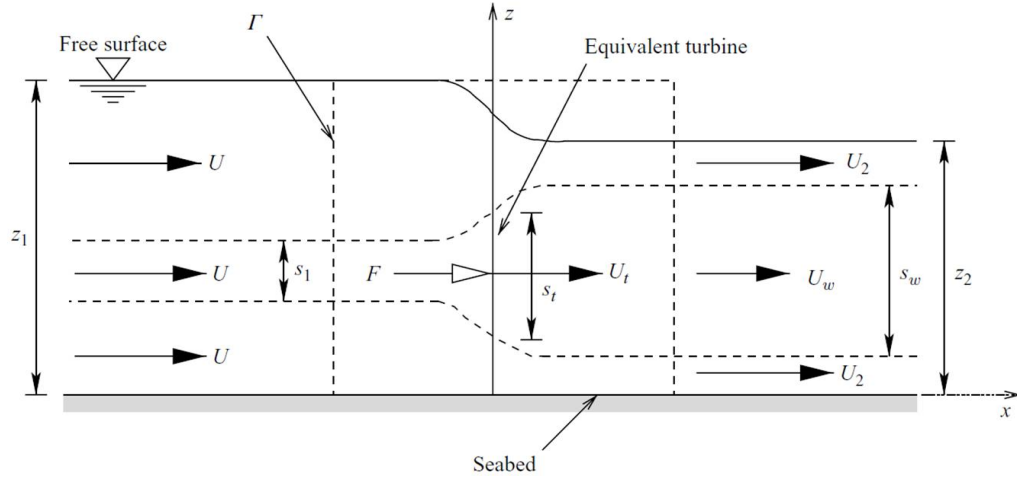


Figure 2.14: Schematic describing the analytical free surface model parameters (reproduced from [2])

While Whelan *et al.* did provide some experimental validation of their model, the experiments did not adequately prove the model's accuracy. Thus, a CFD based model was developed in the current work to resolve the impact of free surface deformation on turbine power with the goal of validating this analytical model, and of determining the importance of free surface deformation on predicting the power output of tidal turbines. It was also thought that if free surface deformation effects were important, such a model would be necessary for future design work.

2.5.1 Simulation Domain

The simulation domain is shown in figure 2.16. The domain was a rectangle 100m long by 2m tall. Power extraction was represented using an actuator strip, a 2D analog to the actuator disk used in the axi-symmetric model of section 2.4. The actuator strip was located at $x = 5m$ and spanned from $y = 0.25m$ to $y = 0.75m$. The strip thickness was 0.05m. The initial water level was 1m which gave a blockage ratio of 50%.

2.5.2 Boundary Conditions

At the inlet, a uniform velocity shared by both air and water of 1m/s was specified. The bottom boundary was treated as a free-slip wall. The top boundary used the opening for entrainment option with the relative pressure set to zero. The domain included a 'dissipation region' which extended the total domain length by 100m using very large streamwise spacing in the mesh, a strategy used by [74] in simulating free surface deformations near a submerged hydrofoil. This region was used to damp out waves propagating to and reflecting off of the outlet boundary, which can de-stabilize the convergence of the simulation. At the end of the dissipation region, the outlet specified a constant pressure of zero in the air phase and a hydrostatic pressure distribution in the water phase. The outlet condition required prescribing the water height, which was set to 1m. Using these boundary

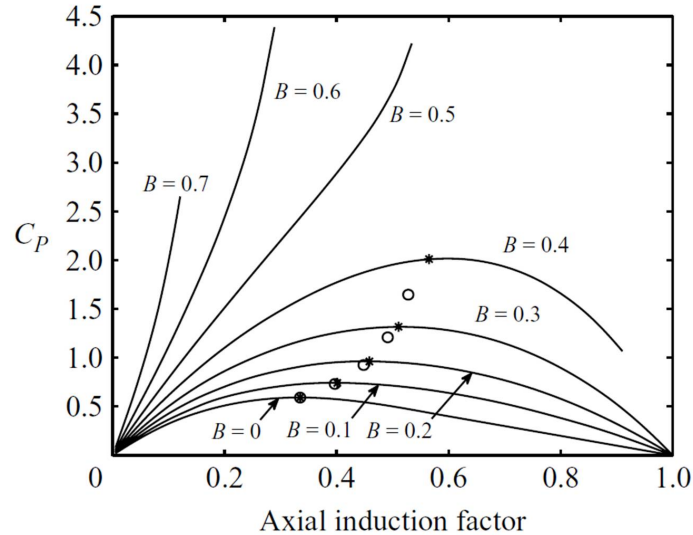


Figure 2.15: The effect of blockage ratio on power at $Fr = 0.22$: * denotes maxima at $Fr = 0.22$, \circ denotes maxima at $Fr = 0$. (reproduced from [2])

conditions, the change in water height between the far upstream and far downstream evolves as a change to the water height at the domain inlet.

Note that these boundary conditions are not exactly consistent with tidal power generation where the turbine and boundaries are fixed and the water is flowing at a given velocity. In reality, a no-slip bottom boundary would be required, and the air velocity would not in general be the same as the water at the inlet. The influence of the air on the water flow is expected to be negligible compared to the pressure gradients created by free surface elevation differences. The boundary conditions used in the model were chosen to maintain consistency with simulations by [74] and to ensure a stable convergence. Also, the free-slip bottom boundary condition allows comparison to the analytical model by Whelan *et al.* which neglects the bottom boundary layer. By setting the inlet air and water velocities equal and by using a homogeneous multiphase model convergence issues resulting

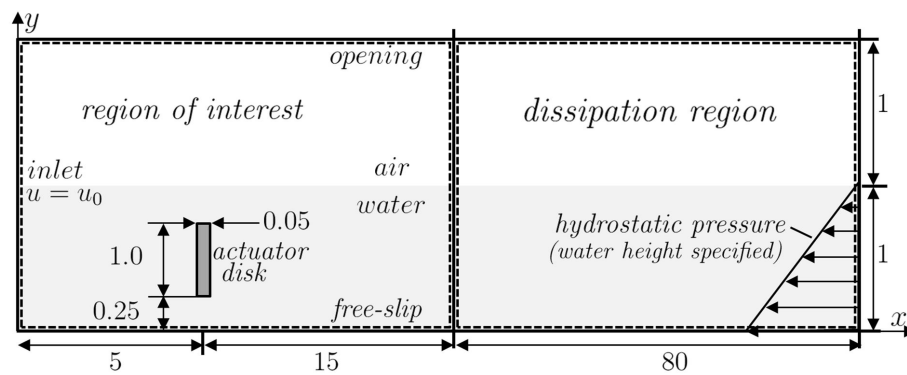


Figure 2.16: The domain and boundary conditions used for free surface simulations

from the generation of small wind waves were avoided.

2.5.3 Simulation Setup

The flow was modeled using distinct water and air phases. Buoyancy effects were included and the reference density was set to that of air ($1.184\text{kg}/\text{m}^3$). The gravity vector was set to $-9.81\text{m}/\text{s}^2$ in the y direction. The inlet Froude number was approximately 0.3, but its exact value depended slightly on the converged inlet water height. The air-water interaction was modeled using a homogenous multiphase strategy where the air and water phases share a single velocity field. Additional equations were solved for the volume fraction of each phase in each computational cell. The homogeneous option is recommended by the CFX modeling guide [61] when there is a distinct and well-defined phase interface. An inhomogeneous model is appropriate when there is entrainment of one phase in another, for example if there was splashing causing entrainment of air bubbles into the water. The inhomogeneous model requires more computational resource [61] and is not considered necessary for the present simulations. Additionally the inhomogeneous model was found to give poor convergence behaviour.

The flow was assumed to be isothermal since the heat generation by viscous dissipation is expected to give negligible temperature variation, especially considering the high heat capacity of water. Simulations were run with both the $k - \epsilon$ and SST turbulence models with no significant differences noted. It was decided that future simulations would use the SST model because its known applicability to separated flows would make it more appropriate if a duct were to be incorporated into the simulation. The power extraction region was modeled using an axial momentum source.

The upwind discretization scheme was used for the momentum, turbulence and volume fraction equations because it was expected to provide better stability than a higher order scheme. Because CFX retains transient terms for steady state calculations, a timestep must be specified.² A physical timestep of 0.05s was specified for the momentum and turbulence terms and 0.01s for the volume fractions. Note that the CFX modeling guide [61] recommends setting the timestep of the volume fractions an order of magnitude smaller than the momentum equations for improved stability.

2.5.4 Computational Mesh

The mesh used 100 uniformly spaced nodes in the y direction ($\Delta_y = 0.02\text{m}$). In the x direction the spacing varied from 0.035m at the inlet to 0.005m at the actuator strip using an expansion ratio of 1.02. Downstream of the actuator strip the x spacing increased with an expansion ratio of 1.02 to 0.028m at $x = 10\text{m}$. Then it expanded (ratio of 1.02) to 0.052m by $x = 15\text{m}$. The x spacing was uniform at 0.052m until $x = 20\text{m}$. The dissipation zone boundary condition then began. In this region the x spacing expanded with a ratio of 1.3 to a final x spacing of 15.9m at $x = 100\text{m}$. As mentioned earlier this dissipation zone is used to improve the simulation stability. The 2D surface mesh was extruded in the z direction 0.2m using a single element. This was done because the CFX solver requires a 3D mesh, even for a 2D simulation.

²CFX uses the first order backward Euler transient scheme for steady simulations.

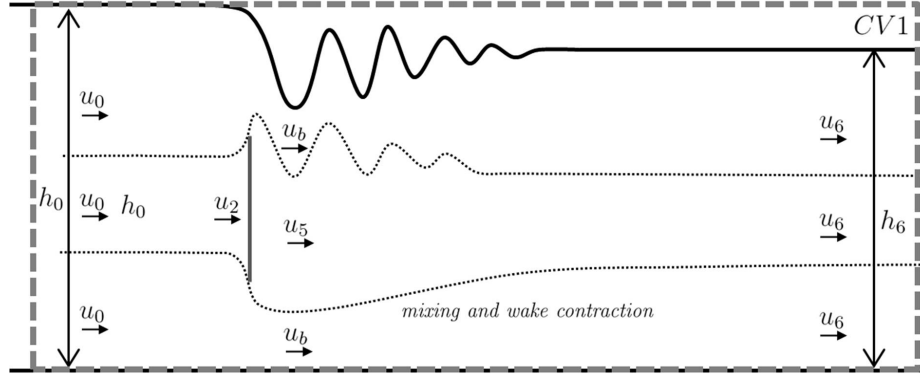


Figure 2.17: Depiction of the wake and free surface deformation which occur when turbines operate near the water surface.

2.5.5 A New Analytical Treatment for Free Surface Effects

In their free surface effect derivation Whelan *et al.* [2] used Bernoulli's equation to determine the surface elevation change in terms of the pressure change from upstream to downstream of the turbine. This treatment did not consider the fact that the fast bypass flow must mix with the slower wake. As this mixing process takes place, the free surface height rises to some value above that assumed by Whelan *et al.* This behavior was observed in CFD simulation results presented in section 3.5, and a new treatment for the free surface height has been derived which agrees more closely with the CFD simulations. First, expressions for the influence of the turbine thrust on the free surface are defined, then the impact of the free surface deformation on the rotor velocity is considered in determining the power.

Influence of Turbine Thrust on the Free Surface

Consider a control volume which extends from upstream of the turbine to the very-far-wake, which is defined as the location where the wake has fully mixed and the velocity is uniform as depicted in Figure 2.17. Consistent with the CFD simulation approach, it is assumed that the known parameters are the upstream flow velocity u_0 , the downstream free-surface height h_6 and the turbine thrust force T . Applying continuity gives:

$$u_0 h_0 = u_6 h_6 \quad (2.5.2)$$

Applying the 1D linear momentum equation:

$$\sum F_x = \dot{m}(u_6 - u_0) \quad (2.5.3)$$

$$\int_0^{h_0} (p_a + \rho g z t) - T - \int_0^{h_6} (p_a + \rho g z t) - p_a t (h_0 - h_6) = \rho h_0 t u_0 (u_6 - u_0) \quad (2.5.4)$$

$$\frac{1}{2} \rho g h_0^2 t - T - \frac{1}{2} \rho g h_6^2 = \rho h_0 t u_0 (u_6 - u_0) \quad (2.5.5)$$

Substituting for u_6 using the continuity equation and dividing the whole equation by $\frac{1}{2}\rho t$ gives:

$$gh_0^2 - \frac{2T}{\rho t} - gh_6^2 = \frac{2h_0^2u_0^2}{h_6} - 2h_0u_0^2 \quad (2.5.6)$$

Collecting like powers for h_0 , and using the definition of thrust coefficient $T = \frac{1}{2}\rho u_0^2 C_T h_t t$ gives a simple quadratic to solve for the unknown upstream surface height.

$$0 = \left[g - \frac{2u_0^2}{h_6} \right] h_0^2 + [2u_0^2]h_0 + [gh_6^2 + C_T u_0^2 h_t] \quad (2.5.7)$$

This equation is non-dimensionalized by defining the Froude number with reference to the upstream velocity and the very-far wake water depth, i.e. $F_r = \frac{u_0}{\sqrt{gh_6}}$. The turbine blockage ratio is also defined using h_6 (i.e. $B_r = \frac{h_t}{h_6}$). Then, dividing the above equation by gh_6^2 gives:

$$0 = [1 - 2F_r^2] \left(\frac{h_0}{h_6} \right)^2 + 2F_r^2 \frac{h_0}{h_6} - [1 + C_T F_r^2 B_r] \quad (2.5.8)$$

The solution of which is given in dimensional and non-dimensional forms:

$$h_0 = \frac{u_0^2 - \sqrt{u_0^4 + \left(g - \frac{2u_0^2}{h_6} \right) (gh_6^2 + C_T u_0^2 h_t)}}{\frac{2u_0^2}{h_6} - g} \quad (2.5.9)$$

$$\frac{h_0}{h_6} = \frac{F_r^2 - \sqrt{F_r^4 + (1 - 2F_r^2)(1 + C_T F_r^2 B_r)}}{2F_r^2 - 1} \quad (2.5.10)$$

This root gives realistic solutions when both the upstream and downstream flows are sub-critical. The second root (not shown) gives realistic solutions when the flow is super-critical both upstream and downstream. Note that when the flow undergoes a transition between super-critical and sub-critical regimes, there is also a transition between which roots should be used. Clearly non-physical solutions give a negative value for the upstream water height, and can be discarded.

An alternative set of boundary conditions assumes that the upstream height and velocity are known. The goal is then to solve for the unknown downstream surface height and velocity. With this set of boundary conditions, the Froude number and blockage ratio are defined as $F_r = \frac{u_0}{\sqrt{gh_0}}$, $B_r = \frac{h_t}{h_0}$. Note that these definitions are different than those used in the above case where u_0 and h_6 are known. Using these definitions, the following cubic expression is obtained:

$$0 = \left(\frac{h_6}{h_0} \right)^3 + \frac{h_6}{h_0} [(C_T B_r - 2)F_r^2 - 1] + 2F_r^2 \quad (2.5.11)$$

This expression can be defined as a monic trinomial of the general form;

$$t^3 + pt + q = 0 \quad (2.5.12)$$

where

$$p = [(C_T B_r - 2)F_r^2 - 1] \quad q = 2F_r^2 \quad (2.5.13)$$

The number of real roots for this equation depends on the value of the determinant $\Delta = -4p^3 - 27q^2$.

When $\Delta > 0$ there are three real roots, which can be found using the following general trigonometric solution:

$$\left(\frac{h_6}{h_0}\right)_k = 2\sqrt{-\frac{p}{3}} \cos \left\{ \frac{1}{3} \arccos \left[\frac{3q}{2p} \sqrt{\frac{-3}{p}} \right] - k \frac{2\pi}{3} \right\} \text{ for } k = \{0, 1, 2\} \quad (2.5.14)$$

The solution for $k = 0$ corresponds to sub-critical downstream flow regardless of the state of the upstream flow, while the solution for $k = 1$ corresponds to super-critical downstream flow. The solution for $k = 2$ gives a negative value for the downstream free surface height and can be discarded.

When $\Delta < 0$ there is only one real root, which can be found using Cardano's method as:

$$\frac{h_6}{h_0} = \sqrt[3]{-\frac{q}{2} + \sqrt{\frac{q^2}{4} + \frac{p^3}{27}}} + \sqrt[3]{-\frac{q}{2} - \sqrt{\frac{q^2}{4} + \frac{p^3}{27}}} \quad (2.5.15)$$

However, this root always gives a negative downstream free surface height and is discarded. Thus, when $\Delta < 0$ there is no realistic solution to the equation. This condition arises when the thrust becomes too large for the upstream froude number. A special condition arises when the upstream flow is critical (i.e. $F_r = 1$) which only gives a realistic solution when the rotor thrust is zero. With critical upstream flow, any positive thrust gives the condition $\Delta < 0$ and the equation cannot provide a realistic solution.

Influence of Free Surface Deformation on Power

Given this new formulation for the eventual free surface deformation, a simple method for determining the impact of this deformation has been established simply considering the reduction in cross sectional area caused by the change in free surface height. First the well established blockage effect correction for $F_r = 0$ is applied. This correction has been defined by several authors including Sørensen *et al.* [73], Garrett and Cummins [26] and Whelan *et al.* [2] who give in the form:

$$\tau_B = \frac{1 - \alpha_B + \sqrt{B_r - 2\alpha_B B_r + \alpha_B^2(1 - B_r + B_r^2)}}{1 - B_r} \quad (2.5.16)$$

where $\tau_B = u_b/u_0$, $\alpha_B = u_5/u_0$ and $B_r = A_f/A_c$ is the blockage ratio. The thrust coefficient is defined as:

$$C_T = \tau_B^2 - \alpha_B^2 \quad (2.5.17)$$

The velocity at the turbine can then be defined as $u_2 = \beta_B u_0$ where β_B is found using;

$$\beta_B = \frac{\alpha_B(\tau_B - 1)}{B_r(\tau_B - \alpha_B)} \quad (2.5.18)$$

At this point, the correction for the change in the channel cross sectional area at the rotor plane is included in the analysis. This is done by multiplying the velocity ratio at the rotor plane (β_B) by a factor of $\frac{1}{2} \frac{h_0 - h_6}{h_0}$. The change in water height is found using either equation 2.5.10 or equation 2.5.14, depending on which set of boundary conditions are known.

$$\beta_{fs} = \frac{\alpha_B(\tau_B - 1)}{B_r(\tau_B - \alpha_B)} \frac{1}{2} \frac{h_0 - h_6}{h_0} \quad (2.5.19)$$

This accounts for the increased velocity at the rotor due to the reduction in channel cross sectional area which arises from the change in free surface height. The factor $\frac{1}{2}$ is from assuming that the free surface height at the rotor plane is the average of the upstream and eventual downstream heights. Despite the crudeness of this assumption, the predicted power increase matches the CFD simulation results remarkably well, as shown in section 3.5. The power coefficient is then:

$$C_P = \beta_{fs}(\tau_B^2 - \alpha_B^2) \quad (2.5.20)$$

A comparison of the two analytical models for free surface effects is made to the results of CFD simulations in section 3.5. It was found that the new analytical treatment matched the simulations very well, while the treatment by Whelan *et al.* overpredicted the influence on turbine power. Section 3.5 also evaluated the importance of modeling free surface effects for realistic tidal flows and found that the influence of the free surface on the turbine power was small relative to the influence of blockage effects. Additionally, CFD modeling of free surface effects adds considerable complexity and computational expense compared to just modeling blockage effects, especially when fully 3D or circular disks are to be considered. Thus the method for optimizing turbines in a realistic tidal channel described in the next section did not account for free surface effects.

2.6 Method for Turbine Optimization in a Idealized Tidal Channel

This section describes a methodology to incorporate a model of real-world channel dynamics with actuator disk CFD simulations that account for blockage effects. The methodology makes use of the actuator disk CFD methods described in section 2.4, but modifies the domain to include the effects of channel blockage. The method also makes use of an analytical channel dynamics model, developed in the field of tidal resource assessment which uses realistic tidal forcing, and includes friction terms to account for the channel bottom friction and the effect of turbines on reducing the flow through the channel. This combination of models allows the total power generated by a tidal fence of equally spaced turbines to be calculated. It also provides the associated reduction in tidal amplitude. Within this combined model framework, the CFD-based optimization algorithm can be used to determine the optimal combination of C_T , C_{nu} and λ for turbines occupying a given portion of the channel cross sectional area. The optimization algorithm was also altered to include a constraint on the acceptable change in tidal amplitude, which is a realistic constraint which could be set to mitigate the changes to the local ecology. The developed methodology could be applied to any real-world tidal channel.

2.6.1 Background

Tidal turbines have traditionally been designed considering an infinite domain using design tools from the wind industry based on actuator disk and blade element theory. However in practice, turbines will be placed in tidal channels which restrict the flow within lateral boundaries as well as within bottom and free surface boundaries. The impact of this is to restrict the expansion of the flow approaching the turbine, forcing more mass through the rotor than in the unbounded case. In the extreme limit, where the entire channel cross section is occupied by turbines, all of the upstream mass flow must pass through the rotors. In this limit the power extraction manifests itself as a head loss, and it is possible to operate the turbines in a manner quite similar to a tidal barrage, except that power is continuously extracted while the flow passes through the turbines, instead of being held back over most of the tidal cycle, and released over a short period of time. It is desirable to take an incremental development strategy, where turbines would be added to the fence over a period of many years. This would avoid the excessive capital costs associated with barrage type-schemes, and allow a more gradual change to the local ecology, which could be monitored as the project progresses.

Tidal power resource assessment must account for the reduction of velocity in a given tidal channel which arises due to the forces exerted on the flow by turbines. This is commonly done using regional scale oceanographic models where turbines are treated as a quadratic drag term applied to computational elements in the simulation [6, 21, 23, 75–77]. Analytical treatments have also been developed for simplified 1D channels, which assume that turbines occupy the entire cross sectional area of the channel [6, 24, 78, 79]. To deal with partial tidal fences, analytical treatments [25, 26] can also be applied, but typically assume ideal turbines and neglect viscous effects between the turbine wake, and faster moving bypass flow. Most resource assessment studies assume ideal turbine

performance, neglecting the effects of structural drag, blade drag, wake swirl and blade tip loss. To obtain more realistic resource estimates, these effects should be considered. Likewise, turbine design is typically carried out assuming no blockage from bathymetry, the free surface, or other turbines, thereby ignoring these important effects.

In the method described in this section, numerical simulations are used to account for the effect of channel boundaries restricting the wake expansion (called blockage effects), while a simple analytical 1D channel model is used to represent the gross effect of turbines reducing the flow through the channel and to determine the associated change in tidal amplitude. This allows a numerical determination of the optimal turbine blade geometry and tip speed ratio for a range of blockage ratios (defined as the frontal area of turbines in the fence divided by the channel cross sectional area $B_r = A_f/A_c$) to maximize power production with an arbitrary constraint on the acceptable change in the tidal amplitude. The results give a prediction of the power which can be produced in a given tidal channel with realistic (i.e. non-ideal) turbines, and demonstrates the increased per-turbine power production which can be achieved if turbines are tuned to maximize power production in a tidal fence.

2.6.2 Literature Review

The fundamental limits to tidal power generation using turbines in a fence configuration have been studied by Garrett and Cummins in a series of papers. In [78] they defined a one-dimensional model of a channel with variable cross sectional area linking a bay to the ocean in which the flow is driven through the channel by the difference in the free surface height between the open ocean and the bay. Using an analytical treatment, they noted that power is extracted most efficiently when turbines are arranged in a fence spanning the entire channel cross section, and this arrangement was assumed for the model derivation. Their analysis neglected flow acceleration terms in the basic dynamical balance but did account for the impact of increased drag in the channel due to turbines on the flow velocity. The increased drag reduces the velocity through the channel, and changes the rate at which the water rises in the bay. The power generated by the turbines is proportional to the force they apply to the flow (i.e. the increased drag) and the mass flow rate through them and is maximized by tuning a turbine drag parameter. In [80] they created a similar 1D model for the case of a channel linking two large bodies of water where the surface elevation of both was not dependent on the flow through the channel. Later, Blanchfield *et al.* [79] defined a 1D treatment which included flow acceleration terms and exit separation effects in the dynamical balance, and could be applied to scenarios of a channel linking a small bay to the ocean, or a channel linking two independent large bodies of water, but could only be solved numerically unless some limiting assumptions are made. This model also assumed a tidal fence spanning the entire channel cross section. Karsten *et al.* [6] derived an approximate analytical solution to the model of [79] which gave very similar results to numerical solutions and to basin-scale simulations for Minas Passage. Due to the simplicity and demonstrated accuracy of this latter treatment, it has been used in this thesis work.

In reality, tidal turbines are unlikely to occupy an entire channel cross section due to a number of limitations discussed later in this section. To address the effect of using turbines which occupy a fraction of the channel cross section, defined as the blockage ratio $B_r = A_f/A_c$ (where A_f is

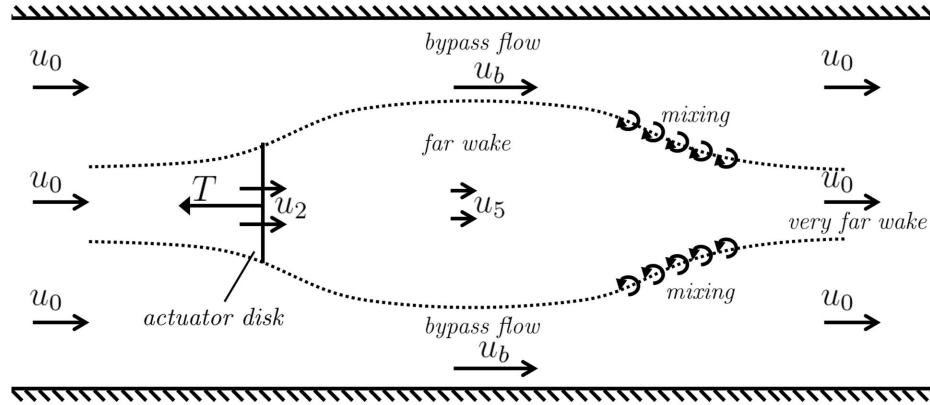


Figure 2.18: Flow parameters used in defining an analytical treatment for channel blockage effects

the frontal area occupied by the fence of turbines and A_c is the channel cross sectional area), Garrett and Cummins [26] applied an analytical treatment for blockage effects which, incidentally, is mathematically identical to wind tunnel blockage corrections (presented in [73] for example.) A depiction of the flow used in this analytical model is given in figure 2.18. Note that the flow which does not pass through the turbine (the bypass flow) is accelerated and reaches a peak velocity where the wake is fully expanded. This model assumed a constant uniform velocity into the channel, a boundary condition which is not consistent with the 1D models discussed in the previous paragraph. Garrett and Cummins acknowledged this inconsistency in [24], but argued that the blockage effect model may be combined with the 1D channel model if the channel is assumed to have constant cross sectional area from the location of the turbine fence to the downstream location where the turbine wakes are fully mixed with the bypass flow, resulting in uniform flow. Vennell [25] combined the analytical treatment for partial fences from [26] with the channel flow model from [80] to create a method to determine the optimal turbine drag parameter for full fence and partial fence scenarios.³ Vennell noted that the partial channel treatment assumed steady flow and neglected bottom friction, while the channel flow model does include bottom friction. He rationalized combining the models by assuming that the turbines occupy a short section of the channel length and that within this length the turbine friction dominates bottom friction and flow inertia. Vennell demonstrated that using the combined model, the optimal turbine drag parameter differed than that found using the analytical channel model alone. He showed that the turbine drag which optimizes power generation must change with increasing blockage ratio. This has important implications for both resource assessment and turbine design.

The approach of Vennell is taken in the present study; but here the analytical channel treatment of [6] is used for the overall dynamical balance of the driving tidal forcing with bottom drag, channel drag and exit separation, and CFD simulations are used to evaluate the impact of using partial turbine fences. The rationale for using a more detailed and complex analysis (i.e. CFD) for partial fence effects (also referred to as blockage effects) is to allow comparing ducted/non-ducted turbine

³Vennell actually used the ratio of the wake velocity to the freestream velocity as a tuning parameter, but this is equivalent to tuning the turbine drag parameter

concepts, and to allow determination of the turbine blade geometry to maximize power output. The CFD model approach also allows blade drag and wake swirl effects to be included in the analysis, and has been extended to include tip-loss and structural drag effects. These phenomena are neglected in the analytical treatments of blockage effects, which inherently assume ideal turbines.

The remaining contents of this section are organized as follows. First an overview of the methodology is given. This is followed by descriptions of the analytical channel flow model, the CFD simulations, the treatment of tip-loss effects and the combined model optimization. The application of the model and results are given later in section 3.6.

2.6.3 Methodology Overview

This study used the rotor optimization technique base on actuator disk CFD simulations described in section 2.4.9. This design tool was originally developed for unbounded flows, but was easily adapted for blocked flows by altering the boundary conditions. A simplified analytical channel flow model was used to calculate the response of the tidal flow to power extraction by turbines in terms of a reduction of the flow velocity and changes to the tidal amplitude in the bay. This model was taken directly from [6] and had been tuned for the specific flow behaviour of the Minas Passage. The combined model can determine the optimal turbine design to maximize the power generated by turbines while placing arbitrary constraints on the change to tidal amplitude. It is pertinent to include such a constraint to limit changes to the flushing rate of the bay, which is important for avoiding accumulation of pollution/silt and for mitigating changes to the bay ecology.

2.6.4 The Analytical Channel Model

The channel model is described in detail in [6] and is presented briefly here. The model assumes a channel with variable cross sectional area $A_c(x)$ over channel section position x and uniform axial flow at velocity $u(x)$, connected to a basin of surface area A_b . The flow is driven by the water height difference between the ocean and basin ($\zeta_0 - \zeta_b$). There is a balance of forces (due to the hydrostatic pressure gradient, bottom drag and turbine drag) and the acceleration of the flow. The governing equations for the flow are:

$$c_g \frac{dQ}{dt} + \gamma |Q|Q = g(\zeta_0 - \zeta_b) \quad (2.6.1)$$

$$Q = A_b \frac{d\zeta_b}{dt} \quad (2.6.2)$$

The water height on the ocean side of the channel is assumed to be a single sinusoid given by;

$$\zeta_0 = a_t \cos \omega_t t \quad (2.6.3)$$

where a_t and ω_t are the amplitude and frequency of the dominant tidal constituent. It should be noted here that the inclusion of additional tidal constituents can produce significant increases to the calculated power extraction [81], however it is argued that since the M2 tidal forcing dominates in Minas Passage [82] the other constituents can be reasonably neglected. For the sake of simplicity,

and to allow comparison to the results of [6] a single constituent (the M2 forcing with $a_t = 4.71m$ and $\omega_t = 1.4 \times 10^4 s^{-1}$) was used in this study.

By assuming that the basin water height can also be represented as a single sinusoid;

$$\zeta_b = a_b \cos(\omega_t t - \phi_b) \quad (2.6.4)$$

where a_b and ϕ_b are the unknown amplitude and phase lag of the basin tides, it is possible to define an approximate solution to the governing equations following the strategy of [6]. The solution is given in terms of an amplitude ratio $R_a = a_b/a_t$ and phase lag ϕ_b and is given by:

$$R_a^2 = \frac{2\beta_g^2}{(\beta_g - 1)^2 + \sqrt{(\beta_g - 1)^4 + 4\gamma^{*2}}} \quad (2.6.5)$$

$$\phi_b = \arcsin\left(\frac{\gamma^*}{\beta_g^2} R_a^2\right) \quad (2.6.6)$$

Here, β_g is a non-dimensional parameter determined by the geometry of the channel and basin, defined by:

$$\begin{aligned} \beta_g &= \frac{g}{A_b} \omega_t^2 c_g \\ c_g &= \int_0^L \frac{dx}{A_c(x)} \end{aligned} \quad (2.6.7)$$

Instead of evaluating this integral over the channel, Karsten *et al.* [6] determined the value $\beta_g = 7.62$ through tuning of a numerical model to best match observed tidal ranges in the Bay of Fundy.

The non-dimensional drag parameter γ^* is defined as:

$$\gamma^* = \frac{8}{3\pi} \frac{g a_t}{(c_g \omega_t)^2} (\gamma_0 + \gamma_1) \quad (2.6.8)$$

where γ_0 is the drag parameter for the channel in its natural state and γ_1 is the drag parameter for the turbines. Note that as stated in [6], “*the non-linear drag (γ^*) represents not only the drag associated with bottom friction and the addition of turbines but also all other non-linearities in the model, including non-linear advection and the nonlinearities involved with the changes in domain as the tides rise and fall.*” As with β_g , γ_0^* (i.e. the non-dimensional channel drag parameter in its natural state) was determined through tuning of a numerical model to best fit observed tidal amplitudes and phase throughout the Bay of Fundy.

Using the model, it is possible to calculate the time-averaged power produced for turbines occupying the entire channel (a subscript $_{ff}$ is used to denote ‘full-fence’) is then given by:

$$P_{ff} = \frac{\gamma_1^*}{2R_{a0}\beta_g^2} R_a^3 \rho g a_t Q_0 \quad (2.6.9)$$

2.6.5 Achievable Blockage Ratio

It is important to note that equation 2.6.9 gives the power that could be produced by turbines if they occupied the entire tidal channel cross sectional area, and if all of the axial force force applied by the turbines contributed directly to power production. While useful in preliminary resource assessments,

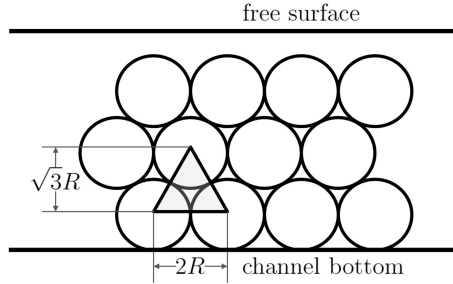


Figure 2.19: Image showing the maximum theoretical packing density for turbines in a single turbine fence.

this clearly overpredicts the amount of power that might reasonably be extracted by a real array of real turbines. For a single fence of turbines, the total swept area is very unlikely to reach the total channel area. An upper limit on the total turbine frontal area assuming staggered horizontal axis axial flow turbines can be defined by considering an arrangement of staggered circles as shown in figure 2.19. A unit cell of this type of arrangement is shown by the triangle. It is simple to define the maximum percentage of turbine area to channel area as:

$$B_r = \frac{A_f}{A_c} = \frac{\frac{1}{2}\pi R^2}{\frac{1}{2}2R\sqrt{3}R} = \frac{\pi}{2\sqrt{3}} \approx 90.7\% \quad (2.6.10)$$

In reality, turbines will not be so closely packed due to clearance requirements with an irregular bottom, a dynamic free surface and other turbines. On the other hand, support structures could be designed to help direct flow through the turbines, increasing the effective blockage ratio. This so called “tidal reef” style design could, in principle, direct all the flow through turbines by blocking the flow in non-swept regions. This seems to be a reasonable strategy which may warrant future investigation. However this would require special considerations to allow the passage of fish and other marine animals across the ‘reef’. In any event, a section of the channel would have to be left open for navigation, and a maximum feasible blockage ratio of 80% has been defined for this study. In practice, it is felt that a realistic feasible blockage ratio would likely be closer to 50%.

2.6.6 Accounting for Losses

When turbines do not occupy the entire channel cross section, there are power losses which arise due to the mixing of the turbine wake flow with the bypass flow. Analytical solutions by Garrett and Cummins [26] predict that for unbounded flows, the wake loss is 1/3 of the total power dissipation. This analysis agrees with the famous Betz limit. Their analytical model also predicts that wake loss accounts for 2/3 of the total power dissipation at very high blockage ratios, but this estimate is unrealistic because the solution neglects viscosity and turbulent mixing which do become important at high blockage because of the very strong shear layer that develops between the bypass flow and the wake. Other losses arise from the drag of support structures, ducts and the blades themselves. Due to this, a significant portion of the increased drag caused by turbines does not contribute towards power production. Previous studies such as [6] have not accounted for such losses and thus over-

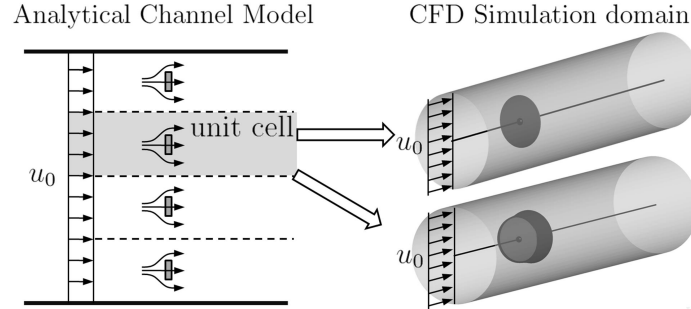


Figure 2.20: Schematic of a tidal fence with turbines spaced at regular intervals. The flowfield is divided into a series of identical unit cells, which can be modeled using CFD simulation. The two images at the right show flow domains for un-ducted and ducted turbines.

predict the reasonable power extraction. Additionally, some of the energy dissipated from the flow is converted into rotational kinetic energy in the swirling wake. Further still, non-ducted turbines are subject to tip loss, discussed further in section 2.6.8.

To account for all of these factors, turbines have been simulated with CFD using an axi-symmetric flow domain with a specified blockage ratio. The model assumes that the turbines are uniformly distributed along a single transect of the channel cross section. In doing so, it is possible to define a single unit cell containing one turbine as shown in figure 2.20. With this set of assumptions, such a unit cell is representative of every turbine in the channel. Note that blockage effects are primarily governed by area ratios, which justifies using an axi-symmetric domain in the CFD simulation to represent the rectilinear unit cell in the channel model. The impact of blockage effects on the turbine are resolved by the simulation, and the gross effect on the flow is calculated by assuming that all turbines in the channel apply the same force to the flow. This strategy is very similar to that used by Vennell [25] who showed that the ideal tuning of turbines depends strongly on the blockage ratio.

2.6.7 Turbine Simulations

The turbine simulations used the axi-symmetric actuator disk CFD method described in section 2.4. The flow domain was altered such that the outer radial boundary used a free-slip boundary condition, and was located to provide the desired blockage ratio. Recall that the simulations employ a fixed, uniform inlet velocity. These boundary conditions are the same as assumed by analytical models presented by [26] and [25]. The result of the simulation is to provide a ratio of the power produced by a single turbine P to the ideal full fence power P_{ff} defined by equation 2.6.9. The CFD simulation is of a single turbine, which is taken to be representative of every turbine in the tidal fence. Of, course this is only valid considering that the channel flow velocity is assumed to be uniform.

In the simulation, the turbine power is calculated as a volume integral of the product of driving torque (rS_θ) and the rotor speed Ω over the actuator disk region.

$$P = \int_{Vol} S_\theta r \Omega dVol \quad (2.6.11)$$

Recall that the term S_θ is formulated to include the effects of blade drag and wake rotation on the power produced. The power is normalized by the freestream kinetic power density and the rotor area A_r .

$$C_P = \frac{P}{\frac{1}{2}\rho u_0^3 A_r} \quad (2.6.12)$$

The ideal ‘full fence’ power produced by the individual turbine in the simulation (i.e. the ideal power that the single turbine would produce if it occupied the entire cross section of its unit cell) is determined as the product of the total axial force applied by the turbine (including duct and structural drag) and the inflow velocity u_0 . Note that in the scenario of a 100% blockage turbine, all of the flow must pass through the turbine, and ideally all of the power lost by the flow is converted to useful power. Thus, the ideal full fence power is equal to the total power lost by the flow. Corten [62] gives an excellent derivation showing that the total flow power loss is simply the product of the total axial force and freestream velocity. In this study, this is given by:

$$P_{ff} = 1.1(T + D)u_0 \quad (2.6.13)$$

where the rotor thrust T is found as a volume integral of the turbine axial force exerted by the actuator disk, and the duct drag D is found by evaluating pressure and skin friction integrals over the duct surface. The factor 1.1 is used to account for drag due to support structures, which is assumed to increase the total axial force by 10%. The value of 10% was determined based on drag estimates for the MCT Seagen turbine (described more fully in sec 3.1.4) which found a drag coefficient based on rotor swept area, $C_{D,A_r} = 0.085$. Without detailed modeling of the support structures, it is not possible to accurately evaluate the effect of structural drag, however it seems reasonable to assume that since structures must become heavier as total device loading increases, then the structural drag is proportional to the sum of rotor thrust and duct drag. For open flow turbines, the optimal rotor thrust coefficient is 8/9. Assuming that the MCT turbine is designed for this condition, the structural drag is approximately 10% of the rotor loading.

Normalizing the rotor thrust and duct drag by the rotor area and freestream kinetic energy density gives:

$$C_T = \frac{T}{\frac{1}{2}\rho u_0^2 A_r} \quad C_D = \frac{D}{\frac{1}{2}\rho u_0^2 A_r} \quad (2.6.14)$$

which allows the ratio of turbine power to full fence power to be defined by:

$$\frac{P}{P_{ff}} = \frac{C_P}{1.1(C_T + C_D)}. \quad (2.6.15)$$

The drag parameter γ_1 used by the channel model is defined as the total axial force of all turbines operating in the channel, normalized by the density, freestream velocity squared and channel cross sectional area.

$$\gamma_1 = \frac{\frac{1}{2}\rho u_0^2 1.1(C_T + C_D)A_r N_{turb}}{\rho u_0^2 A_c^3} \quad (2.6.16)$$

$$= \frac{1.1(C_T + C_D)B_r \frac{A_r}{A_{de}}}{2A_c^2} \quad (2.6.17)$$

where the blockage ratio B_r is defined based on the total frontal area occupied by turbines $A_f = N_{turb}A_{de}$, where A_{de} is the duct exit area for a ducted turbine, and is equal to the rotor area A_r in the case of a non-ducted turbine.

Combining equations 2.6.8, 2.6.9, 2.6.15 and 2.6.17 the time-averaged power production of turbines in a channel is given by;

$$P = \frac{2}{3\pi} C_P B_r \frac{A_r}{A_{de}} \frac{ga_t}{(A_c c_g \omega_t)^2} \frac{R_a^3}{R_{a0} \beta_g^2} \rho g a_t Q_0 \quad (2.6.18)$$

where R_a is found using equation 2.6.5. This method allows the calculation of the total power output of an array of turbines of equal spacing in a channel with known characteristics. At the device scale, all that is required is to measure or simulate the total power production and axial force acting on the turbine installation. In this study, these parameters have been determined through CFD simulation of reasonable turbine designs. It would be equally convenient to apply experimental data from prototype testing to this analysis, which would provide an even more realistic estimate of extractable power.

2.6.8 Tip Loss

It is important to note that for the ducted concept, no tip loss model was applied. This is consistent with the findings of Fleming *et al.* [16] who used CFD simulation to demonstrate that the presence of the duct prevents tip vortices. For non-ducted turbines on the other hand, tip loss effects are well documented and most commonly accounted for using the Prandtl tip loss correction, which is almost universally applied in BEM codes, but has also been used in actuator disk CFD methods [60].

The validity of the Prandtl tip loss model is questionable for flows involving channel blockage because it assumes that the flow bypassing the wake has velocity is equal to the freestream. This assumption becomes increasingly poor as the channel blockage ratio increases due to an accelerated bypass flow. The impact of tip vortices on the flowfield is still expected to be somewhat important, and as a first order approximation, it has been assumed that the reduction in power due to tip loss is constant with blockage ratio. The impact of channel blockage on tip loss effects could be studied using an actuator line CFD [40] approach, however due to the computational expense and time constraints, such work was not carried out during this thesis.

In the present work, the estimated reduction in thrust and power due to tip loss was evaluated using a non-linear optimization of the standard blade element momentum (BEM) [54] equations. This was described in section 2.2.6. It was found that including tip loss in the optimization resulted in a 5.34% reduction in C_P and a 2.73% reduction in C_T compared to running the same optimization neglecting tip loss.

The actuator disk CFD simulations for non-ducted turbines used in the channel model do not account for tip loss, and therefore the output power and operating thrust coefficient should be reduced by these factors to obtain an estimate of the actual power and basin response to real turbines which are subject to tip losses. These reductions were accounted-for in the channel model simulations by modifying the calculation of the non-dimensional turbine drag parameter γ_1 in equation 2.6.17

and turbine power P shown in equation 2.6.18 as follows:

$$\gamma_1 = 0.9727 \frac{1.1(C_T + C_D)B_r \frac{A_r}{A_{de}}}{2A_c^2} \quad (2.6.19)$$

$$P = 0.9466 \frac{2}{3\pi} C_P B_r \frac{A_r}{A_{de}} \frac{ga_t}{(A_c c_g \omega_t)^2} \frac{R_a^3}{R_{a0} \beta_g^2} \rho ga_t Q_0 \quad (2.6.20)$$

The same reduction factors were applied to all of the considered blockage ratios. In reality, there is likely some change in the power and thrust reduction for optimized rotors due to tip loss at different blockage ratios. However a valid treatment for the interaction of tip-loss and blockage effects has not yet been established. Thus, a constant reduction is the best estimate available. These reductions are not very large and neglecting tip loss altogether would not have an impact on the conclusions of this study, but tip loss will be important for detailed blade design.

2.6.9 Optimization of the Turbine Blades and Tip Speed Ratio

The optimization algorithm described in section 2.4.9 was modified with a new objective function and to allow the specification of a constraint on the change in tidal amplitude in Minas Basin. For this study, the objective function was the time averaged power produced by the turbines, which was calculated using equation 2.6.18 for the ducted concept and equation 2.6.20 for the non-ducted concept. The limit to the acceptable change to the tidal amplitude in Minas Basin was defined as:

$$\Delta_{R_a} = \frac{R_{a0} - R_a}{R_a} \quad (2.6.21)$$

The optimization search space consisted of the thrust coefficient C_T , tip speed ratio λ (the ratio of the blade tip speed to the freestream velocity) and non-uniform loading coefficient C_{nu} which defines the slope of a linear variation in the rotor loading with radius. The method assumes that these parameters are held constant over the tidal cycle, which is reasonable since they are non-dimensional operating parameters for a constant blockage ratio. Since C_T and λ are non-dimensionalized by the freestream velocity, the actual rotor thrust and rotor speed would change sinusoidally in phase with the velocity of the flow through the channel. Note that due to assuming that power is generated over the entire tidal cycle, the cut-in speed of the turbines is neglected in the current analysis. The algorithm sought out the maximum objective within a discretized grid of the design search space. A higher density grid for the search space provides more precision in finding the optimum design point, but increases the required number of CFD simulations. The grid spacings were $\Delta_{C_T} = 0.05$, $\Delta_\lambda = 0.1$, and $\Delta_{C_{nu}} = 0.1$. It was found that near the optimum operating point, the turbine power production was acceptably insensitive to changes in the control parameters corresponding to one grid space, which confirmed that the grid was of adequate resolution.

Chapter 3

Application of the Models: Results and Discussion

This chapter describes the studies that have been conducted using the methods described in chapter 2. The sections are organized as follows:

- Section 3.1 describes a study that determined the performance and power extraction efficiency of ducted turbines (ducts D1 to D7) with ideal rotors.
- Section 3.2 describes the development of curve-fits of CFD results for the diffuser efficiency and base pressure coefficient for a range of ducts, which are employed by the 1D duct performance model described in section 2.3.2.
- Section 3.3 gives sample results of the rotor optimization technique using actuator disk CFD simulations described in section 2.4.9.
- In section 3.4 the DuctBEM model (section 2.3) was used to analyze the rotor developed in section 3.3 and the resulting performance was compared to that predicted by the CFD simulations. The DuctBEM model was also used to optimize the rotor and the resulting blade geometry was compared to that found from the CFD-based optimization.
- Section 3.5 shows results of the CFD simulations of free surface effects and compares these to the analytical model by [2] and the newly developed analytical model from section 2.5.5.
- Finally, Section 3.6 presents the results of applying the methodology for optimizing turbines in a real-world channel described in section 2.6 to a case study of Minas Passage in the Bay of Fundy.

3.1 Performance of Ducted Turbines with Ideal Rotors

Near the beginning of this thesis work, a study was undertaken to evaluate the power enhancement of ducted turbines and to compare their performance to open flow turbines. In addition to observing the power coefficient, an additional performance metric called the extraction efficiency was determined.

Highly idealized models were used for both turbine concepts. The well-established BEM method (section 2.2) was used for evaluating the non-ducted turbine, while the actuator disk CFD method (section 2.4) was applied to the ducted turbines. For both concepts, ideal rotor performance was assumed, and therefore only the axial forces and momentum were considered (neglecting losses due to blade drag, wake rotation and tip loss). Furthermore, this initial study only looked at the case of an isolated turbine in an unbounded domain. The definition of extraction efficiency given in this section was formulated to give a term relating the power production of tidal turbines to their impact on the tidal flow. This was done to provide a useful metric for comparing turbine concepts given a finite tidal resource.

3.1.1 Defining Extraction Efficiency

At the time of the study, no previous work had been found that defined an efficiency term as formulated in this study. The extraction efficiency was defined as the power produced by the turbine P divided by the total power lost from the flow P_{lost} .

$$\eta_{ex} = \frac{P}{P_{lost}} \quad (3.1.1)$$

First a highly simplified version of the power and power lost are given to provide some insight into the fundamental principles which govern this efficiency term. Considering an actuator disk with a uniformly distributed thrust loading, and assuming that the flow is uniform, the turbine power P is simply the product of the local flow velocity u_2 and the turbine thrust T .

$$P = Tu_2 \quad (3.1.2)$$

The power lost from the flow, which is equivalent to the total work done on the flow by all parts of the turbine system, is simply the sum of the turbine thrust T and device drag D (from the duct and structures) multiplied by the freestream velocity u_0 .

$$P_{lost} = (T + D)u_0 \quad (3.1.3)$$

This simple definition of power loss has been noted by Corten [62] and can be deduced by considering a system where the turbine with all its structures is pulled through a stationary fluid at a velocity u_0 . The power required to pull the turbine is simply the force applied multiplied by the velocity, and is equal to the power lost from the flow in the case of a stationary turbine in a moving fluid. The energy lost from the flow not owing to the useful power extraction in the rotor ends up as thermal energy after viscous dissipation completes, however the heat capacity of the flow is so large that the results are unaffected by considering this temperature change.

By defining the axial induction factor such that $u_2 = u_0(1 - a)$ and a drag factor $\gamma_d = \frac{D}{T}$ the efficiency can be expressed simply as:

$$\eta_{ex} = \frac{(1 - a)}{(1 + \gamma_d)} \quad (3.1.4)$$

Ducts are designed to increase the velocity at the rotor plane, thus increasing $(1 - a)$. They also produce increased drag, increasing γ_d . The definition of η_{ex} shows that the overall efficiency

of a ducted turbine could be greater than that of a conventional turbine if the increase to $(1 - a)$ outweighs the increase to the total axial force applied by the turbine on the flow $(1 + \gamma_d)$. The power and thrust terms are often normalized by the freestream kinetic energy density and rotor swept area A_r . In this section the duct drag is normalized in the same manner. The normalized parameters C_T , C_D , C_P and $C_{P_{lost}}$ are defined as;

$$C_T = \frac{T}{\frac{1}{2}\rho u_0^2 A_r} \quad (3.1.5)$$

$$C_D = \frac{D}{\frac{1}{2}\rho u_0^2 A_r} \quad (3.1.6)$$

$$C_P = \frac{P}{\frac{1}{2}\rho u_0^3 A_r} \quad (3.1.7)$$

$$C_{P_{lost}} = \frac{P_{lost}}{\frac{1}{2}\rho u_0^3 A_r} = C_T + C_D \quad (3.1.8)$$

Non-Ducted Turbines

For conventional turbines, the turbine efficiency was calculated based on standard 1D actuator disk theory [54]. The rotor velocity u_2 was assumed uniform over the actuator disk and is defined as $u_2 = u_0(1 - a)$ where a is the axial induction factor. By momentum theory, the induction factor is related to the thrust coefficient by.

$$a = \frac{1}{2} \left(1 - \sqrt{1 - C_T} \right) \quad (3.1.9)$$

At high thrust coefficients ($C_T > 8/9$) the momentum theory breaks down due to the turbine entering the turbulent wake state where momentum from the exterior flow is entrained into the wake. In this state, the induction factor is calculated by an empirical formula which fits a straight line from the value of C_T at the transition to turbulent wake state to a value C_{T1} when the induction factor $a = 1$. A value of 1.7 was taken for C_{T1} and the induction factor in the turbulent wake state was found using:

$$a = 1 - \frac{C_T - C_{T1}}{4\sqrt{C_{T1} - 1}} \quad (3.1.10)$$

Ducted Turbines

For ducted turbines, there is no simple theory defining the increase in power output and drag due to the presence of the duct. Thus, the efficiency was calculated based on results from simulations using the actuator disk CFD method described in Section 2.4. To represent ideal turbine rotors, only axial flow and axial force were considered in the simulations. The simulations applied an axial momentum source S_x to the actuator disk region. The thrust T was found as the volume integral of S_x over the actuator disk. The duct drag D was found as the surface integral of the local force in the axial direction (with pressure and shear components) over the duct. The turbine power P was found as the volume integral of the product of S_x and the local axial velocity u_2 , which varies radially and across the small but finite thickness of the disk (the disk thickness was less than 5% of

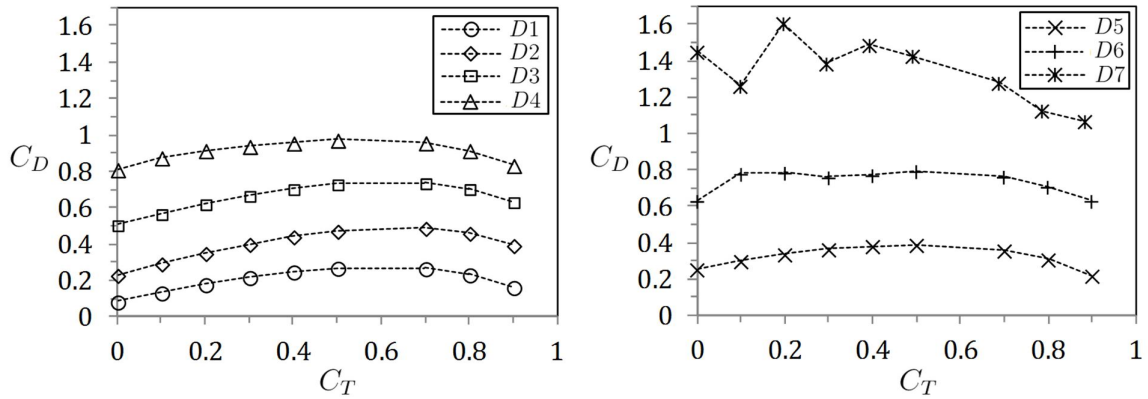


Figure 3.1: Variation of duct drag coefficient with thrust coefficient for ducts D1 to D7

its radius). The power lost from the flow and extraction efficiency were then found using equations 3.1.3 and 3.1.1.

3.1.2 Results For Turbines with Equal Rotor Area

The duct drag coefficient, turbine power coefficient and extraction efficiency were calculated for the ideal non-ducted turbine, and for ducts D1 to D7 described in section 2.1. These results are plotted in figures 3.1, 3.2 and 3.3. It can be seen that for turbines with equal rotor area, the ducted designs show a significant improvement in power over the non-ducted turbine, but at a cost of reduced efficiency. Based on these results, it appears that the efficiency of ducted turbines is bounded by the ideal open turbine case. This seems reasonable since the ideal open case assumes zero losses due to drag, and therefore represents a maximum possible efficiency. It is very important to note that this does not necessarily mean that non-ducted turbines are inherently more efficient than ducted turbines. The efficiency of particular turbines depends on their specific design and operation. Also, ducts suppress tip loss, which reduces the optimal non-ducted power output by approximately 5% causing a similar decrease in extraction efficiency.

Observing figures 3.1 through 3.3, several general trends are apparent. Ducts D1 through D4 were designed with increasing expansion ratios ($\frac{A_4}{A_3}$). The maximum C_P increased with the expansion ratio up to approximately $\frac{A_4}{A_3}=2.4$ (D3). Beyond this, no further improvement to C_P was noted. Ducts D5 to D7 were designed with increasing duct outlet angle (the expansion ratio also increased). The power coefficient increased as the outlet angle increased, but with diminishing returns. In general, as the influence of the duct on the flow increased (whether through increasing expansion ratio, or increasing outlet angle) the overall efficiency became lower. This is physically reasonable; considering that the power enhancement can be attributed to increasing circulation due to the duct lift force. Airfoils have a certain angle-of-attack that maximizes the lift-to drag ratio. When this angle is exceeded, the drag increases more rapidly than the lift. In an analogous manner, it should be expected that for a given duct profile, there is a combination of expansion ratio and outlet angle that provides the best compromise between increased circulation and increased drag.

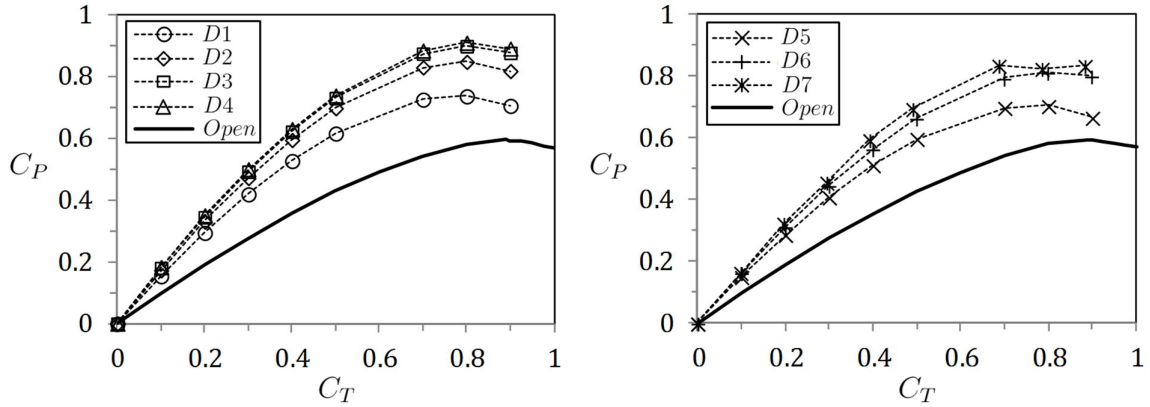


Figure 3.2: Variation of power coefficient with thrust coefficient for ducts D1 to D7 and for the ideal non-ducted turbine

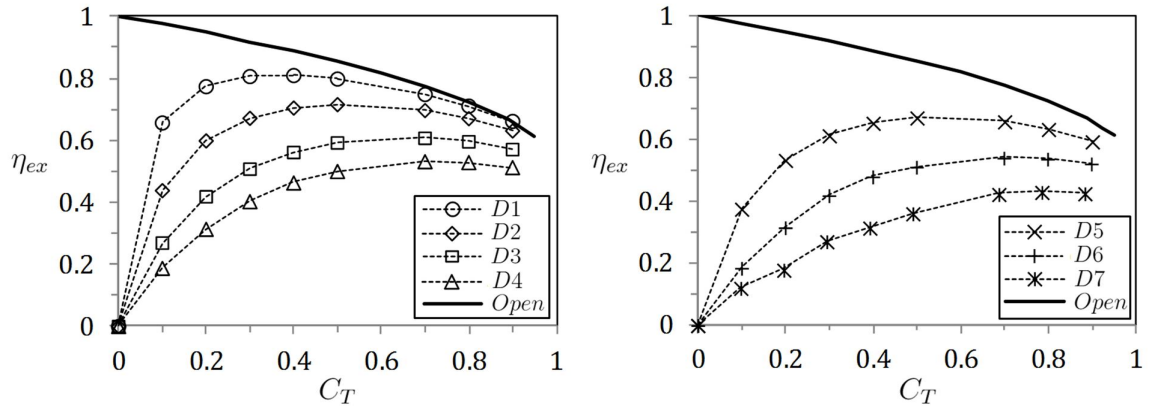


Figure 3.3: Variation of extraction efficiency with thrust coefficient for ducts D1 to D7 and for the ideal non-ducted turbine

The general trend was for decreasing efficiency with increased C_P enhancement, however the duct with the greatest C_P enhancement (D4) did not have the greatest reduction in efficiency. The D7 duct had the worst extraction efficiency and did not provide as large an increase in C_P as D4 or D3. This was attributed to flow separation. All of the ducts displayed some degree of separation of the boundary layer from the interior duct surface. The duct drag was strongly influenced by the degree of flow separation which significantly reduced the extraction efficiency. Figure 3.4 shows the degree of flow separation for ducts D1, D4, D5 and D7 with $C_T = 0.8$. The black region is where the flow is reversed. It is clear that increasing flow separation leads to increased drag and therefore reduced extraction efficiency. Additionally, steady state solutions to flows with large regions of separated flows are known to have poor accuracy. This is particularly concerning for the D7 duct. Simulation results could be improved for such scenarios using an unsteady flow simulation with a LES or DES approach to turbulence modeling, however this has not been pursued due to a drastic increase in computational cost associated with these methods. In any case, massively separated flows are highly

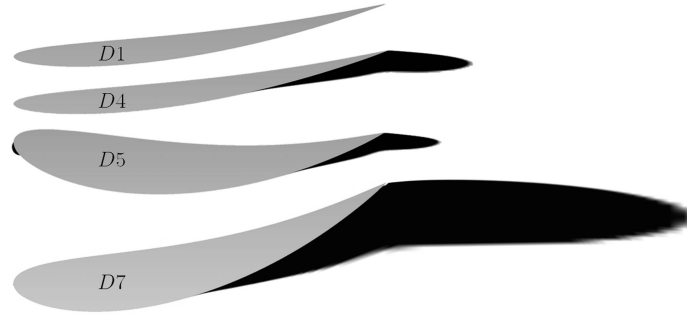


Figure 3.4: Depiction of separated flow region for ducts D1, D4, D5 and D7. The black region is where the flow is reversed

undesirable from a design perspective because they place large dynamic loads on the duct and rotor. Thus accurate simulation of such flows is unnecessary since realistic designs should not produce such behavior.

3.1.3 Results for Turbines with Equal Frontal Area

The results presented above show that a ducted turbine will produce more power than a non-ducted turbine if both have the same rotor area. Some authors (for example Fleming *et al.* [16]) argue that in making such comparisons, the total frontal area of the device should be held constant. This argument has reasonable grounds because the total area which can be occupied by turbines in a channel cross section is limited by the physical extents of the channel, and by practical considerations such as navigational requirements. This argument may also be made on economic grounds. The cost of a ducted turbine will be more similar to the cost of a non-ducted turbine with a rotor sized equal to the duct exit diameter than to one with a rotor sized equal to the ducted turbine rotor. Following this logic, the power and thrust coefficients should be normalized with respect to the frontal area of the duct ($A_f = A_4$).

$$\begin{aligned} C_{T2} &= \frac{T}{\frac{1}{2}\rho u_0^2 A_f} & C_{P2} &= \frac{P}{\frac{1}{2}\rho u_0^3 A_f} \\ C_{D2} &= \frac{T}{\frac{1}{2}\rho u_0^2 A_f} & C_{P_{lost2}} &= C_{T2} + C_{D2} \end{aligned} \quad (3.1.11)$$

It is important to note that re-normalizing the coefficients in this manner has no impact on the extraction efficiency but it does change the apparent benefit of using a duct to augment the flow through turbines. The power and thrust coefficients have been re-normalized in this manner and are re-plotted in figure 3.5. This shows that for a given size of device, the ducted concepts cannot generate as much power (and also cannot create as much turbine thrust) as their open flow counterparts. It is also instructive to observe the variation of the thrust and power coefficients with the power extracted from the flow. This is plotted in figure 3.6 and shows that while the open flow concept has the highest power generating capacity, it does so with the highest rotor loading (represented by C_{T2}). Thus, there is a tradeoff between rotor loading and power generation capability. The ideal non-ducted turbine always has a higher power production for a given power loss from the flow (i.e. the best extraction efficiency).

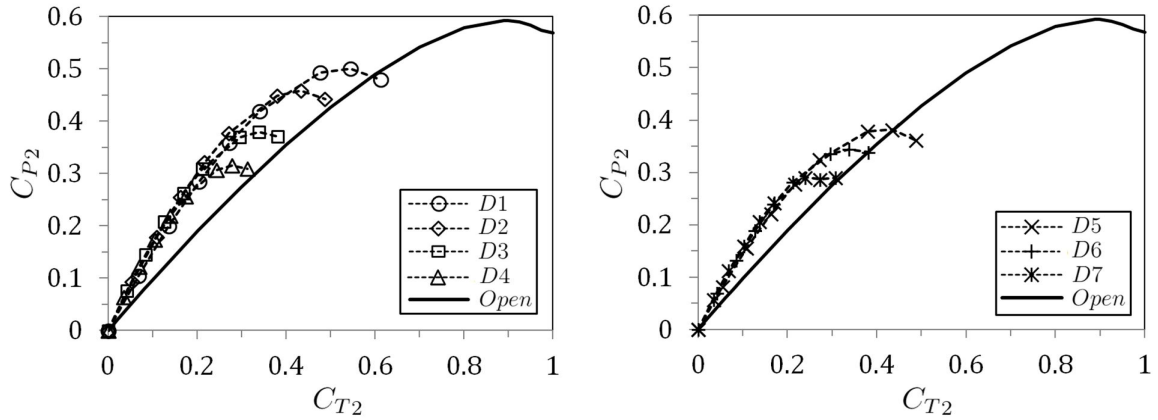


Figure 3.5: Power vs. thrust coefficient normalized by total projected frontal area

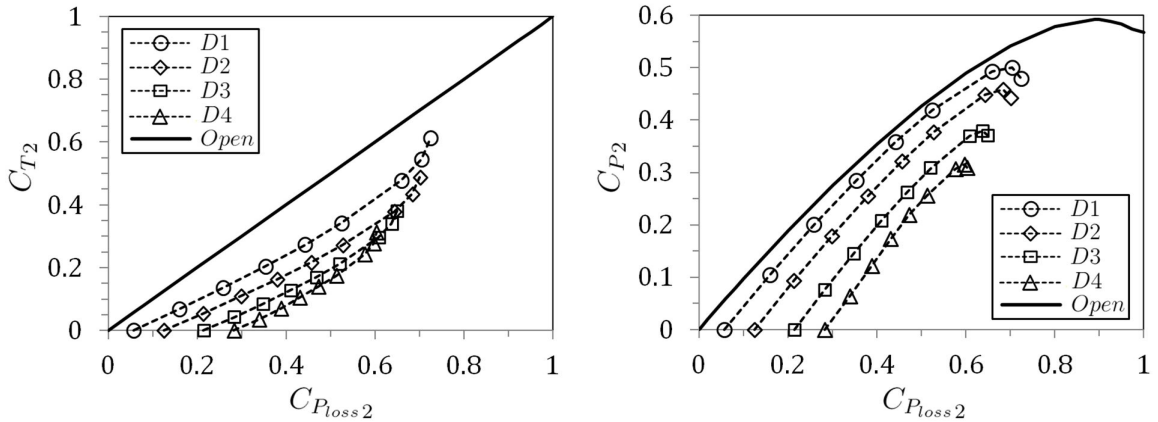


Figure 3.6: Variation of power and thrust coefficients with power loss coefficient, normalized by total projected frontal area

3.1.4 Sensitivity to Structural Drag and Tip Loss

The analysis of extraction efficiency to this point has assumed that the turbine rotor is ideal. In reality, there are power losses due to drag from supporting structures, blade drag, wake swirl, and tip vortices (tip-loss). The sensitivity of the power coefficient and extraction efficiency to these factors was studied in a rough manner at this preliminary stage in the research. Further studies refined methods to include the losses due to blade drag and wake swirl more accurately, and on defining the optimal turbine blade geometry and rotational speed for non-ideal turbines.

Structural drag was estimated based on the only installed commercial scale tidal turbine in operation, the SeaGen turbine by Marine Current Turbines [83]. The design features two rotors connected side-by-side on a horizontal boom of length $L_b = 29m$ and width $w_b \approx 1m$, which is mounted on a surface-piercing pile of diameter $d_p = 3m$ in water approximately $L_p = 30m$ in depth. Assuming a 3:1 elliptical shape for the boom, the drag coefficient based on frontal area is approximately $c_{d,ellipse} = 0.17$ in turbulent flow [84]. For a cylinder in turbulent flow, the drag

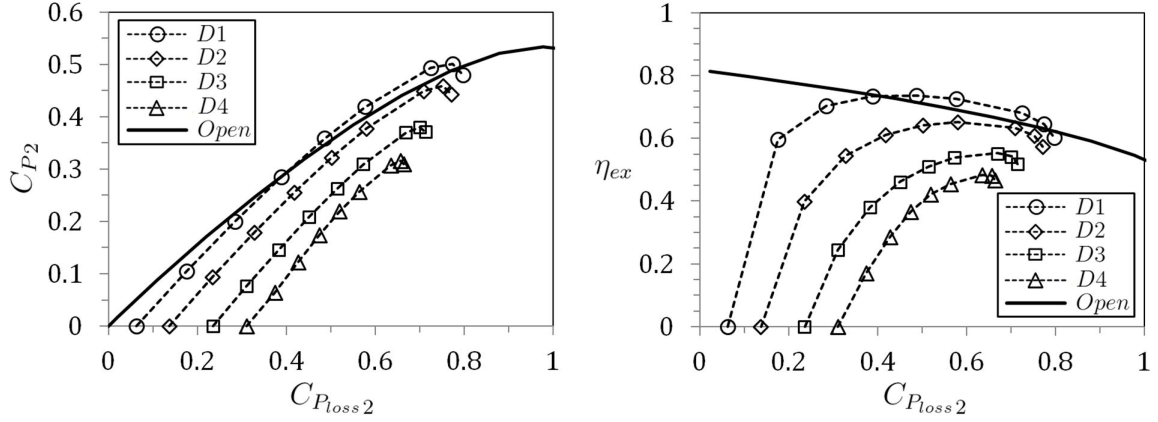


Figure 3.7: Variation of power and thrust coefficients with power loss coefficient, normalized by the total projected frontal area

coefficient based on frontal area is approximately $c_{d,cyl} = 0.3$ [84]. To use the above drag coefficients to determine the effect on efficiency, they are first renormalized with respect to the rotor swept area of $A_r = 377m^2$ as follows;

$$C_{D,boom} = c_{d,ellipse} \frac{L_b w_b}{A_r} = 0.0131 \quad (3.1.12)$$

$$C_{D,pile} = c_{d,cyl}(L_p d_p)/A_r = 0.0716 \quad (3.1.13)$$

For ideal non-ducted turbines, the maximum power coefficient occurs with a rotor loading of $C_T = 8/9$. Assuming this is the design point for the SeaGen turbine, then the structural drag adds approximately 10% to the total axial force in addition to the rotor thrust. A 10% increase in the total axial force was also assumed for ducted concepts for their support structures.

Tip losses were assumed to reduce the power production of the non-ducted turbine by approximately 10%. This was a crude estimate, which at the time was used merely to demonstrate the sensitivity of the extraction efficiency to tip loss. The effects of wake swirl and blade drag losses were assumed to be equivalent for both types of turbines, and were not included in this analysis. With these assumptions, revised estimates for the turbine performance metrics were calculated using:

$$\begin{aligned} C_{T2} &= \frac{T}{\frac{1}{2} \rho u_0^2 A_f} & C_{P2} &= \frac{0.9P}{\frac{1}{2} \rho u_0^3 A_f} \\ C_{D2} &= \frac{D}{\frac{1}{2} \rho u_0^2 A_f} & C_{P_{lost}2} &= 1.1(C_{T2} + C_{D2}) \end{aligned} \quad (3.1.14)$$

The factor 0.9 used in calculating the power coefficient was only applied to the non-ducted turbine as tip losses were assumed to be negligible when ducts are used. The resulting power coefficient and extraction efficiency are plotted in figure 3.7. It is apparent that when structural drag and tip loss are considered it is possible for a ducted turbine to have better extraction efficiency. However, for the same installed frontal area, the non-ducted turbine is still capable of producing more power.

3.1.5 Summary

This section has presented an analysis of the performance enhancements possible by using ducts to increase the flow velocity through the turbine rotor. In making comparisons between different designs, it is important to decide whether the rotor area, or total frontal area should be held constant. In reality, this choice will be made clear by realistic cost estimates of ducted and non-ducted turbines. In holding the rotor area constant, the increased power attributed to using a duct is apparent. In holding the total frontal area constant, the non-ducted turbine can produce the greatest power. The extraction efficiency is a parameter which does not depend on which perspective is taken and in that sense is a more universal metric for comparison. When including crude estimates of tip loss and structural drag effects, the least aggressive duct design had a marginally higher extraction efficiency than the non-ducted turbine, but still produced less power for a given total frontal area. These results are discouraging for ducted concepts, but the idealization of the turbine rotor overpredicted the power of all concepts, so more refined methods were necessary to improve the analysis.

Later studies worked on modeling non-ideal rotors. However, to compare ducted and non-ducted concepts using non-ideal rotors, it was realized that a fair comparison could only be made if the rotor was optimized for the duct. Thus, rotor optimization methods (sections 2.3.6 and 2.4.9) had to be developed. Additionally, it was desired to make the comparison between ducted and non-ducted turbines using a realistic case study of power generation in a real tidal channel. To do this, methods of capturing channel blockage effects and the feedback of turbine power extraction on the tide driven flow described in section 2.6 were also required.

3.2 Fitting Parameters for the Empirical Duct Performance Model

During the course of this thesis it was realized that while the BEM method was applied almost universally to the design of non-ducted turbines, ducted turbine design work relied very heavily on computational fluid dynamics. An accurate analytical/empirical extension of BEM to ducted turbines would allow faster prototyping iterations during early design stages, and in later unsteady fatigue simulations. A literature review (summarized in section 2.3) revealed that several analytical treatments were available for extending the BEM method for ducted turbines, but they required determining empirical model parameters that quantify several effects unique to ducted flows which are inherently beyond treatment with purely analytical flow descriptions. The axial-only (i.e. for ideal rotors) actuator disk CFD model (section 2.4) provided a convenient means to determine the required model parameters for a range of duct geometries. It was found that accurate curve fits for these parameters could be developed based on geometric features of the ducts. The result was a surprisingly accurate treatment for ducted turbines (with ideal rotors) which shed the dependence on time-consuming CFD simulation. In addition to this important contribution, parameterizing the duct performance in the manner done here provides greater insight into duct performance than just observing thrust and power coefficients and extraction efficiency, which were discussed in the previous section.

The model framework is discussed in section 2.3.2. Here, the determination of the empirical model parameters and curve-fits is discussed. Section 3.2.1 presents the inlet efficiency $\bar{\eta}_{02}$, diffuser efficiency $\bar{\eta}_{34}$ and base pressure coefficient $c_{p,b}$ determined by axial-only actuator disk simulations. Section 3.2.2 presents the curve fits which define the empirical duct model based on duct geometry and validation of the empirical model against CFD results. Following this, the effect of boundary layer flow control is also briefly discussed in section 3.2.3.

3.2.1 CFD Results

The simulations used for this study assumed ideal rotors, and only applied axial forcing terms to the flow. This section presents the simulation results for the inlet and diffuser efficiencies, base pressure coefficient and power coefficient for each duct. Note that figures showing these results (figures 3.8 and 3.9) also include predictions of the empirical curve fits (described in section 3.2.2) which define the empirical duct performance model, and are labeled ‘model.’

The thrust and power coefficients were calculated as described in section 2.4.5 for axial-only CFD simulations. To calculate the model parameters, a streamline passing through the duct leading edge stagnation point and the duct trailing edge was defined to isolate the flow passing through the duct. Planes were then defined at stations 0 through 6 (see figure 2.6) bounded by this streamline. This allowed calculation of the area-averaged velocity, pressure, and stagnation pressure at each station. This was achieved using automated post-processing algorithms written in the CFX scripting language. These area-averages were then used to calculate the model parameters as described below.

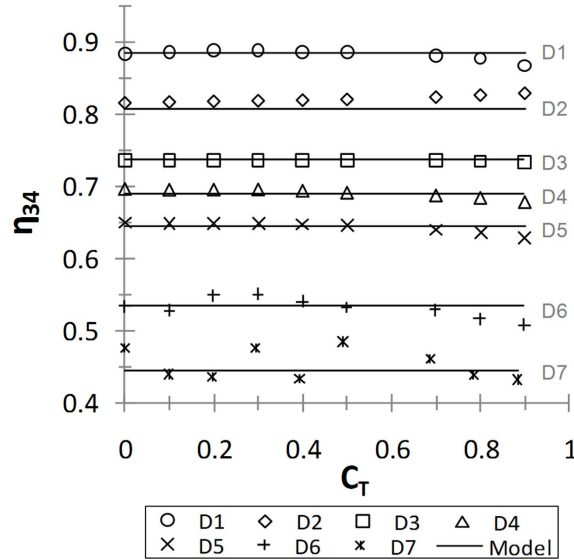


Figure 3.8: Empirical model prediction of η_{34} (solid line) compared to CFD results for development cases D1-D7 (symbols)

Inlet Efficiency

The inlet efficiency was found using:

$$\bar{\eta}_{02} = \frac{\bar{p}_2 - p_0}{1/2\rho(u_0^2 - \bar{u}_2^2)} \quad (3.2.1)$$

Note that this efficiency term is very sensitive to discrepancies in the pressure when u_2 approaches u_0 , which occurs at a specific C_T for each duct when the freestream ingested flow area equals the rotor area. This sensitivity can be avoided by assuming that the efficiency calculated for $C_T = 0$ is appropriate for all values of C_T . The inlet efficiency was not expected to show significant variation with C_T because unlike in the diffuser, flow separation is very unlikely in the inlet and the efficiency is primarily due to friction over a relatively constant surface. The inlet efficiency was typically within 5% of unity, and simply assuming a value of unity had little impact on the power calculated by the model.

Diffuser Efficiency

The diffuser efficiency was calculated using:

$$\eta_{34} = \frac{\bar{p}_4 - \bar{p}_3}{1/2\rho\bar{u}_3^2\left(1 - \frac{A_3^2}{A_4^2}\right)} \quad (3.2.2)$$

which accounts for viscous loss and flow separation. The diffuser efficiency is shown for ducts D1 to D7 in Fig. 3.8. As expected, it was observed that as (A_4/A_3) and $\theta_{4,in}$ grow, the diffuser efficiency diminishes due to increasing flow separation. The efficiency was nearly constant with C_T .

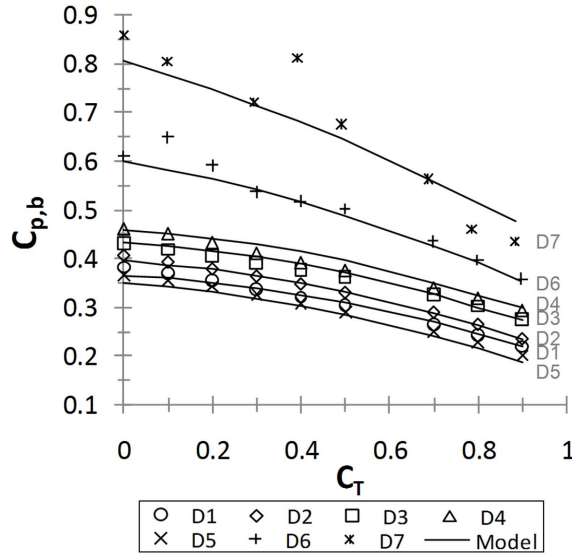


Figure 3.9: Empirical model prediction of $C_{p,b}$ (solid line) compared to CFD results for development cases D1-D7 (symbols)

Base Pressure Coefficient

The base pressure coefficient was calculated using:

$$\bar{c}_{p,b} = \frac{p_0 - \bar{p}_4}{\frac{1}{2}\rho u_0^2} \quad (3.2.3)$$

and is plotted in Fig. 3.9 for ducts D1 to D7. The base pressure coefficient was seen to increase in magnitude with (A_4/A_3) and $\theta_{4,out}$ and to decrease with increasing C_T , as seen in Fig. 3.9.

Power Characteristic

The power coefficient is plotted as a function of C_T for ducts D1 to D7 in figure 3.10. Note that C_P and C_T are both normalized using the rotor area A_r (as opposed to the total frontal area A_f) in this section. The first four duct designs maintained a constant diffuser outlet angle of 19° while changing the duct expansion ratio. The effect of this was as expected for cases D1 to D3, with larger expansion resulting in greater C_P enhancement. However, D4 showed little further improvement over D3 as the area ratio increased from 2.36 to 2.87.

The next set of ducts (D5-D7) was created to test the impact of outlet angle on performance. It was observed that large outlet angles reduce the diffuser efficiency due to increased flow separation, but also provide a greater base pressure effect due to blockage of the flow exterior to the duct. Flow separation from the inner surface of the duct essentially creates a smaller core flow, reducing the effective expansion by the diffuser.

Ducts D8-D10 were used to test the variation of duct performance with expansion ratio for larger outlet angles than the first four ducts. The results of these ducts are not explicitly shown in this thesis for brevity, and because the trends observed were consistent with ducts D1 to D7. In general,

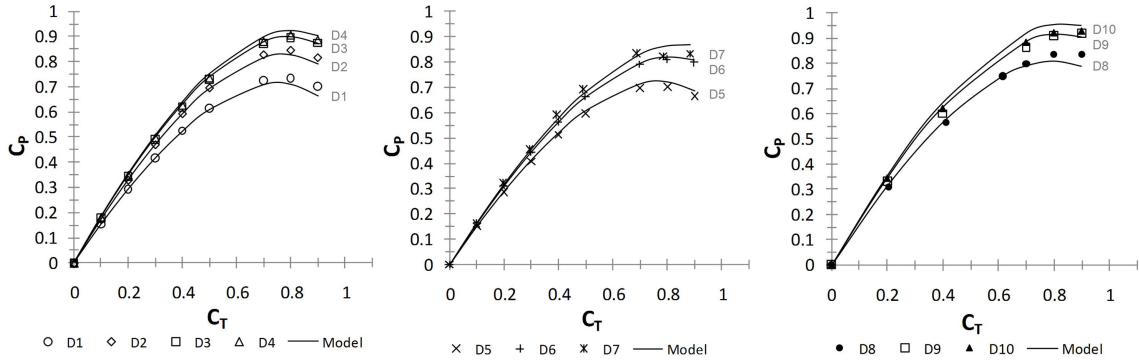


Figure 3.10: Empirical model prediction of C_P (solid line) compared to CFD results for development cases D1-D7 (symbols)

a larger outlet angle led to greater base pressure and lower diffuser efficiency. As with the first four ducts, the diffuser efficiency was best for a small expansion ratio and the base pressure was greatest for the largest expansion ratio.

3.2.2 Fitting The 1D Empirical Duct Model

Development

The diffuser efficiency and base pressure coefficients were parameterized as functions of duct geometry and thrust coefficient. Using a trial and error based approach of increasing term order, appropriate functional forms shown in equations 3.2.4 and 3.2.5 were determined. Note that η_{34} depends on the inner outlet angle $\theta_{4,in}$ expansion ratio A_3/A_4 and inlet contraction ratio A_1/A_2 . Physically, this is a reasonable set of parameters to define the diffuser efficiency, which characterizes the flow separation behaviour within the duct. The diffuser efficiency was modeled as having no dependence on C_T based on the observed CFD results. The base pressure coefficient depends on the expansion ratio A_3/A_4 , outer outlet angle $\theta_{4,out}$ and C_T . This set of parameters also seems to have some physical validity for defining $C_{p,b}$ since it characterizes the flow blockage effect of the entire duct/turbine system.

$$\eta_{34} = a_1 + b_1 \frac{A_3}{A_4} + c_1 \theta_{4,in} + d_1 \frac{A_1}{A_2} \quad (3.2.4)$$

$$C_{p,b} = a_2 + b_2 \frac{A_3}{A_4} + c_2 \theta_{4,out} + (d_2 + e_2 \theta_{4,out}) C_T + f_2 C_T^2 \quad (3.2.5)$$

The coefficients for the above equations were found using a least squares optimization of the CFD data for ducts D1 through D10 and are summarized in Table 3.1. Except for a few outliers, the above correlations agree very well with the simulated values. Fig. 3.11 shows the model values plotted against the simulation results for all ducts. Fig. 3.8 shows the modeled diffuser efficiency for ducts D1 to D7 plotted alongside CFD results.

The base pressure coefficient found by the model is plotted against C_T and compared to the simulation results in Fig. 3.9. It is clear that the model matches the simulation results quite well except for several points for D7. The simulation results for this duct are somewhat questionable as

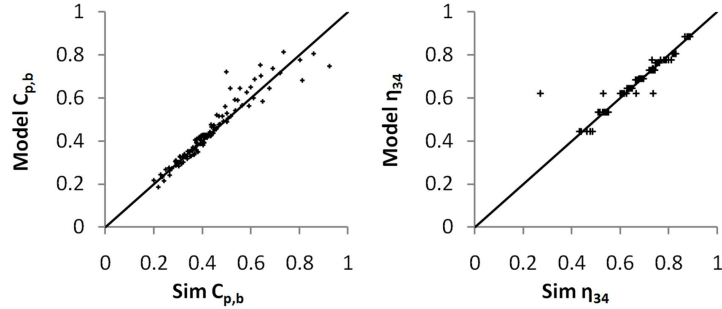


Figure 3.11: Correlation plots for diffuser efficiency (left) and base pressure coefficient (right); the solid line shows a 1:1 correlation

Coeff.	Value	Coeff.	Value
a_1	0.8867	b_2	-0.3330
b_1	0.5212	c_2	0.0269
c_1	-0.0108	d_2	0.1068
d_1	-0.1313	e_2	-0.0152
a_2	0.2701	f_2	-0.1275

Table 3.1: Regression model coefficients

the flow displayed transient behaviour even though the simulations were run as steady state. This is likely due to the unsteady nature of a large separated flow region for duct 7 and was not an issue for the other cases.

Using the modeled diffuser efficiency (eq. 3.2.4) and base pressure coefficient (eq. 3.2.5), and assuming an inlet efficiency of unity, duct performance was predicted for the development cases D1-D10 using eqs. 2.3.6 and 2.3.7. A comparison to the CFD results is shown in Fig. 3.10, which shows a good match. It is to be expected that a good match would be achieved with the development cases. As with any regression based model, a separate dataset from that used to derive the model should be used for validation, which is discussed in the next section.

Validation

Validation was done using the ducts V1 to V3, which were not used in determining the model coefficients above. The empirical model was used to predict the performance of each duct and subsequently compared to CFD results. The diffuser efficiency is shown in Fig. 3.12. Note that the CFD simulations for case V2 did not converge well for C_T below 0.7, giving questionable results. As with case D7 this poor convergence was due to transient behaviour due to a large region of separated flow. The base pressure coefficient is shown in Fig. 3.13. Finally, the performance characteristic of each validation case is shown in Fig. 3.14. The model produces a reasonable approximation of the CFD results for all three validation cases.

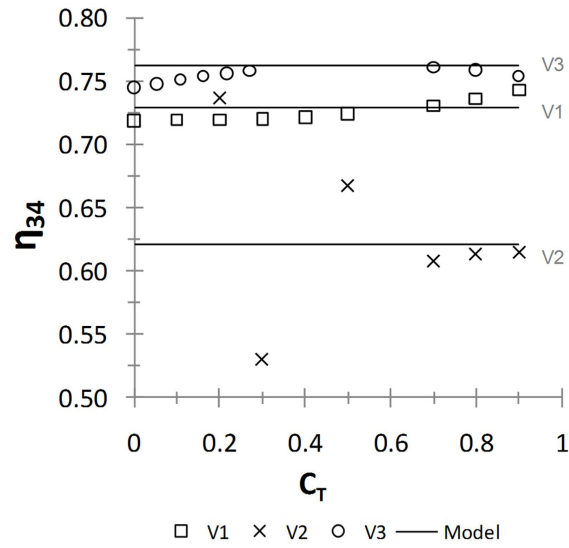


Figure 3.12: Empirical model prediction of η_{34} (solid line) compared to CFD results for validation cases V1-V3 (symbols)

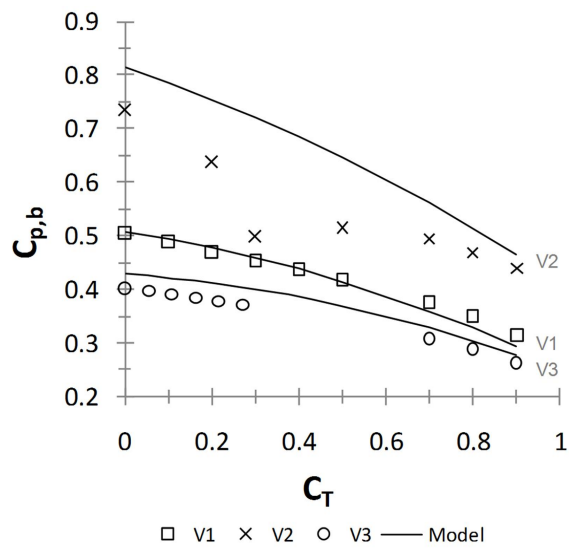


Figure 3.13: Empirical model prediction of $C_{p,b}$ (solid line) compared to CFD results for validation cases V1-V3 (symbols)

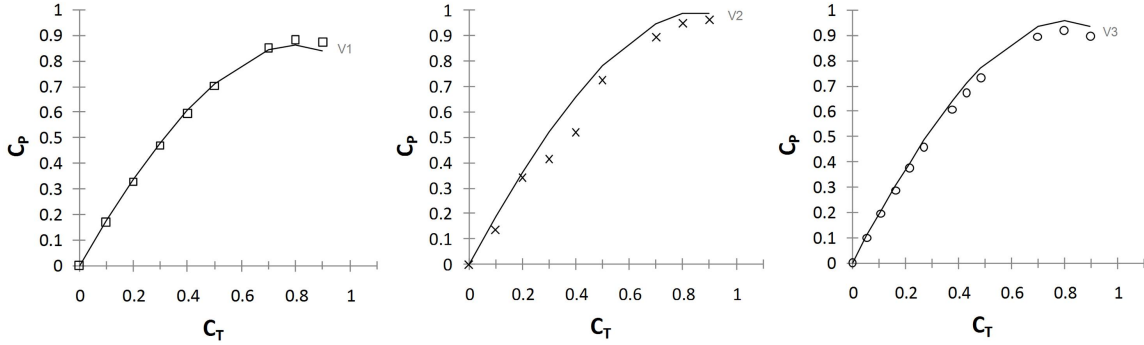


Figure 3.14: Empirical model prediction of C_P (solid line) compared to CFD results for validation cases V1-V3 (symbols)

3.2.3 Boundary Layer Flow Control

It is possible to delay flow separation in the diffuser by incorporating features that add momentum to the boundary layer. This sort of design feature was approximated in [1] using a small gap between the edge of the actuator disk and the duct surface. The gap was also included in several simulations over the course of this study to observe the impact on the flow field and turbine performance.

For the cases including the gap, it was found that increasing C_T was accompanied by reducing flow separation and increasing diffuser efficiency. For these cases, greater turbine thrust led to more mass flow being diverted through the gap and therefore greater momentum transfer to the boundary layer. This behaviour can be observed in Fig. 3.15, which shows the fast flowing jet, increased velocity through the duct and reduced flow separation which arise when the gap is present. The gap had the most pronounced effect with the most aggressive ducts; for example the maximum C_P for D7 increased from 0.85 without the gap to 1.14. Such a jet is unlikely to occur in real turbines unless the solidity ratio is very high or other design features, such as the slotted diffusers used by Grumman researchers [13, 47], lead to its presence. The performance gains possible with boundary layer flow control are likely significant. However, attempts to develop empirical relationships for the diffuser efficiency for the cases including the gap did not produce useful correlations due to increased flowfield complexity.

It is unlikely that a small clearance between the actual blade-tips and duct surface would have the same impact on the flowfield as a gap in the actuator disk approximation. This is because the disk approximates an infinite number of blades, and when discrete blade effects are considered, flow could be diverted around the blades as well as towards the duct surface. The true influence of blade tip clearance cannot be modeled accurately using an actuator disk model and requires more advanced CFD models or experimental work to quantify accurately.

3.2.4 Summary and Discussion

Using the axial flow actuator disk CFD model, several duct designs were simulated. These simulations provided insight into the factors influencing the performance enhancement provided by ducts:

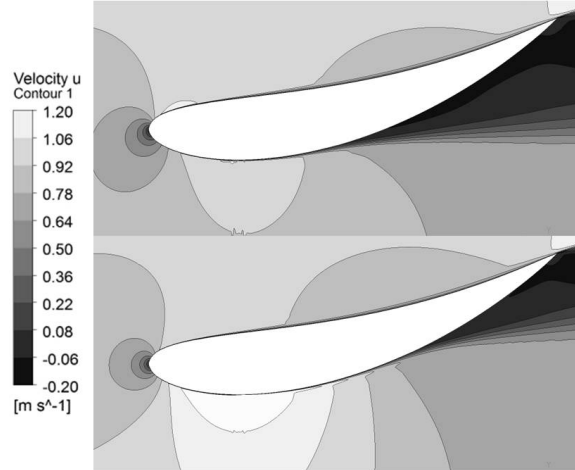


Figure 3.15: Axial velocity contours for duct D7 without, (top) and with (bottom) the gap between the actuator disk and duct surface. Note the higher velocity at the duct throat when the gap is present.

viscous loss, flow separation and base pressure. It was found that viscous loss in the inlet was essentially negligible for the considered cases. Flow separation of the boundary layer in the diffuser section led to significant performance degradation characterized by a reduction in the diffuser efficiency. It was found that the diffuser efficiency decreases with increasing diffuser expansion, inlet contraction and inner exit angle. The diffuser efficiency was not seen to vary greatly with thrust coefficient except for cases which included a small gap between the edge of the actuator disk and the surface of the duct. In such cases the efficiency improved with increasing C_T as discussed above. This observation shows that boundary layer flow control may be important for practical designs. The base pressure effect provides a significant performance enhancement and is seen to grow with diffuser expansion ratio and outer exit angle but diminish with increasing C_T .

In duct design, moving towards larger expansion ratios and larger outlet angles provides increased base pressure, but diminished diffuser efficiency. The maximum performance occurs when the marginal gain from increasing the base pressure effect is equal to the marginal loss from decreased efficiency. This may explain the rationale behind pursuing a flanged diffuser which creates a large base pressure effect by blocking the external flow near the duct exit, a strategy which has been investigated by Setoguchi [50] and Abe et al. [51]. It is of practical importance to note that most tidal turbine concepts do not rotate during slack tide and thus include a pair of inlet/diffusers to allow performance gains on both the ebb and flood tides. In such designs, the upstream ‘diffuser’ will disrupt the flow, potentially reducing the performance augmentation of the downstream diffuser. Thus the unidirectional flow diffuser designs presented here likely provide an optimistic estimate of ducted-turbine performance.

An empirical model for diffuser efficiency and base pressure was derived through curve-fitting which provides a good match to the CFD results. This regression based model performs reasonably well for ducts with geometric features within the ranges used in this study. No work has been done

to validate the model beyond these ranges, however the trends identifying the geometric features which affect the diffuser efficiency and base pressure coefficient are expected to hold over a wide variety of duct designs.

For novel duct designs, or any designs including boundary layer flow control, CFD simulation and experimental work will remain critical for analyzing performance. However, the results presented here show that an empirical model is feasible for simple ducted turbine concepts.

3.3 CFD-Based Blade Design: Sample Results

The CFD based optimization tool described in section 2.4.9 was used to determine the optimum rotor loading (in a design search space with $\Delta_{C_T} = 0.05$, $\Delta_{C_{nu}} = 0.1$ and $\Delta_\lambda = 1$) for ducts D1 and D4. Unlike in the previous two studies, the actuator disk CFD simulations used by the CFD-based optimization tool included azimuthal forcing terms and thus did account for blade drag and wake swirl effects. Sample results of the optimization algorithm for two duct geometries are described in this section. This optimization tool is of practical interest because it provides a methodology to optimize turbines for any arbitrary duct geometry. Optimizing the coupled duct/rotor system is a more complex task that will need to be dealt with in future studies if ducted designs are pursued. The optimization tool was later expanded upon as described in section 2.6.9 and used for optimizing turbines in a fence configuration in the context of a real-world tidal channel, as described in section 3.6.

3.3.1 The Uniformly Loaded Case

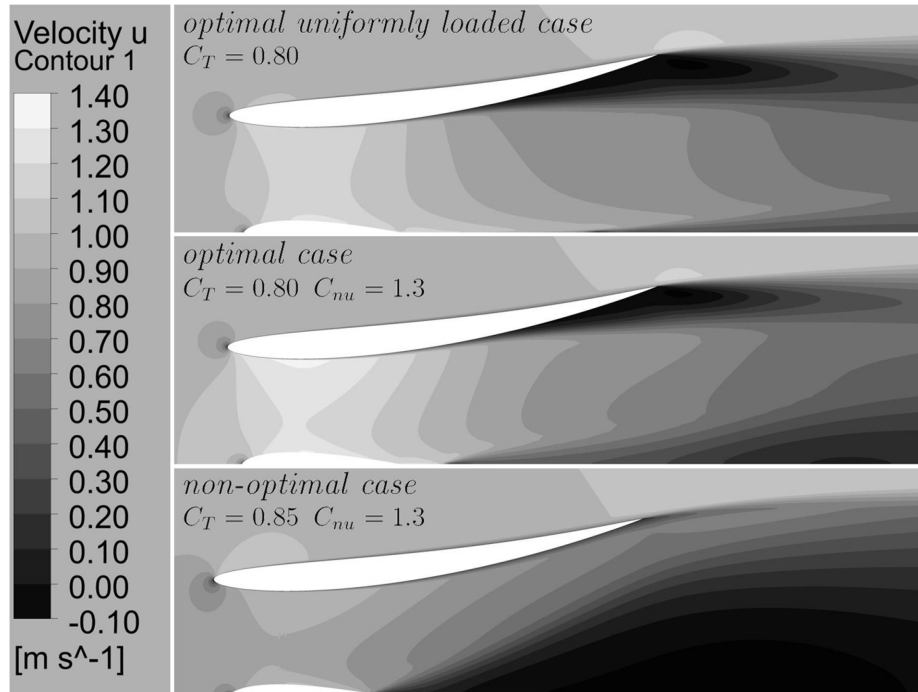
It has been established in texts such as [54] that for an ideal actuator disk in an unbounded flow, uniform axial loading gives optimal performance. This may not necessarily be the case for ducted rotors. Simulation results presented earlier in this thesis (section 3.1.2) showed that flow separation of the duct boundary layer is a limiting factor in the performance enhancement that can be achieved using a diffuser. It was thought that by loading the disk more heavily near the center, and more lightly near the blade tips, some flow could be diverted towards the duct surface, energizing the boundary layer and delaying flow separation. This ought to give an overall performance enhancement by allowing increased mass flow through the turbine. As a baseline case, the uniformly loaded disk was optimized by modifying the optimization algorithm to keep C_{nu} (which defines the slope of the thrust distribution with radius as described in section 2.4.3) constant at a value of 1.0, which provides a uniform thrust distribution. The algorithm was run for both the D1 and D4 ducts and the results are summarized in table 3.3.2. The axial flow for the D4 case is shown in the top plot of figure 3.16, which shows the large region of separated flow along the downstream portion of the duct surface.

3.3.2 Non-Uniform Loading Cases

To evaluate the impact of non-uniform loading, the optimization algorithm was run allowing C_{nu} to vary freely; the results were as expected. The improvement in C_P was negligible for the D1 duct, which was expected because this design did not have any flow separation in the uniformly loaded scenario. The D4 duct performance, on the other hand showed a 7.3% improvement in C_P using an optimum non-uniform loading parameter of $C_{nu} = 1.3$. The associated flowfield shown in the middle plot of figure 3.16 had a reduced separated flow region, and increased axial velocity at the rotor plane.

Table 3.2: Summary of load optimization algorithm results for the D1 and D4 ducts.

Duct	constr.	Initial				Final				# sims.
		C_T	C_{nu}	λ	C_P	C_T	C_{nu}	λ	C_P	
D1	uniform	0.85	1.0	4	0.662	0.75	1.0	3	0.673	8
D1		0.75	1.0	3	0.673	0.75	1.1	3	0.675	7
D4	uniform	0.85	1.0	4	0.819	0.8	1.0	4	0.822	7
D4		0.85	1.0	4	0.819	0.8	1.3	4	0.885	14

Figure 3.16: Contours of axial velocity for the D4 duct: Uniform loading with $C_T = 0.8$ (top), and non-uniform loading cases with $C_T = 0.80$, $C_{nu} = 1.3$ (middle) and $C_T = 0.85$, $C_{nu} = 1.3$ (bottom).

3.3.3 Robustness of Design

It is important to note that the D4 case with the best performance is very similar to that with the worst. When C_T was increased from the optimal value of 0.80 to 0.85, C_P dropped from 0.88 to 0.68. This large degradation in power was associated with a region of reversed flow just downstream of the turbine near the center of the wake, clearly shown in the bottom plot of figure 3.16. Such an abrupt change in flow behaviour is a concern for design purposes; while the determined optimum design point does maximize performance at the design condition, the off-design performance may suffer drastically. Additionally, such an unstable flow regime could lead to large fluctuations in the applied loads on the structure, leading to early failure. Thus, caution needs to be applied in applying CFD-based optimization tools which design for a single optimal operating condition. It may be beneficial to design the rotor to operate at a slightly lower loading than the optimum determined by this algorithm to reduce the possibility of the flowfield transitioning into this undesirable regime.

3.3.4 Blade Geometry and Performance

For the optimized cases, the blade geometry was determined using the methods defined in section 2.4.6. The chosen airfoil for the design was the DU91-W2-250, with a maximum l/d of 39.67, and corresponding lift and drag coefficients $c_l = 0.922$, $c_d = 0.023$, which occur at an angle of attack of $\alpha = 6.28^\circ$. Note that wind turbines often have a lift-to-drag ratio exceeding 100, so the value of 40 used here is quite conservative. This conservative value was chosen because it was thought that due to factors such as increased structural requirements, bio-fouling and highly turbulent flow, the maximum achievable l/d would be lower in a marine environment than in the context of wind energy. The calculated blade properties are shown in figure 3.17. The leftmost plot shows the solidity, which is defined as the length of B blade chords as a percentage of the circumference of a circle at a given radius. Near the blade root, the solidity is nearly 80% for both ducts. Note that a solidity exceeding 100% could be achieved by having overlapping blades, but would require accounting for cascade effects. The middle plot shows the ratio of chord to turbine radius for designs using $B=6$ blades. Because an actuator disk approach has been used and there is no model applied for discrete blade effects, the turbine performance does not depend on the number of blades. This allows the number of blades to be defined after the CFD-based optimization has found the optimal configuration.

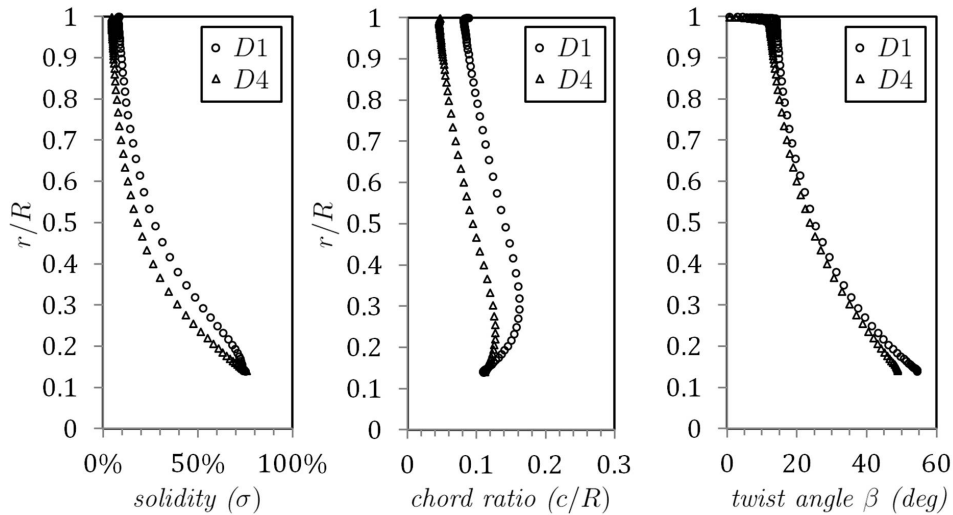


Figure 3.17: Determined optimal blade properties for the D1 and D4 ducts

The D1 duct uses a significantly wider blade than the D4 duct. This is mainly due to the lower optimal tip speed ratio (3 vs. 4) used by the D1 case, which reduces the blade relative velocity, thus requiring a larger chord to achieve a similar rotor loading. The rightmost plot in figure 3.17 shows the blade twist distribution. Again the differences in the twist distribution arise primarily from the different tip-speed ratio affecting the local inflow angle. These results make it clear that the optimal blade profile will be significantly different from one duct to the next. It is also of interest to note that depending on the power takeoff system, the blades may be attached to a central hub, or to an annulus housed inside the duct. In the latter scenario the blades would extend into the duct, leaving no clearance between the duct surface and blade tip. This has important implications

regarding blade tip loss, since such a blade could maintain a relatively constant circulation right to the blade tip, preventing the formation of tip vortices and thus preventing tip-loss. Indeed this is what Flemming *et al.* [16] have found using CFD simulations which resolved the turbine blades explicitly. This finding justifies neglecting to use a tip-loss model in the actuator disk CFD approach.

The local thrust and power coefficients were calculated using equations 2.4.28 and 2.4.31 and are shown in figure 3.18. In both cases, the linear trend in c_T (which arises from the C_{nu} parameter) is evident, with more thrust at the root than the tip, although for the D4 duct the slope is much larger. The local power coefficient for the D1 duct shows an increasing trend towards the blade tip, while for the D4 duct, there is a local maximum at approximately 35% radius, beyond which the local c_P decreases gradually. These opposing trends arise due to the distribution of loading and the flowfield which is influenced by both the duct and the rotor. Because of the multiple influences acting on the flow field it is difficult to deduce a general explanation to account for these opposing trends, however the primary factor seems to be the thrust distribution. It is important to note that in finding the total power coefficient, the local c_P are added together in a weighted sum where the weights are the local annular area. Thus, the c_P near the blade tip have the highest influence on the total C_P .

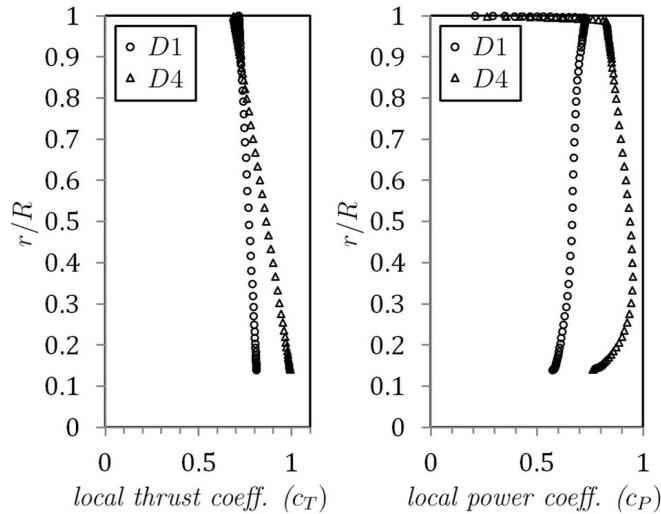


Figure 3.18: Optimal local thrust and power coefficients for the D1 and D4 ducts

The flow field at the rotor plane is given in terms of induction factors in figure 3.19. The leftmost plot shows the radial induction defined as $a_r = u_r/u_0$. The radial flow is mainly governed by the duct inlet and hub geometries at the rotor plane. Radial flows are of interest because they contribute to 3D flow effects on the blades, which are not considered in detail in this thesis, and are reserved for future studies. The middle plot shows the axial induction, which takes on negative values because the flow has been accelerated by the duct. Note that the flow is significantly faster in the D4 duct due to a much larger expansion ratio. This accounts for its higher power coefficient. Both designs have a region of relatively higher velocity at the blade root, which arises due to the effect of wake swirl enhancing the axial flow and due to flow acceleration around the hub. The rightmost plot

shows the tangential induction, which behaves as expected with the highest tangential velocity at the root and a trend towards zero at the tip. The higher tangential induction in the D1 duct is attributed to its lower tip speed ratio, which increases the inflow angle, making the blade lift force more closely aligned to the azimuthal direction, thus resulting in increased tangential velocity in the wake.

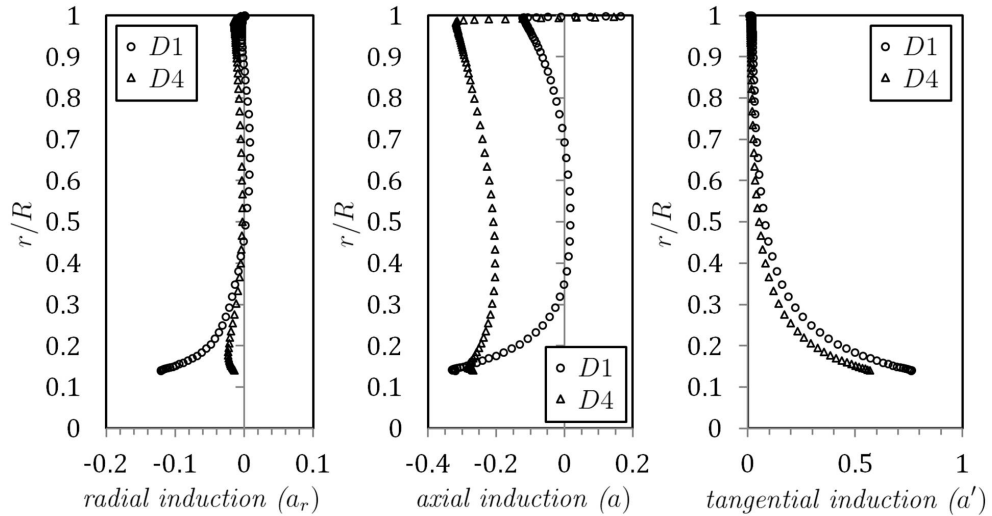


Figure 3.19: Induction factors for the optimal configurations for the D1 and D4 ducts

3.3.5 Summary

A simple algorithm was used to determine the set of input parameters (C_T , λ and C_{nu}) that maximize the power of turbines using the D1 and D4 ducts within a set level of granularity. This approach is reasonably fast, requiring approximately 10 to 30 minutes per simulation. The number of iterations until the design converges depends on how precisely the optimum parameters are to be defined. Here, the precision on C_T , λ and C_{nu} was 0.05, 1 and 0.1, respectively, and the optimization required approximately 4 hours to run using 4 parallel processes on a recent (2009) i7core PC.

The model revealed that it is feasible to use a non-uniform turbine loading to improve overall performance of a ducted turbine by reducing flow separation in the diffuser. Using a non-uniform loading therefore may allow a large performance enhancement without the added design complexity of other boundary layer flow control devices. The gain in power using such a strategy is reduced when the flow separation in the uniformly loaded case is small to begin with, as demonstrated by the results presented for the D1 duct.

Using an actuator disk model may cause an over-estimation of the benefit of a non-uniform loading, since with discrete blades the flow could be diverted between the blades instead of radially outward. This would produce less transfer of momentum to the boundary layer and less reduction of flow separation. Actuator line CFD simulations (which account for discrete blade effects explicitly) done separately from this thesis work have confirmed that accounting for discrete blade effects for

the D4 duct gives approximately 5% lower C_P for the optimal configuration determined in this section, consistent with the above arguments.

The results of this optimization were later used as a baseline for comparison for studies which used the DuctBEM model (section 2.3) to analyze ducted rotor performance and to optimize turbine blades. The optimization technique was also expanded upon (section 2.6.9) and used for optimizing turbines in a fence configuration in the context of a real-world tidal channel, as described in section 3.6.

3.4 Comparing the DuctBEM model to CFD Results

This section uses the DuctBEM model (section 2.3) to calculate the performance of the optimal rotor for the D4 duct, as determined in the previous section, to CFD results. The DuctBEM model relies on the duct performance parameters (diffuser efficiency and base pressure coefficient) which are defined by the 1D empirical duct model described in section 3.2.2. The 1D empirical duct model, however, used simulations which only included axial flow, and assumed that the duct performance coefficients $c_{p,b}$ and η_{34} were constant with radius. To eliminate errors associated with these assumptions, the diffuser efficiency and base pressure coefficients were determined for a series of concentric annuli for the specific duct and optimal loading condition. Using these parameters, the DuctBEM model gave results very close to the CFD simulations, which validated that it was formulated correctly from a flow physics perspective. Building an accurate set of response surface models representing how $c_{p,b}$ and η_{34} vary with duct geometry, loading condition and radial position would be a complex and difficult task. Thus the errors associated with 1) assuming that the diffuser efficiency and base pressure coefficient are constant with radius and 2) using simulations that don't include tangential forcing terms when determining the duct performance parameters were assessed.

3.4.1 Baseline Turbine Performance

To evaluate the validity of the DuctBEM model, results from actuator disk CFD simulations for the D4 duct (presented in section 3.3) were used as a baseline for comparison.

The CFD simulation results from section 3.3 were used to calculate the base pressure coefficients $c_{p,b}$, swirl pressure coefficients $c_{p,sw}$ and diffuser efficiency η_{34} . Note that this simulation included azimuthal forcing terms, and thus included the effects of wake swirl. The radial variation of the duct parameters was determined by dividing the flow by a series of streamlines as described in section 2.3.3. The diffuser efficiency η_{34} was evaluated for each streamline using equation 2.3.10, the base pressure coefficient was found using equation 2.3.12 and the swirl pressure coefficient was calculated using equation 2.3.8. The results are plotted in figure 3.20, and are specific to the D4 duct, the specific operating condition and the optimized blade. The sum of $c_{p,b}$ and $c_{p,sw}$ is also shown because this quantity can be readily measured from physical experiments, whereas the specific contribution of each component is more difficult to determine because it requires precise measurement of the swirl velocity just downstream of the rotor. As expected, the swirl pressure coefficient is greatest at the rotor centerline, where the highest tangential velocity is found. Note that the base pressure coefficient and diffuser efficiency do vary significantly with radius.

To test the physical accuracy of the DuctBEM model, the diffuser efficiency and base pressure determined from the CFD simulation as described above were input directly into DuctBEM. The swirl pressure coefficient was calculated on the fly from the tangential induction using equation 2.3.9. The resulting axial induction, angle of attack, and thrust and power coefficients are compared to the CFD results in figure 3.21. There is an excellent match between the CFD and DuctBEM models. This validates the DuctBEM model formulation and the methods of calculating $c_{p,sw}$, $c_{p,b}$ and η_{34} presented in this thesis.

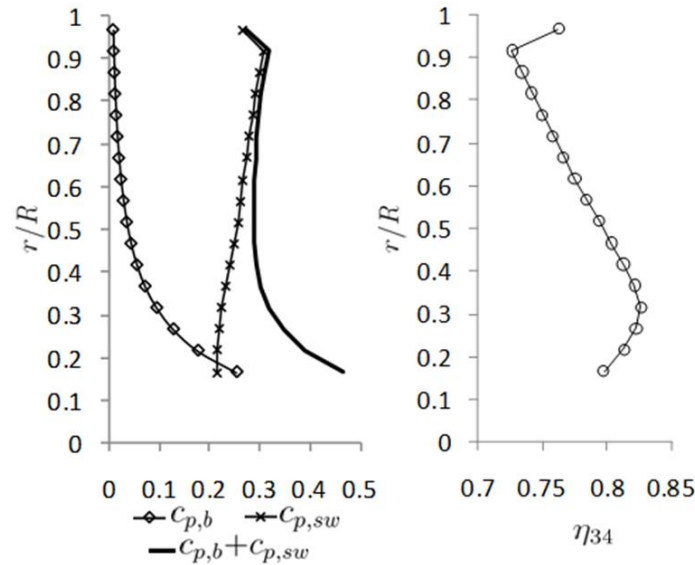


Figure 3.20: Radial variation of η_{34} , $c_{p,b}$ and $c_{p,sw}$ as calculated from CFD simulation results for the optimized rotor from section 3.3 for the D4 duct

The model coefficients used to produce these results are of course specific to this duct, blade design and tip speed ratio. To achieve the same accuracy over a range of blade designs and tip speed ratios, it would be necessary to create response surface models for η_{34} and $c_{p,b}$ over a wide range of turbine configurations. This would require a large number of CFD simulations or experiments and may not be worth the effort if a simpler model could achieve an acceptable level of accuracy. For this reason, several options for simplified models are presented in the following sections.

3.4.2 Simplified Duct Parameter Models

The effort expended in determining response surface models for the base pressure coefficient and diffuser efficiency depends on the type of experiments and/or simulations to be run, as well as whether or not the radial variation of the duct parameters is taken into account. The most complex experimental campaign would involve detailed measurements of the flowfield and pressure for a real turbine rotor in a duct, including the radial variation of the duct parameters. A large amount of data would be required to create response surface models valid over a range of operating conditions. If a variety of ducts were to be tested, the number of test cases would increase very quickly. A less complex approach would be a similar study using porous disk type experiments where the flow is purely axial. If the radial variation of the duct parameters is neglected, the amount of data required could be reduced significantly. If actuator disk CFD simulations are used, the additional effort of modeling swirling flow is negligible. However creating a response surface model which includes the radial variation of parameters would still be a somewhat daunting task - particularly if the model is to be applicable to a variety of duct designs.

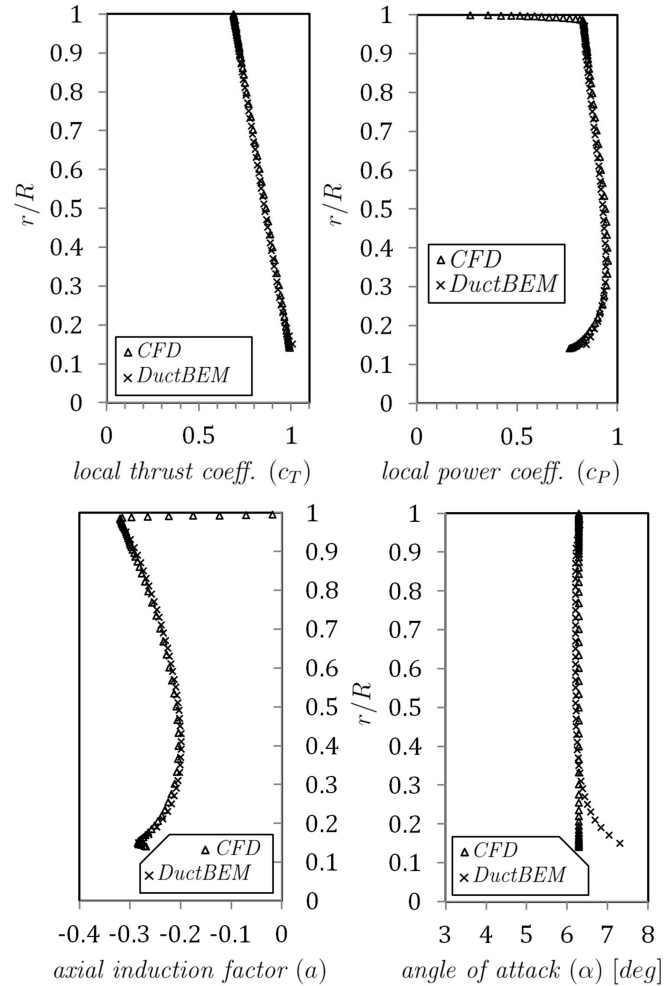


Figure 3.21: Results of the DuctBEM model using the radially varying $c_{b,p}$ and η_{34} extracted for the specific duct and rotor loading, compared to CFD results for the same configuration.

This section presents results of the DuctBEM model where the model parameters were treated as constant with radius (as opposed to the more accurate treatment presented in the previous section). The first case determined the model parameters using area averages across the entire rotor exit plane (station 3) and duct exit plane (station 4) from the simulation defining the optimal turbine performance from section 3.3. This is analogous to a real turbine type experiment because the effect of wake swirl on the diffuser performance is taken into account. The second case determined the model parameters from a simulation which only included axial forcing, thus neglecting the influence of wake swirl on duct performance. The third case used the curve fits for the 1D empirical duct model presented in section 3.2 to determine $c_{p,b}$ and η_{34} based on a parameterized duct geometry and thrust coefficient C_T . Unlike the first two cases, in which the model parameters were calculated for the specific duct and turbine loading, these curve fits have been shown to give reasonable predictions of duct performance over a range of duct designs and C_T , however they are limited in that they

were derived using a dataset from simulations of uniformly-loaded (i.e. $C_{nu}=1$) rotors which did not include tangential forcing terms.

Figures 3.22 and 3.23 show the errors in axial induction, angle of attack, local thrust coefficient and local power coefficient associated with using the simplified models described above. The error is defined as the model output minus the CFD baseline result. The total thrust and power coefficients calculated for each case are summarized in the following.

The total power coefficient C_P was 0.896, 0.919 and 0.843 for cases 1, 2, and 3 respectively, compared to the baseline result of 0.885. The corresponding total thrust coefficients C_T were 0.805, 0.819 and 0.772 respectively, compared to the baseline result of 0.800. The error in axial induction was within ± 0.04 , and the angle of attack was within $\pm 0.5^\circ$ except at the blade root for all cases. The local thrust and power coefficients were within ± 0.1 for all models.

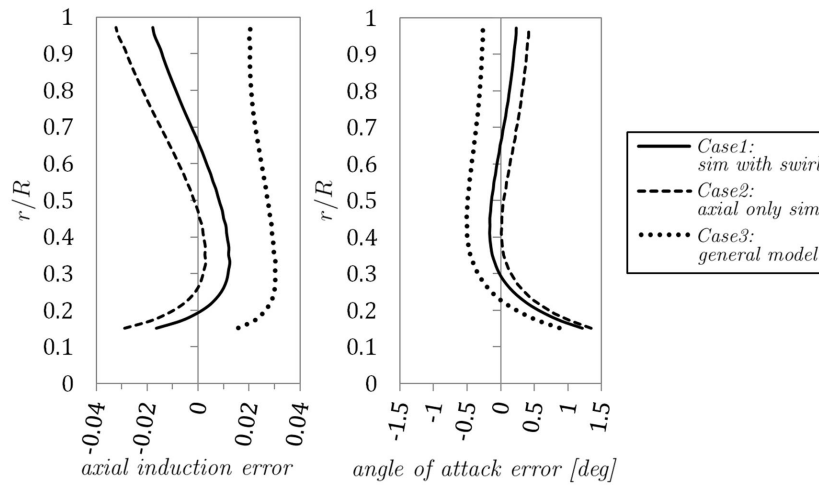


Figure 3.22: Errors in axial induction and angle of attack when using simplified representations of $c_{p,b}$ and η_{34} .

While these errors are significant, the models do produce reasonable results. There is a clear loss of model fidelity as the duct parameters are assumed to be constant with radius (case 1), and when wake swirl is excluded from simulations/experiments used to find the model coefficients (case 2), however this amounts to less than 4% error in the calculated C_P . As expected, the curve fits from section 3.2 (case 3) have lower fidelity than using the parameters determined for this specific duct and operating condition, but the calculated C_P is still within 5% of the baseline result. This shows that reasonable results can be obtained with a parameterized duct model. Such a model is useful for preliminary design work, and more detailed parameterization can be developed as the concept matures and greater accuracy is required for finalized designs.

3.4.3 Optimum Blade

The DuctBEM model was used to define the optimal blade geometry using the strategy described in section 2.3.6. As in the previous section, the results of the present ducted BEM model were

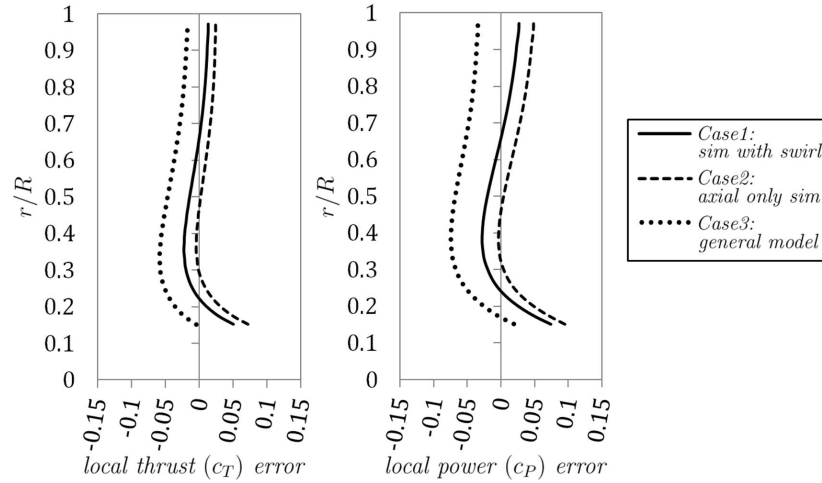


Figure 3.23: Errors in local thrust and power coefficients when using simplified representations of $c_{p,b}$ and η_{34} .

compared to those of the CFD based optimization [46]. The CFD approach predicted an optimum rotor loading with $C_T = 0.800$ and $C_P = 0.885$. While this is used as a baseline for comparison, the method constrained the local thrust coefficient c_t to vary linearly with radius, which may have detracted slightly from the true optimum.

Using the ducted BEM model, the blade was optimized using two sets of duct parameterizations, the first being the radially varying duct coefficients (for the specific rotor loading condition) as described in section 3.4.1, and the second being the set of curve fits from section 3.2. The following discussion refers to the resulting optimum blade geometry, axial induction, thrust and power shown in figure 3.24.

The first parameterization used the radially varying parameters from the specific duct and rotor loading case shown in figure 3.21. This predicted an optimum C_T of 0.868 with $C_P = 0.896$. It is important to note that since this parameterization was developed using a specific rotor loading case, it cannot predict the change in duct coefficients associated with altered rotor loading. In section 3.2 it was found that the diffuser efficiency was nearly constant with changes in rotor loading, but the base pressure coefficient decreased with increasing thrust. Since the algorithm did not account for such variation, it determined a higher optimum thrust loading than the CFD based optimization, which can be observed in the plot of c_T . This thrust loading gave a higher power coefficient towards the blade tips. Note that the contribution of the local thrust and power coefficients towards the global thrust and power increases with the square of the radial position, so increased c_P near the blade tip is much more significant than an equivalent reduction near the root.

The second duct parameterization used the curve fits defined in section 3.2. This gave an optimum C_T of 0.808 and $C_P = 0.846$. Unlike the first duct parameterization, these curve fits account for the effect of C_T on $c_{p,b}$. This explains why the determined optimal thrust loading is very close to the CFD based results. The disadvantage of these curve fits is that they neglect the effects of wake swirl and non-uniform loading on $c_{p,b}$ and η_{34} . It is thought that these effects contribute toward

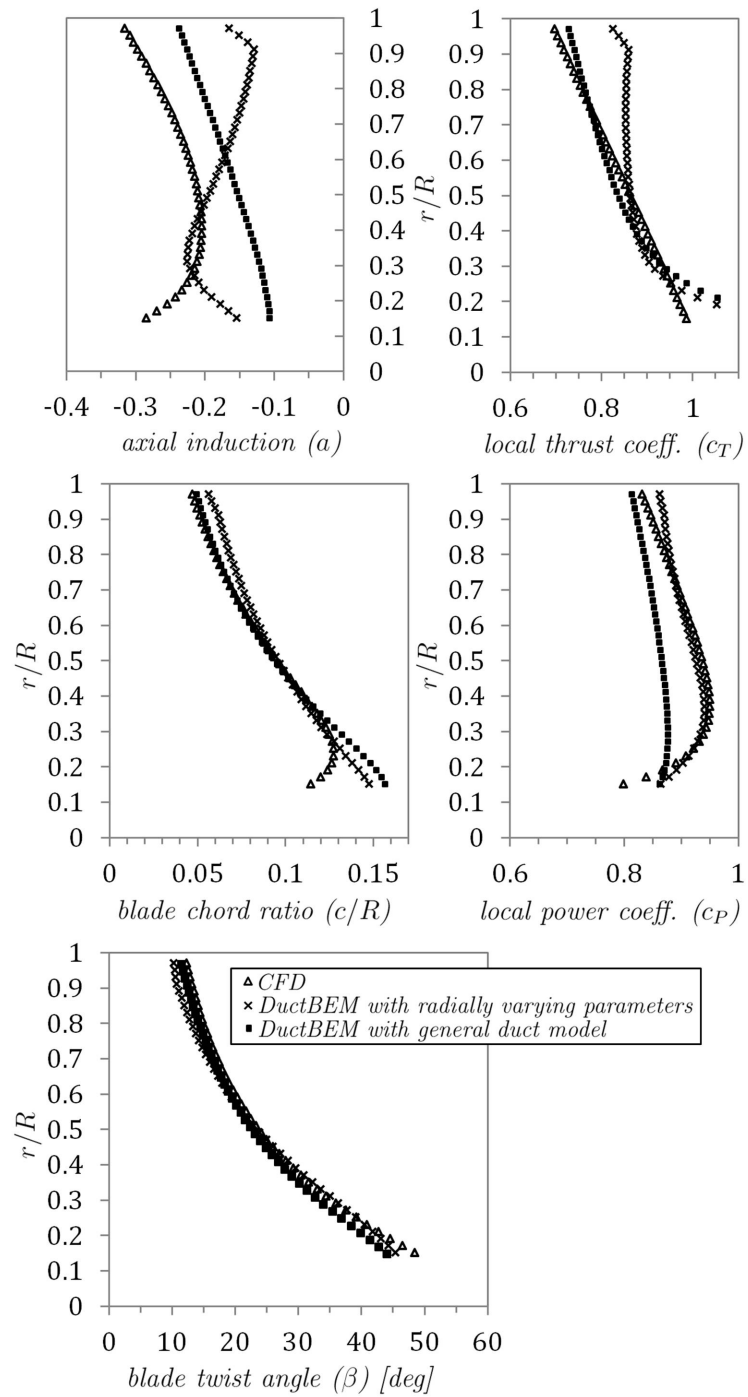


Figure 3.24: Optimal determined blade geometries and performance metrics.

improved duct performance by reducing flow separation through the diffuser. This rationale explains why the determined optimum axial induction, and resulting power coefficient are lower when using the determined curve fits.

In fact, none of the optimization models presented in this thesis are perfect. The CFD based method restricted c_T to vary linearly with radius, which is not likely to represent a true optimum, evidenced by the fact that the BEM based method predicts a non-linear radial variation of local thrust coefficient. The detailed duct parameterization including the radial variation of $c_{p,b}$ and η_{34} neglected the dependence of $c_{p,b}$ on C_T . The curve fits from section 3.2 neglected the influence of wake swirl and non-uniform loading on $c_{p,b}$ and η_{34} . Here, the sensitivity of the ducted BEM method to such assumptions has been shown. The discrepancies between the models are not very large, however CFD simulations presented in section 3.3 indicated that near the optimal loading condition, a small increase in C_T can lead to drastic changes in the flowfield and a large reduction in C_P . This behavior was due to a shift in the location of a region of separated flow from the outer rim of the duct exit towards the duct centerline, which highlights the importance of separation effects in predicting duct performance. Because of such effects, caution is required when using a parameterized duct model for optimization.

3.4.4 Summary

An empirical duct model framework has been merged with blade element momentum theory to produce a useful tool with a range of fidelity levels for the analysis and design of ducted turbines. The physics of the model formulation have been validated for a specific duct geometry and rotor loading case and produced results very similar to actuator disk CFD simulation. In practice, the accuracy of the model depends on the level of detail used in determining the empirical base pressure coefficient $c_{p,b}$ and diffuser efficiency η_{34} parameters. A number of simplified models for these coefficients were compared to illustrate their relative merits and shortcomings. A complete response surface model of how these parameters vary with changing duct geometry and rotor loading could provide a very accurate and robust model valid over a large range of operating conditions.

The DuctBEM model can be used as an alternative to computationally expensive CFD simulation in the design process to determine the optimum blade profile and duct geometry. However, since the model requires parameterization of the duct, a number of physical experiments and/or CFD simulations would still be necessary. The ducted BEM model could also be extended and used to analyze the impact of dynamic inflow and turbulence on blade loading, which would be very computationally expensive using CFD. The DuctBEM model was not used for further work in this thesis because it had not been formulated to account for blockage effects, which were a major part of the remaining work.

3.5 Free Surface Simulation Results

This section presents results of free surface simulations conducted towards understanding the impact of a dynamic free surface on the flow through turbines and the resulting changes to the power production. First, results are presented for a series of CFD simulations which evaluated the sensitivity of the simulation to the downstream location of the dissipation region boundary condition (which is discussed in section 2.5). Then the CFD model’s prediction of the impact of free surface deformation on the power production of turbines is compared to the analytical model by Whelan *et al.* [2] and to the newly developed analytical model given in section 2.5.5. An assessment of the importance of including free surface effects for realistic tidal flows was then carried out.

3.5.1 Sensitivity To the Location of the Dissipation Region

The simulations used a dissipation region as a boundary condition to prevent waves reflecting off of the outlet boundary and back into the domain. It was thought that the simulated free surface and rotor velocity could be sensitive to the downstream location of the beginning of this region. Simulations were run with the dissipation region beginning at $x=10m$, $x=15m$ and $x=20m$ to determine the effect on the turbine performance and free surface profile. In all cases, the RMS momentum residuals converged to 2×10^{-6} and the volume fraction residuals converged to 1×10^{-5} . At this point, several monitor points showed no change to the axial velocity with further iteration, and the solution was thus considered fully converged.

Figure 3.25 shows the dependence of the free surface profile on the starting point of the dissipation region. For the case with $x = 10$ the damping effect of the dissipation region on wave amplitude is evident looking at the 4th, 5th and 6th wave crests. Also note that the inlet surface height is slightly lower than the other cases, implying less total head loss than the other cases (recall that the downstream height is prescribed at $1m$). The cases where $x = 15$ and $x = 20$ give essentially identical profiles for free surface height. This implies that for this particular simulation, starting the dissipation region at $15m$ is sufficient, and keeping a fine mesh beyond this point does not improve the simulation result significantly. The effect of the dissipation boundary location on the power production of the simulated turbine was minimal and is summarized in table 3.3. The calculated C_P varied only in the 3rd decimal place, which was considered negligible.

boundary position (m)	C_P
$10m$	0.8897
$15m$	0.8886
$20m$	0.8862

Table 3.3: Sensitivity of C_P to the downstream location of the dissipation region boundary condition

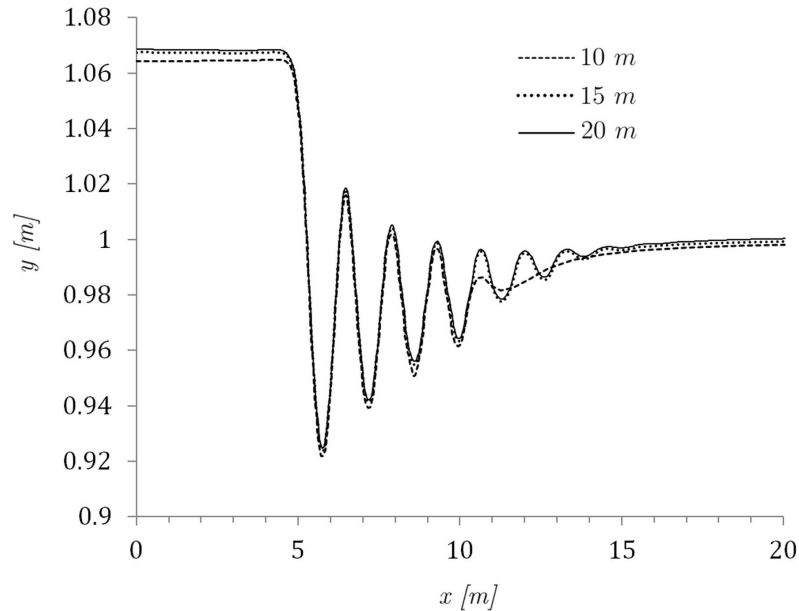


Figure 3.25: The free surface profile predicted from simulations for a range of dissipation region downstream distances $x = \{10, 15, 20\}$

3.5.2 Effect of Free Surface Deformation on Power

The impact of free surface deformation on the calculated turbine power was studied by running two sets of simulations, one with the free surface modeled as described in section 2.5 (which gave a Froude number $Fr \approx 0.3$, and another with the free surface fixed at height of $1m$ ($Fr=0$)¹. In the fixed surface simulations, the domain height was $1m$ and the top boundary condition was a free slip wall. This method modeled the blockage effect of the free surface without modeling its deformation, and such a treatment should be fairly accurate for small free surface deformations.

Simulations were run for values of C_T ranging from 0.5 to 5.0 and the resulting power coefficients are shown in figure 3.26, which also shows results from the two analytical models. The CFD simulations predicted a slight power increase due to the free surface deformation, and are very consistent with the newly developed analytical model (identified as the ‘Shives’ model). The analytical treatment by Whelan *et al.* predicts a much higher increase in power than the CFD results. At this point, neither the analytical nor CFD models have been sufficiently validated with experimental data because suitable data for this purpose have not been found to date.

The deformation of the free surface height predicted by the analytical models is compared to the CFD results for a blockage ratio $B_r = 0.5$ and thrust coefficient $C_T = 3.0$ in figure 3.27. The analytical model by Whelan *et al.* predicts a free surface deformation somewhere in the middle of the valleys and peaks of the resulting wave train, which is consistent with the approach of using the bypass flow velocity u_b in the Bernoulli equation from the wake to the undisturbed upstream

¹Note that $Fr = 0$ implies no free surface deformation corresponding to the fixed surface simulations

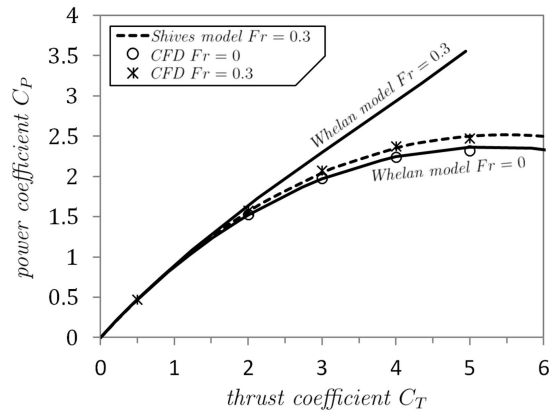


Figure 3.26: Comparison of analytical models for the effect of free surface deformation on turbine power to the CFD results for a range of C_T

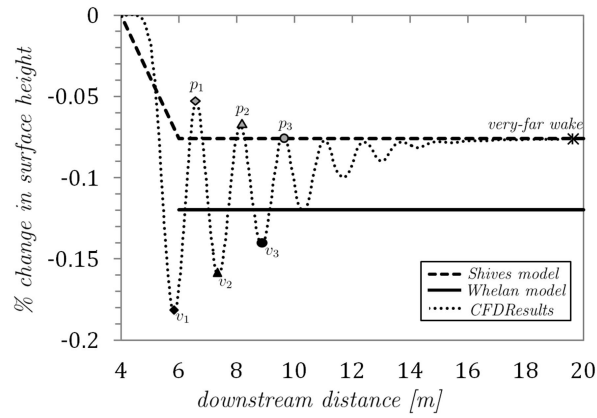


Figure 3.27: Comparison of analytical models for the free surface deformation to the CFD results ($B_r = 0.5$, $C_T = 3.0$)

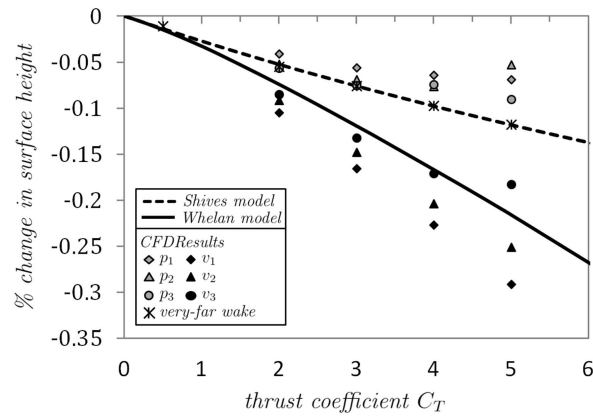


Figure 3.28: Comparison of analytical models for the free surface deformation to the CFD results for a range of C_T

flow to determine the free surface elevation change. The new analytical model predicts the eventual downstream free surface deformation.

Figure 3.28 shows the predicted free surface heights from CFD simulations and the analytical models for the range of tested thrust coefficients. The trends found for the case with $B_r = 0.5$, $C_T = 3.0$ are also seen over the entire range of tested C_T .

3.5.3 Evaluating Free Surface Effects for Real-World Applications

In a real tidal channel, a reasonable blockage ratio might be on the order of 50%. This is due to navigation requirements, clearance requirements between turbines, the requirement that turbines be fully submerged, even at the lowest tide, and limitations on suitable mooring/foundation locations arising from the irregular ocean floor. A shallow channel depth would be approximately $30m$, and a high tidal flow velocity is $5m/s$. Using these figures, the blockage ratio is $B_r = 0.5$, and the Froude number is $F_r = 0.291$. Using these parameters, the newly developed free surface treatment can be used to predict the increased power coefficient for turbines. The maximum C_P for these parameters is 2.50 (a 320% increase from the Betz limit for unbounded flows). If the influence of free surface deformation on the turbine power is neglected, but the blockage effect is still considered, the maximum C_P is 2.37 (a 300% increase from the Betz limit). This scenario represents a maximum reasonable impact of free surface effects. The additional 20% increase when modeling free surface effects is small relative to the 300% increase when just modeling blockage. For very accurate predictions of turbine power potential in a channel, free surface deformations should be considered. However their importance is secondary to that of blockage effects, and they require much more complex simulations to assess accurately. For these reasons, free surface effects were neglected in the case study of turbines in Minas Passage given in section 3.6.

3.5.4 Summary

This section discussed the results of CFD simulations of the interaction of a tidal turbine with a free surface. The model only considered the axial force of the turbine and neglected wake swirl effects, and is thus somewhat idealized. The required location of the dissipation region boundary was established using a sensitivity analysis. It was found that the CFD model predictions of the change in free surface height and the resulting power augmentation were less than those predicted by an analytical model by Whelan *et al.* [2]. The validity of this analytical model was in question, and a new analytical treatment was developed which matched the CFD results very closely. Physical experiments are required to validate both the analytical models and the CFD simulations, however suitable data for this purpose have not been found to date. The predicted impact of free surface deformation on turbine performance was relatively small compared to the impact of blockage effects. For this reason, and due to the increased complexity and computational expense of resolving a dynamic free surface in CFD, free surface effects were not considered in subsequent studies.

3.6 Evaluating Optimal Power Extraction from a Real-World

Tidal Channel

This section describes the results of applying the methodology described in section 2.6 to study the power extraction potential of a fence of turbines in Minas Passage (pictured in figure 3.29) in the Bay of Fundy. This location is of prime interest because it has a very high potential for tidal power generation. Nova Scotia power is considering installing tidal turbines in Minas Passage, and a full scale turbine designed by OpenHydro has been tested there. This study used actuator disk CFD simulations (section 2.4) and the CFD-based optimization algorithm (section 2.6.9) to define the optimal turbine loading and tip speed ratio for a range of turbine blockage ratios (based on the total projected frontal area) in Minas Passage. An analytical model described in section 2.6.4 was used to determine the effect on the turbines on reducing the flow through the channel and the associated reduction of the tidal amplitude in Minas Basin.



Figure 3.29: Satellite image of Minas Passage and surrounding area ©Google (modified to be greyscale, labels added manually)

Optimizations were run for the D1 duct geometry, and for a non-ducted turbine. The D1 duct was chosen because based on the results presented in section 3.1 it had the best extraction efficiency and gave the highest power for a given total device frontal area. It was therefore thought to have the best performance of the considered ducts. One set of optimizations limited the change in tidal amplitude in Minas Basin ΔR to remain less than 5% and another set allowed it to change by up to 100% (unbounded). This section presents results of these optimization runs. First the resulting turbine power and the power dissipated from the flow are shown, followed by an assessment of the extraction efficiency. The increased productivity and therefore improved economics of turbines tuned for blocked flows are then demonstrated. Then the optimal turbine configuration to maximize

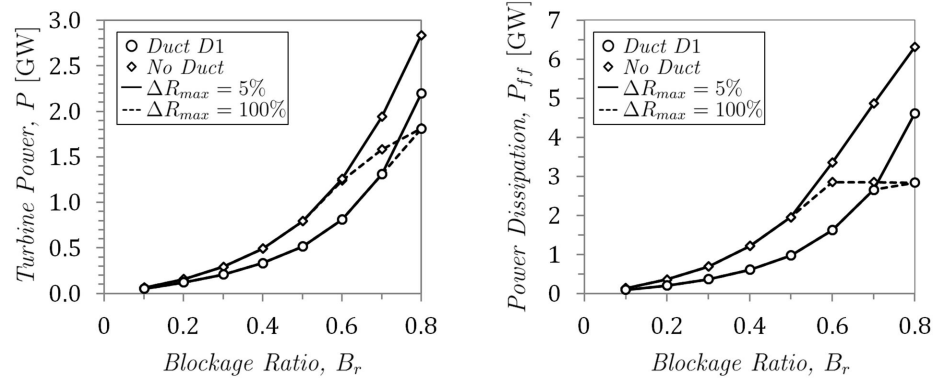


Figure 3.30: Variation of optimal turbine power (left) and resulting total power dissipation (right) with blockage ratio

power production is discussed in terms of the operating thrust coefficient, tip speed ratio and blade geometry. Finally, the flowfield resulting from optimal turbines in blocked flows is discussed.

3.6.1 Turbine Power and Impact on the Tidal Flow

For low blockage ratios, the power production of the turbines was limited by the fact that water could be diverted around the turbines as their thrust coefficient increased (a Betz-like limit) and the constraint to the maximum change to the tidal amplitude did not play a role. For the unconstrained optimizations at higher blockage ratios, the limiting factor became the available driving head between the ocean and Minas Basin. For the constrained optimizations at higher blockage ratios, the 5% constraint to the amplitude change in Minas Basin became the limiting factor. Figure 3.30 shows the variation of turbine power and total power dissipation with blockage ratio for the D1 duct design and the open flow turbine. The impact of the 5% limit is evident in the plot of the power dissipation, where the total dissipation stops increasing beyond a blockage ratio of 0.6 for the open flow turbine. For the D1 turbine, this limit is not hit until a blockage ratio of 0.8. Note that for the constrained optimization, the turbine power continues to increase as the blockage ratio is increased, but with no further increase to the total power dissipation. This was achieved by reducing the thrust coefficient of the turbines (see figure 3.35), and demonstrates that operating turbines at a C_T lower than that for maximum power results in increased extraction efficiency. For a given blockage ratio (and therefore a given total installed frontal area) the open flow turbine always had greater power output and greater total power dissipation than the ducted turbine when both were tuned for maximum power. The impact of power extraction on the tidal amplitude change in Minas Basin is shown in figure 3.31.

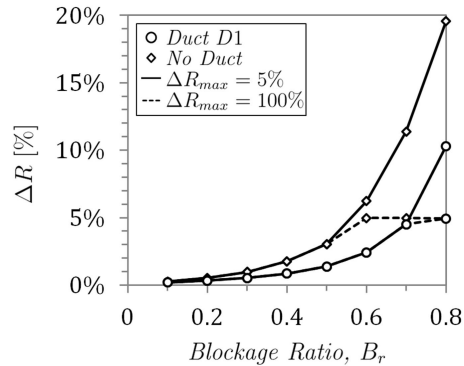


Figure 3.31: Variation of tidal amplitude change in Minas Basin with blockage ratio (when turbines are optimized for maximum power production)

3.6.2 Extraction Efficiency

The extraction efficiency of turbines optimized for maximum power production is plotted in the left-hand plot of figure 3.32. The extraction efficiency can also be visualized in the plot of turbine power vs. total dissipated power in the right-hand plot of figure 3.32. The optimized ducted turbine has a higher extraction efficiency than the optimized non-ducted turbine for a given blockage ratio. However this is somewhat misleading. This trend arises due to choosing to maximize power, instead of extraction efficiency. In fact, the same extraction efficiency as the ducted turbine can be achieved by the non-ducted turbine simply by operating at a reduced thrust coefficient, and this is achieved with a higher power output than the ducted turbine. This is demonstrated for a blockage ratio of 0.6 in figure 3.33. The optimization did not choose such solutions because they come at the cost of reduced power production. This gives evidence that optimally configured non-ducted turbines which are tuned to achieve the same extraction efficiency as optimal ducted turbines will achieve a higher power production. The D1 duct examined in this section had the best performance of all the ducts examined in this thesis, so it seems unlikely that a ducted concept would achieve higher extraction efficiency at the same power output than the conventional non-ducted concept. It is most practical to maximize power production at any given blockage ratio to provide lowest cost of energy, especially considering that tidal turbines need to reduce their cost of energy to become economically competitive with wind power, and even more so to compete with fossil fuel generation.

3.6.3 Economics

The optimization results can be related to the economics of tidal power production by considering that the cost of installing turbines is primarily driven by the total installed frontal area. This assumes that the cost of a ducted turbine would be roughly the same as a non-ducted turbine of equal total frontal area. In reality a ducted turbine would likely require more material and fabrication time than a non-ducted turbine of the same frontal area, and therefore would likely be more expensive. A productivity metric (M_P) is defined to represent the average power generated per square meter

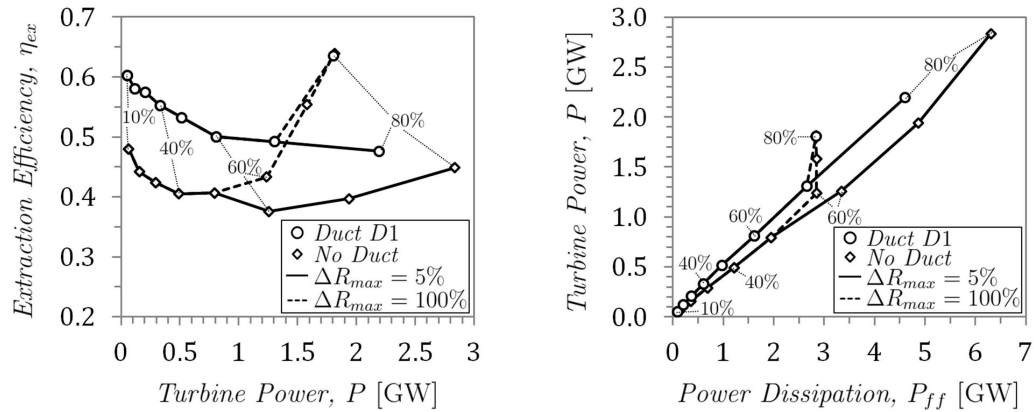


Figure 3.32: Variation of extraction efficiency with optimal turbine power generation (left) and variation of optimal turbine power generation with total power dissipation (right). The labels show the blockage ratio of selected data points.

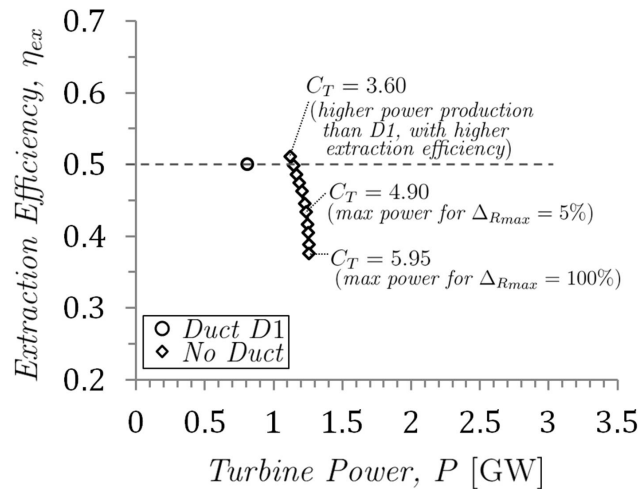


Figure 3.33: Effect of reducing thrust coefficient of non-ducted turbine for a blockage ratio of $B_r = 0.6$. When C_T is reduced such that non-ducted turbine efficiency is equal to that of the ducted turbine, the non-ducted turbine power production is significantly higher than the ducted turbine.

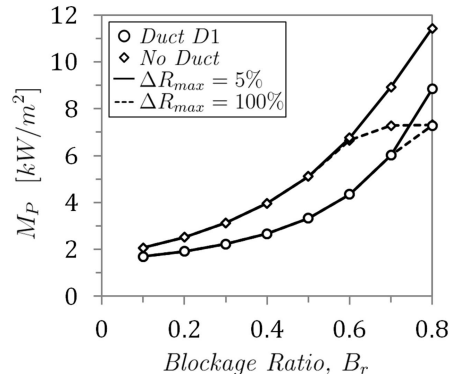


Figure 3.34: Power produced per square meter occupied by turbines plotted against blockage ratio

of installed turbine frontal area.

$$M_P = \frac{P}{A_c B_r} \quad (3.6.1)$$

The productivity metric is clearly important from an economic perspective because its inverse is very closely related to the cost of energy. Of course, turbines operating at a significantly increased thrust coefficient (see figure 3.35) compared to those designed for the unbounded case would have some additional cost which has not been analyzed in this thesis. In figure 3.34 the productivity metric is plotted against the blockage ratio. M_P increases very significantly with increasing blockage ratio, and is always higher for the non-ducted turbine. Because of its superior performance, the following discussion concerns the non-ducted turbine. Extending the trend of M_P to $B_r = 0$ gives an estimated productivity metric of about $1.6[kW/m^2]$ in the limit of isolated turbines. With $B_r = 10\%$, the metric improves by a factor of 1.3. With 50% blockage, the improvement is by a factor of 3.2. With 80% blockage the improvement is by a factor of 4.5 when the limit of 5% change to ΔR is applied, and by a factor of 7 when the tidal amplitude change is unbounded. For turbines arranged in a sparse array, the blockage ratio would likely remain below 10% and the productivity metric would not be nearly as high as with a high blockage ratio. For a given number of installed turbines, the effective blockage ratio will be maximized (and consequently so will be the productivity metric) if the turbines are arranged in a fence configuration, as opposed to multiple rows of sparsely arranged turbines.

3.6.4 Turbine Design

The turbine fence configuration with high blockage ratios requires that turbines operate at a much higher thrust coefficient than those designed for unbounded flows. The thrust coefficient and tip speed ratio which maximize power production are shown in figure 3.35. The optimum thrust coefficient and tip speed ratio both increase with blockage ratio. When the 5% limit to ΔR is enforced, there is a blockage ratio beyond which the thrust coefficient must decrease with increasing blockage, however the tip speed ratio continues to increase as the flow velocity through the turbine continues

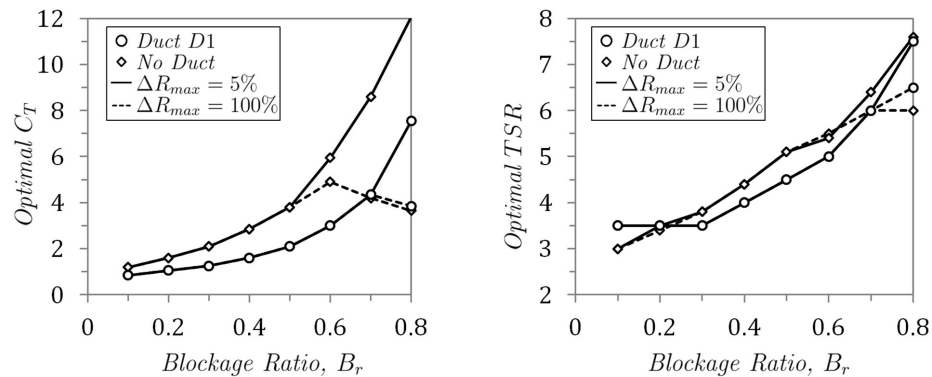


Figure 3.35: Variation of thrust coefficient (left) and tip speed ratio (right) with blockage ratio, for maximum power production

to increase. When this limit is not enforced, the C_T and λ for maximum power continue increasing with B_r . The ducted turbine operates at a significantly reduced thrust coefficient compared to the non-ducted turbine. This may be an advantage because it could potentially reduce the cost of bearings and structures supporting the rotor. However it seems unlikely that this benefit would outweigh the reduced performance and the additional cost of the duct.

Due to the changes to C_T and λ , very different blade profiles are required to maximize power for highly blocked flow conditions than for low blockage ratios. The twist angle must change to maintain an optimal airfoil lift-to-drag ratio and the blade chord depends on the optimal tip speed ratio, thrust coefficient and induction. Figure 3.36 shows the optimal blade chord ratio (c/R) for the non-ducted turbine for each blockage ratio when there is no limit applied to the tidal amplitude change. The left side plot shows the chord ratio, while the right side plot shows the percent change in the chord from the $B_r = 10\%$ case. Note that these blade profiles assume a 6 bladed turbine using the DU91-W2-250 airfoil. Also note that the goal of this section was to identify trends in how the optimal chord and twist distributions change with increasing B_r , and for this purpose the specific blade number and chosen airfoil are not of great importance.

There is an abrupt increase in the chord between the 50% and 60% blockage cases, beyond which the chord is nearly constant with increasing B_r . The required chord varies in proportion to C_T and roughly with the inverse of λ . Observing figure 3.35, it can be seen that below $B_r = 0.5$, C_T and λ increased almost linearly with B_r . At $B_r = 0.6$ the slope of the C_T curve increases, and the slope of the λ curve decreases. This accounts for the sudden increase in the optimal chord distribution.

The optimal blade twist distributions, and the difference in twist from the $B_r = 0.2$ case are shown in figure 3.37. The twist decreases with increasing B_r , and the variation is largest near the blade root. The twist distribution changes gradually as B_r increases from 0.1 to 0.5. There is a transition at $B_r = 0.6$, and the twist is nearly the same for the $B_r = 0.7$ and $B_r = 0.8$ cases.

During this study it was found that the calculated chord distribution was quite sensitive to both the thrust coefficient and the tip-speed ratio. It was also found that near the maximum power condition, the turbine power output was not very sensitive to the tip speed ratio or thrust coefficient. This means that relatively large changes can be made to the chord distribution with only a minor

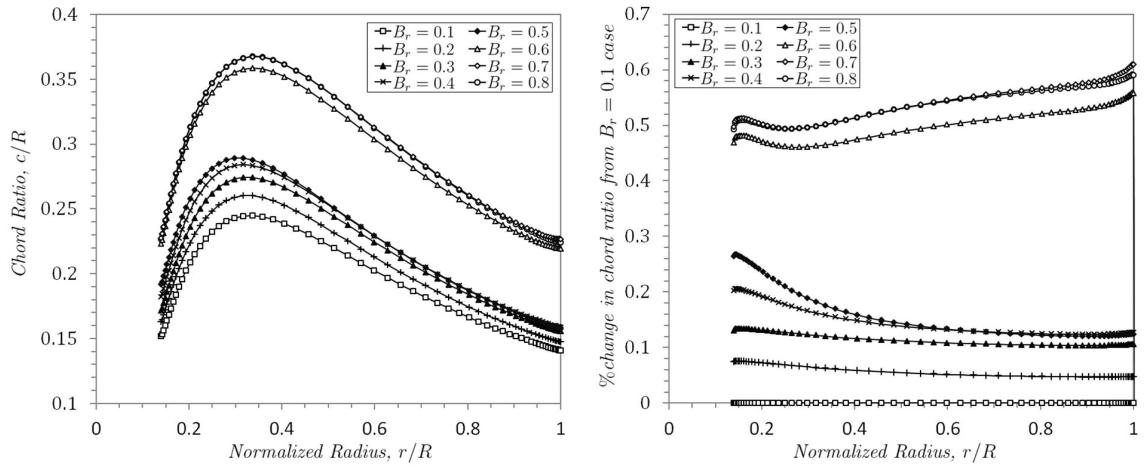


Figure 3.36: Variation of optimal blade chord ratio with increasing blockage (left) and percent change in the chord ratio from the 10% blockage case (right)

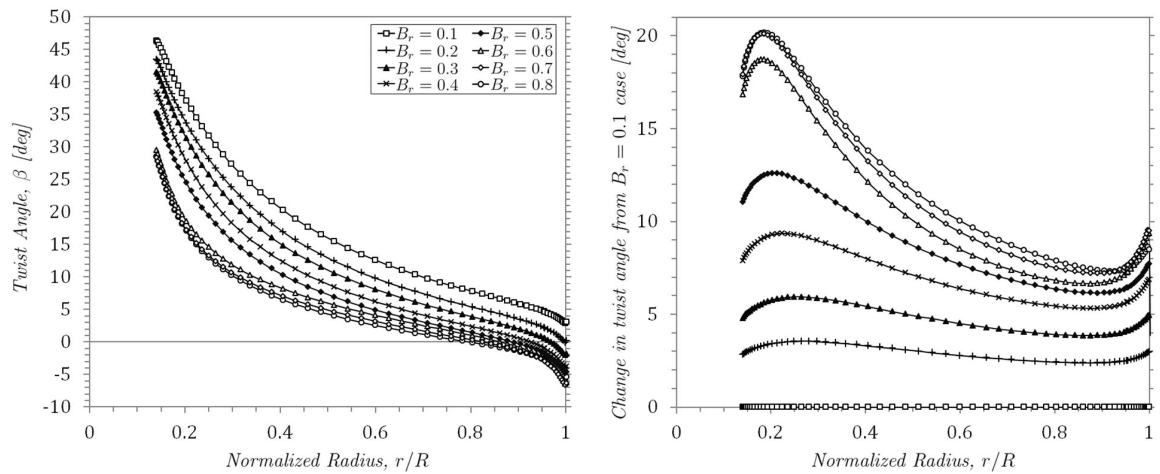


Figure 3.37: Variation of optimal blade twist angle with increasing blockage (left) and change in the twist from the 10% blockage case (right)

impact on the turbine performance. Additionally, the twist profile along the outboard portion of the blade varies by an offset which is nearly constant for blockage ratios ranging from 0.1 to 0.4, and is nearly the same for blockage ratios ranging from 0.6 to 0.8. This means that a blade with chord and twist distributions optimized for the $B_r = 0.3$ case could likely be operated at near-optimal performance over the range ($B_r = 0.1$ to $B_r = 0.5$) by changing the pitch of the entire blade and the turbine rotational speed. The same could be said for a blade optimized for $B_r = 0.7$ operating on blockage ratios ranging from 0.6 to 0.8. Considering this discussion, it is likely feasible to design a single blade that will give near-optimal performance over a wide range of blockage ratios if the turbine rotational speed and the blade pitch can be controlled independently. This would be highly beneficial because a turbine fence would likely be installed incrementally, starting out with a very low blockage ratio and gradually progressing to higher blockage ratios. Designing turbines to give near-optimal performance over a range of B_r would avoid unnecessary performance losses and the additional expense of changing the turbine blades as the tidal fence grows.

3.6.5 Flowfield

The simulated axial velocity near the turbine is shown in figure 3.38 for the maximum power condition for all the blockage ratios. The fast flowing bypass jet is evident in all images, and becomes stronger as the blockage ratio increases. A region of recirculating flow occurs downstream of the turbine actuator disk. This region is almost non-existent with $B_r = 0.1$ but becomes quite large for $B_r = 0.6$. The growth of this recirculation may explain the jump in the calculated chord at $B_r = 0.6$.

Large recirculating flows may have lead to some inaccuracy in the CFD simulation results, because the simulations sought a steady state solution using the SST turbulence model. Large recirculating regions are often unsteady and sometimes require large eddy simulation LES or scale adaptive simulation SAS to accurately resolve. [68] Such methods are orders of magnitude more computationally expensive than the approach taken in this study, making in infeasible to use them for design optimization. Several test cases should be run in the future to assess the error associated with finding a steady state solution to these flows by comparing to large eddy simulations or physical experiments. It is expected that the trends observed in this study are correct, but due to the observed recirculation the results may be somewhat inexact.

The unsteadiness of such recirculating flows is likely to impose significant fatigue loading on the turbine blades and other structures. The severity of the fatigue loading will depend on the magnitude and frequency of these fluctuations. This is an area of research which requires attention to assess the feasibility of tuning turbines with significantly increased rotor loading. Fatigue loads may become a limiting factor in the performance gains possible when taking advantage of blockage effects.

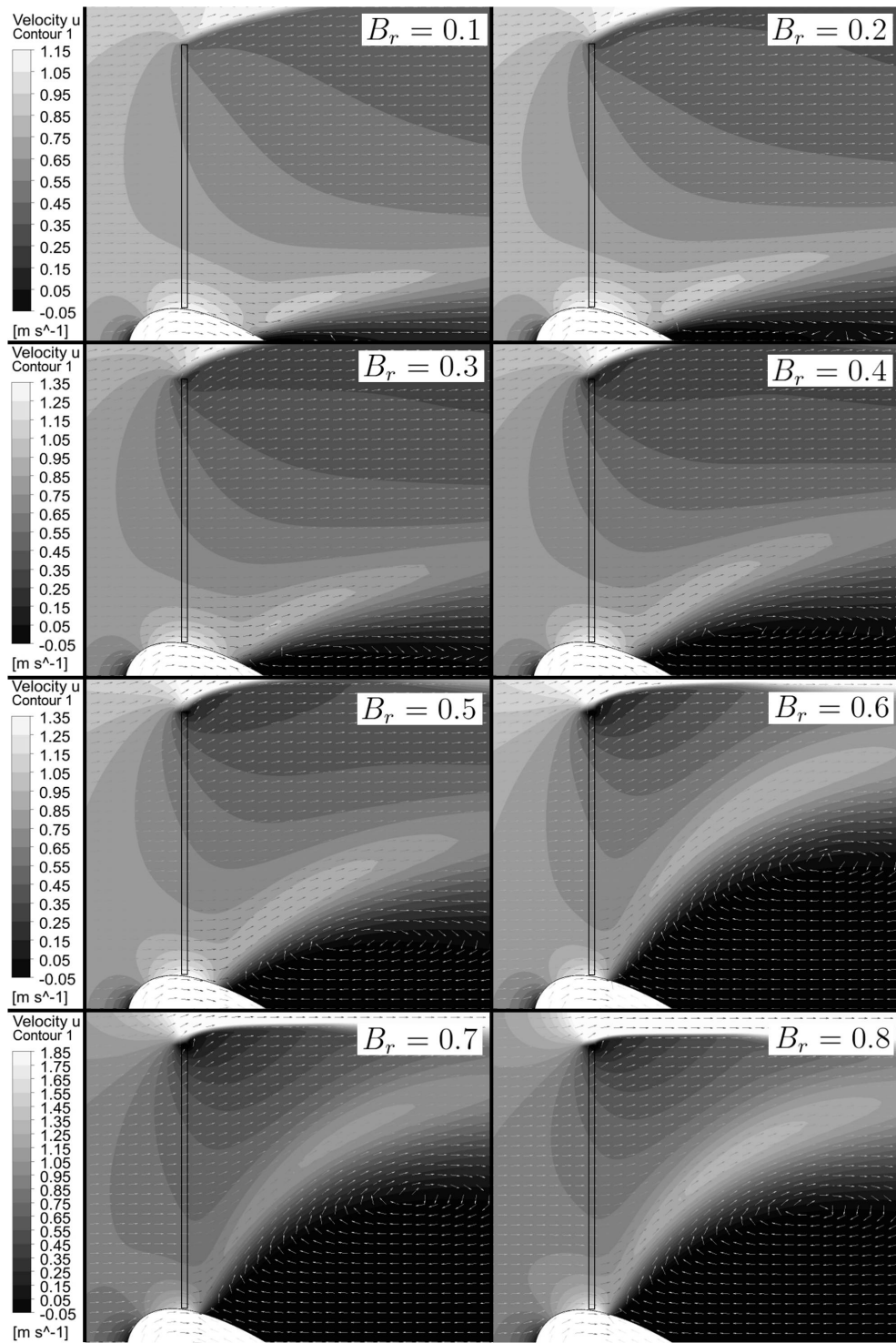


Figure 3.38: Contour plots of the axial velocity near the turbine actuator disk. The actuator disk location is shown by the narrow rectangle, and the assumed turbine hub is clearly visible. Vectors are shown to indicate the flow direction

3.6.6 Summary

The power that can realistically be produced without producing more than 5% change to the tidal amplitude in Minas Basin was found to be approximately 1.81 GW. This requires that turbines occupy 80% of the channel cross sectional area in a single partial fence. It would be possible to reach the limit of 5% amplitude change using multiple partial fences, each with a smaller blockage ratio. This would result in a lower total power and require more turbines, and is therefore not as effective as using a single fence. Karsten *et al.* [6] found that 2.5 GW could be extracted with less than 5% change to the tidal amplitude, but this figure assumed 100% blockage and perfectly ideal turbines (i.e. no losses due to structural drag, duct drag, blade drag, tip loss or wake swirl). The figure 1.8 GW is more realistic because it accounts for such losses and for physical constraints on the achievable blockage ratio. Both analyses have limited accuracy because they assume uniform flow through the channel.

An often cited advantage of using kinetic turbines to extract energy from the tides instead of a barrage-type scheme is the potential for incremental development. In this approach, turbines would be added a few at a time, always developing the most energetic flows. In such an approach, the first turbines to be deployed would need to be optimized for unblocked flow. As more turbines were added, the blockage ratio would increase and the initial turbines would no longer be optimal. Thus it would be advantageous to design turbines which can change their operating tip speed ratio and blade pitch to maintain near-optimal performance as the tidal fence becomes larger. Active pitch control would not necessarily be required for this purpose. The blade attachment design could allow for manual pitch adjustment, which could be done incrementally as the turbine fence grows. The work presented here highlights the requirement for such tuning strategies but also some of the challenges involved. This study suggests that using blade pitch and rotor speed controls, turbine blades can be designed to operate at near-optimal performance over wide ranges of blockage ratios. Of course, if the entire tidal fence could be designed and installed as a single project, the turbines could be optimally configured without as much requirement for in-situ tuning.

This work used a highly idealized channel model with uniform flow. Realistic tidal flows will have significant cross-channel variation, and the most energetic regions will likely be developed first. In reality, there are several factors which will prevent very high blockage ratios. The channel bottom will have highly irregular geometry and may not provide a suitable mooring. Turbines should not be placed in each-other's wakes, or spaced so closely to risk blade collision. Turbines cannot be placed too close to the surface (which varies in height significantly) to prevent the risk of cavitation or worse, blades penetrating the water surface. These factors should be considered in future work, and can likely be best studied using a combination of regional scale oceanographic models to account for cross-channel flow variations, and CFD models for more localized phenomena.

This study found that for the same frontal area, ducted turbines produce less power than non-ducted turbines in blocked flows. It is likely that the expense of including a duct in the turbine design is greater than the expense of simply building longer blades. Due to the additional drag of the duct, ducted turbines have a higher total axial loading than non-ducted turbines that produce the same power, thus requiring stronger moorings. They do, however operate with lower rotor loading,

which could equate to some cost savings in bearings and hub structures. Using a duct also prevents blade tip vortices, which reduce non-ducted turbine power by about 5%, and may cause increased seabed scouring. Ducts may attenuate the flow turbulence encountered by the rotor, reducing blade fatigue loading. They also provide a structure on which a wire mesh or grid can be placed to prevent ingestion of large marine animals. Lastly, they may allow turbines to operate over a longer portion of the tidal cycle by reducing the cut-in speed (the minimum flow speed required for turbines to operate.)² Despite these potential advantages, the concept of using expanding ducts to increase the power production of turbines is unlikely to provide an economic advantage over non-ducted turbines.

The model suggests that flow blockage effects can be exploited to increase the energy production per square meter of installed turbine frontal area by a factor of about three with a blockage ratio of 50%. The possible gains with higher blockage ratios are even greater but may be more limited than the results presented here suggest due to problems with flow recirculation causing fatigue loading. The possible gains in turbine productivity imply a significant economic advantage to the tidal fence type of installation over sparse arrays of turbines.

²The potential to increase the duration of the operational cycle of tidal turbines by decreasing the cut-in speed is an aspect of ducted turbine concepts that warrants further investigation.

Chapter 4

Conclusions

This chapter presents a summary of the work done, answers to the research questions presented in the introduction, and recommendations for future studies.

4.1 Summary of the Work Done

A variety of methods were used to model and optimize turbines, and to account for blockage/free surface effects and for the effect of turbines on reducing the flow through a given tidal channel. Section 2.2 described the well-established blade element momentum (BEM) theory, which was used to evaluate and optimize non-ducted turbine performance in an unbounded domain (i.e. no blockage effect). Section 2.3 described an adaptation of BEM for ducted turbines (DuctBEM), which was developed as a part of this thesis work. The adaptation relied on model parameters which needed to be determined using data from experiments and/or numerical simulations. The accuracy of DuctBEM was evaluated by comparison to more detailed actuator disk CFD simulations with promising results, demonstrating the feasibility of such a model. The DuctBEM model is very fast and could therefore be used for preliminary design studies and could also be extended for dynamic inflows to evaluate fatigue loading on turbine blades. Section 2.4 described the application of the actuator disk CFD methodology to studying ducted and non-ducted turbines. This method is versatile because it represents the duct geometry explicitly, allowing parametric studies of changing geometry to be carried out. It also provides a very simple way to include blockage effects, simply by modifying a single boundary condition. A rotor optimization method using the actuator disk CFD simulations was also described in section 2.4.9. Section 2.5 described methods to model blockage and free surface effects, including previously published and new analytical models and a CFD methodology. Section 2.6 described a methodology to include a 1D channel scale dynamics model (which includes a sinusoidal tidal forcing, drag terms which account for bottom friction and exit separation effects and

terms to account for the increased drag due to turbines) in the turbine rotor optimization employing the actuator disk CFD simulations. This was the first model of its kind, which can define the blade geometry and tip-speed ratio which maximize power production for a chosen blockage ratio and can set a constraint to the acceptable change to tidal amplitude.

These methods were then put to use for a number of case studies. Section 3.1 described a study comparing the power production and extraction efficiency of a non-ducted turbine to turbines using a range of duct geometries for the case of zero blockage, in which the turbine rotors were assumed to be ideal. The non-ducted turbine performance was found using BEM while the ducted performance was found using actuator disk CFD simulations. The study found that based on rotor area, the ducted turbines did produce more power than the non-ducted turbine. However, when normalizing the power using the total device frontal area the non-ducted turbine was superior. The extraction efficiency of the non-ducted turbine was also superior. The applicability of these results was somewhat limited by the assumption of ideal rotors, and a good deal of work was later done towards developing methods to define optimal rotors for ducted and non-ducted turbines. Section 3.2 described the calculation of the model parameters required by DuctBEM from actuator disk CFD results of turbines with ideal rotors using a variety of duct designs. The parameters were curve-fit based on key geometric features of the ducts and the turbine thrust coefficient. The resulting duct performance model was shown to reproduce the CFD predictions of power coefficient well. Section 3.3 described the application of the rotor optimization methodology using actuator disk CFD simulations to two duct geometries. In section 3.4 the DuctBEM model was used to predict the performance and flowfield of one of the optimized designs from section 3.3, with a close match to the CFD results. The DuctBEM model was also used to optimize the rotor design for a ducted turbine, with similar results to the CFD-based optimization algorithm. Section 3.4 also evaluated the error associated with using simplified representations of the duct model parameters.

Section 3.5 described the results of a series of CFD simulations with a blockage ratio of 50% that resolved the influence of free surface effects on ideal turbine performance. It was found that, as predicted by analytical models, free surface deformation led to an increase in turbine power. The previously published analytical model predicted a much greater influence than the simulations, but the newly developed analytical treatment matched the simulations remarkably well. Due to the complexity of modeling free surface effects, and their relative unimportance compared to blockage effects, later studies did not consider them. Section 3.6 applied the combined channel dynamics/rotor optimization technique described in section 2.6 to a case study of a tidal turbine fence in Minas Passage in the Bay of Fundy. The blockage ratio was varied from 10% to 80% and non-ducted turbines and the duct design giving the best performance from previous studies (D1) were considered. This was the most advanced model used in the thesis work, and it accounted for realistic tidal channel dynamics, for blockage effects and for efficiency losses due to drag from support structures, drag on the turbine blades, tip loss (in the case of non-ducted turbines) and duct drag (for ducted turbines). It was found that the non-ducted turbine always had greater power output for a given total installed frontal area. It was also found that non-ducted turbines could be operated to have a higher extraction efficiency and higher power output than ducted turbines. Furthermore, it was found that turbines designed for maximum power production in blocked flows could produce significantly more power

per installed frontal area than those designed for maximum power in sparse arrays.

4.2 Answers to the Research Questions

The primary research question was: *“Is there a real technical advantage to using expanding ducts to increase the power potential of ducted turbines?”*. To address this it was necessary to answer some other questions first.

The question *“What are some valid metrics for comparing the performance of ducted and non-ducted turbines?”* was not trivial. Many researchers [12, 13, 47–49] [15, 50, 51] have presented the power coefficient as a means to make such comparisons. The power coefficient represents the rated power of the turbine for a given flow velocity and rotor diameter. It is felt that this is not a fair metric for comparison because a ducted turbine of equal rotor area to a non-ducted turbine will inevitably use more material, require stronger moorings, and cost more. The cost is likely to be more similar between a ducted turbine, and a non-ducted turbine with a rotor of equal diameter to the duct exit plane. Furthermore, in a tidal channel with a certain cross sectional area, it is the total frontal area of a device which limits the number of turbines which can be placed in a single transect (or tidal fence). For these reasons, it was felt that the power coefficient should be normalized using the device frontal area instead of the rotor area. This represents the useful power production per square meter of the device frontal area, and was used as the first performance metric in this thesis. A second performance metric that was defined was the power extraction efficiency, which is the ratio of useful power production to the rate of energy dissipation from the tidal flow. This is a useful metric because it relates the useful output of the turbines to an important aspect of the environmental impact, since the rate at which energy is dissipated from the flow is the major factor contributing to changes in tidal amplitude and basin flushing.

The question *“How can ducted and non-ducted turbines be optimized?”* was addressed in quite a bit of detail during this thesis work. The work done focused on optimizing the turbine (i.e. blade design and tip speed ratio) for a defined duct geometry. In reality a coupled optimization which determines the duct geometry, blade design and tip speed ratio simultaneously would be ideally suited for such studies. However developing such a tool is quite difficult due to the complexities of ducted turbine flows (particularly the flow separation behavior) which require CFD simulation to predict. As such, a range of duct geometries was employed to observe the impact of changing certain geometric features (namely the inlet contraction ratio, diffuser expansion ratio, and diffuser outlet angles) on performance. Tools were developed to optimize the turbine blade and tip speed ratio for an arbitrary duct based on actuator disk CFD simulation (section 2.4) and based on an extended blade element momentum method (section 2.3) which accounts for the influence of the duct through parameters (the diffuser efficiency and base pressure coefficient) which need to be found through experiments or CFD simulations.

The question *“Since the boundary conditions on tide-driven flows are different than atmospheric flows (i.e. wind), are there major differences in how energy can be extracted and do these factors interact differently with ducted concepts than non-ducted concepts?”* was addressed by creating a

methodology to incorporate an analytical 1D channel dynamics model into a rotor optimization framework as described in section 2.6. This model used a realistic representation of the tidal forcing and accounted for channel blockage effects. It also accounted for the effect of turbines reducing the flow through a given channel and allowed the calculation of the resulting change to the tidal amplitude. This framework was applied to a case study which optimized ducted and non-ducted turbine concepts for maximum power production in Minas Passage. A separate investigation on the effects of free surface deformation (sections 2.5 and 3.5) evaluated the impact on turbine power production and revealed that channel blockage effects are dominant compared to free-surface effects for realistic tidal flows. The impact of free surface deformation is to enhance the power production of turbines by reducing the cross sectional area of the flow via a drop in free surface height. This increases the rotor plane velocity and therefore increases power. Free surface effects were not included in the case study of Minas Passage due to their relative unimportance (compared to blockage effects) and due to the complexity in resolving the free surface deformation in a CFD framework. The case study of Minas Passage revealed that since the boundary conditions on tidal flows are different than atmospheric flows, the limits to power production are significantly different as well. In the case of a tidal flow through a channel, blockage effects allow far greater power production per square meter of installed turbine frontal area. This enhancement was noted for both ducted and non-ducted concepts.

With these questions addressed, it was possible to evaluate the main research question, *“Is there a real technical advantage to using expanding ducts to increase the power potential of ducted turbines?”*. In section 3.1 the performance of turbines using a range of duct geometries was compared to the non-ducted configuration. Ideal rotors were assumed for this study, and the flow was unbounded (i.e. no blockage effects). This study revealed that the maximum extraction efficiency of ducted turbines was bounded by that of the non-ducted turbine. It also showed that the non-ducted turbine had higher power production per square meter of installed frontal area (characterized by C_{P2}). In section 3.6, the performance of turbines optimized for maximum power production was found for a realistic tidal channel (Minas Passage) for a range of blockage ratios. The duct design which gave the best performance in the unbounded case (D1) was compared to a non-ducted turbine in this study. It was found that at all blockage ratios, the non-ducted turbine had higher power production per installed frontal area. It was also demonstrated that the non-ducted turbine could operate at equal efficiency, and higher power than the ducted turbine. Of course these results were for a particular duct design, however in all studies performed during this thesis it was noticed that progressively more aggressive duct profiles (i.e. those which were designed to provide the largest mass flow increase for a given rotor area) gave progressively poorer performance in terms of the chosen performance metrics. Based on this trend, it seems clear that the best duct is one which has the least influence on the flow, (i.e. no duct at all). Additionally, the ducts used in this study were uni-directional, which are expected to have significantly better performance than bi-directional ducts which will certainly have a reduced inlet efficiency. In tidal power applications, bi-directional ducts seem to be the preferred design concept because they do not require a yawing mechanism to operate in both ebb and flood tides. Thus, the conclusion is that using expanding ducts to increase the power potential of ducted turbines offers no technical advantage from a flow-physics perspective.

It is important to note that ducts may offer practical engineering advantages which have not been explicitly addressed in this thesis work. It could be that a duct with a very mild expansion ratio which exhibits no flow separation could produce better performance than a non-ducted turbine by preventing tip vortices from forming. This would offer at best a 5% enhancement to the power produced per square meter of installed frontal area. (Equal to the impact of tip loss on non-ducted turbines.) Preventing tip vortices may reduce seabed scouring as well. An optimized ducted turbine will operate at a reduced rotor loading compared to a non-ducted turbine. This may offer some savings by reducing structural requirements on bearings and/or the hub assembly. Ducts may also attenuate the flow turbulence encountered by the rotor, reducing blade fatigue loads. They may also redirect off axis flows to become more aligned with the turbine rotor, which could be beneficial in locations where the flow is not exactly bi-directional. They could also provide a structure on which a grate could be installed to prevent large objects and marine animals from entering the turbine. Also, ducts may reduce the cut-in speed of turbines, allowing them to operate over a longer portion of the tidal cycle. These practical advantages may prove valuable enough to encourage the proliferation of ducted concepts. However, the concept of using expanding ducts to augment turbine power production has been shown to be less effective than simply extending the turbine blades to the same diameter of the proposed duct exit.

The final research question was, “*What is the best strategy to maximize power production of turbines, while minimizing the cost and environmental impact?*” While this thesis has not addressed this question sufficiently to provide a definitive answer, it seems that optimizing turbines to operate in blocked flows, using a tidal fence arrangement, offers potential for the most power production with the least number of turbines (i.e. least cost). The benefit of this increases greatly with the blockage ratio. For example, a tidal fence with a blockage ratio of 50% could give three times more power per installed square meter of installed turbine area than turbines arranged in a sparse array. This result has been found using a simple 1D channel model that assumes uniform flow. In reality, the flow through a given tidal channel varies with depth and across the channel width. To maximize the power production of turbines in real channels, more advanced models than those presented in this thesis are required.

4.3 Recommendations for Future Studies

Based on the findings of this thesis work, and considering some important aspects which it did not address a number of recommendations can be made.

First, it is recommended to not use expanding ducts to try to improve the power production of tidal turbines. A ducted rotor will produce less power, and likely cost more than a non-ducted rotor of equal diameter to the duct exit. Note that it is possible to follow this recommendation while still using ducts to take advantage of their potential other benefits described above, however in doing so the duct would have a very small expansion ratio and be designed to avoid any flow separation. Such a duct could be much shorter than those studied in this thesis, requiring much less material and producing much less drag.

Second, due to the very large potential benefits of exploiting blockage effects to increase turbine power, further research into this possibility is strongly encouraged. The feasibility of such an approach needs to be studied using much more detailed tidal channel models which include spatial and temporal variations in the flow velocity. This presents a challenge because numerical channel flow simulations use grid spacings on the order of kilometers or at best tens of meters [6], while the grid spacings required to resolve the flow around turbines are on the order of meters or centimeters. Thus, there is a requirement to either develop accurate sub-grid scale representations of turbines or to develop computationally efficient nested domains to resolve the flow around turbines or to use local mesh refinement in the regional scale models to obtain sufficient resolution to model turbines directly.

Third, this thesis work often identified flows with large regions of recirculating flow. Such flows are difficult to resolve accurately using steady-state CFD simulations and may produce large dynamic fluctuations in the velocity encountered by turbine blades, leading to damaging fatigue loads. Additionally, the turbulent fluctuations naturally present in tidal flows may lead to similar fatigue loading, and CFD methods that include such dynamic inflow conditions should be pursued. There is a requirement to analyze dynamic flow behavior in much more detail than covered in this thesis work because it will likely have a significant impact on turbine design. This can best be achieved using large eddy simulation or scale adaptive simulation methods [68], which are much more computationally expensive than the Reynolds averaged approach taken here, and will therefore require more computational resources than a single PC. Working towards this goal, an actuator-line CFD approach [85, 86] has been pursued separately from this thesis work, both to provide an assessment of discrete blade effects for tidal turbines, and to later extend to modeling dynamic flows.

By pursuing turbine designs which exploit blockage effects in tidal channels, tidal turbines can become much more economically competitive with fossil fuel based power generation. Studying dynamic blade loading is important in this context, because such turbines will operate with higher rotor loading than the traditional concept optimized for the scenario of sparse turbine arrays. Accurate modeling of dynamic flows and their interaction with turbine blades will improve predictions of fatigue and eventually lead to longer service lifetimes of turbines. Making tidal turbines produce more energy and improving their serviceable lifetime could certainly lead to the widespread proliferation of this carbon-free, predictable energy generation technology.

Bibliography

- [1] M. O. L. Hansen, N. N. Sørensen, and R. G. J. Flay, “Effect of placing a diffuser around a wind turbine,” *Wind Energy*, vol. 3, pp. 207–213, 2000. [viii](#), [3](#), [4](#), [15](#), [43](#), [48](#), [49](#), [84](#)
- [2] J. I. Whelan, J. M. R. Graham, and J. Peir, “A free-surface and blockage correction for tidal turbines,” *J. Fluid Mech*, vol. 624, pp. 281–291, 2009. [viii](#), [7](#), [20](#), [51](#), [52](#), [53](#), [55](#), [57](#), [69](#), [100](#), [103](#)
- [3] R. H. Charlier, “Forty candles for the rance river tpp tides provide renewable and sustainable power generation,” *Renewable and Sustainable Energy Reviews*, vol. 11, pp. 2032–2057, 2007. [1](#)
- [4] L. Blunden and A. Bahaj, “Initial evaluation of tidal stream energy resources at portland bill, uk,” *Renewable Energy*, vol. 31, pp. 121–132, 2006. [1](#)
- [5] I. Bryden and G. T. Melville, “Choosing and evaluating sites for tidal current development,” *Proc. Instn Mech. Engrs Vol. 218 Part A: J. Power and Energy*, vol. 218, pp. 567–577, 2004. [6](#)
- [6] R. H. Karsten, J. M. McMillan, M. J. Lickley, and R. D. Haynes, “Assessment of tidal current energy in the minas passage, bay of fundy,” *Proc. IMechE Vol. 222 Part A: J. Power and Energy*, vol. 222, pp. 493–507, 2008. [6](#), [59](#), [60](#), [61](#), [62](#), [63](#), [64](#), [113](#), [120](#)
- [7] F. O. Rourke, F. Boyle, and A. Reynolds, “Tidal energy update 2009,” *Applied Energy*, vol. xxx, pp. xxxx–xxxx, 2009. in press. [1](#)
- [8] N. Park, “Sihwa tidal power plant: a success of environment and energy policy in korea.” Korea University, Online: http://www.eer.wustl.edu/McDonnellMayWorkshop/Presentation_files/Saturday/Saturday/Park.pdf, 2007. [2](#)
- [9] R. Pelc and R. M. Fujita, “Renewable energy from the ocean,” *Marine Policy*, vol. 26, pp. 471–479, 2002. [2](#), [6](#)
- [10] G. M. Lilley and W. J. Rainbird, “Rep. 102: A preliminary report on the design and performance of ducted windmills,” tech. rep., College of Aeronautics, Cranfield, 1956. available as Tech. Rep. C/T 119, The Electrical Research Association, Leatherhead, England (1957). [3](#), [29](#)
- [11] K. M. Foreman, B. Gilbert, and R. A. Oman, “Diffuser augmentation of wind turbines,” *Solar Energy*, vol. 20, pp. 305–311, 1978. [3](#), [29](#), [32](#)

- [12] B. L. Gilbert, R. A. Oman, and K. M. Foreman, “Fluid dynamics of diffuser augmented wind turbines,” *Journal of Energy*, vol. 2, pp. 368 – 374, 1978. [3](#), [16](#), [32](#), [117](#)
- [13] B. Gilbert and K. Foreman, “Experimental demonstration of diffuser augmented wind turbines,” *Journal of Energy*, vol. 3, pp. 235 – 240, 1979. [3](#), [16](#), [32](#), [84](#), [117](#)
- [14] D. G. Phillips, R. G. J. Flay, and T. A. Nash, “Aerodynamic analysis and monitoring of the Vortec 7 diffuser-augmented wind turbine,” *IPENZ Transactions*, vol. 26, no. 1, pp. 13–19, 1999. [3](#)
- [15] D. G. Phillips, P. J. Richards, and R. G. J. Flay, “Cfd modelling and the development of the diffuser augmented wind turbine,” *Wind and Structures*, vol. 5, pp. 267–276, 2002. [3](#), [16](#), [117](#)
- [16] C. F. Fleming, S. C. McIntosh, and R. H. Willden, “Design and analysis of a bi-directional ducted tidal turbine,” in *Proceedings of the 9th European Wave and Tidal Energy Conference Series*, 2011. [4](#), [8](#), [16](#), [36](#), [67](#), [74](#), [90](#)
- [17] W. Batten, A. Bahaj, A. Molland, and J. Chaplin, “The prediction of the hydrodynamic performance of marine current turbines,” *Renewable Energy*, vol. 33, pp. 1085–1096, 2008. [5](#), [6](#), [7](#), [20](#)
- [18] A. Muñoz, “Once in a lifetime coatings anticorrosion and underwater maintenance solutions,” in *3rd International Conference on Ocean Energy, 6 October, Bilbao, PS4-6.*, 2010. [6](#)
- [19] J. Thomson, B. Polagye, M. Richmond, and V. Durgesh, “Quantifying turbulence for tidal power application,” in *Oceans 2010, Seattle, WA, September 20-23.*, 2010. [6](#), [43](#)
- [20] S. Gant and T. Stallard, “Modelling a tidal turbine in unsteady flow,” in *Proceedings of the Eighteenth (2008) International Offshore and Polar Engineering Conference, Vancouver BC, Canada*, July 6-11, 2008. [6](#)
- [21] R. Karsten, A. Swan, and J. Culina, “Assessment of arrays of in-stream tidal turbines in the bay of fundy,” in *The 9th European Wave and Tidal Energy Conference*, 2011. [6](#), [59](#)
- [22] I. Jones, C. Staples, A. Wells, R. McSherry, J. Grimwade, and A. Mateus, “Numerical modelling of high energy tidal regions using three-dimensional cfd,” in *Proceedings of the 9th European Wave and Tidal Energy Conference Series*, 2011. [6](#)
- [23] I. G. Bryden, S. J. Couch, A. Owen, and G. Melville, “Tidal current resource assessment,” *Proc. IMechE Vol. 221 Part A: J. Power and Energy*, vol. 221, pp. 125–135, 2007. [6](#), [59](#)
- [24] C. Garrett and P. Cummins, “Limits to tidal current power,” *Renewable Energy*, vol. 33, pp. 2485–2490, 2008. [6](#), [59](#), [61](#)
- [25] R. Vennell, “Tuning turbines in a tidal channel,” *J. Fluid Mech.*, vol. 663, pp. 253–267, 2010. [7](#), [59](#), [61](#), [65](#)

- [26] C. Garrett and P. Cummins, “The efficiency of a turbine in a tidal channel,” *Journal of Fluid Mechanics*, vol. 588, pp. 243–251, 2007. [7](#), [57](#), [59](#), [61](#), [64](#), [65](#)
- [27] X. Sun, J. Chick, and I. Bryden, “Laboratory-scale simulation of energy extraction from tidal currents,” *Renewable Energy*, vol. 33, pp. 1267–1274, 2008. [7](#), [8](#), [36](#)
- [28] R. Nicholls-Lee, S.R.Turnock, and S.W.Boyd, “Performance prediction of a free stream tidal turbine with composite bend-twist coupled blades,” in *2nd International Conference on Ocean Energy (ICOE 2008)*, (Brest, France), 15th–17th October 2008. [7](#), [20](#)
- [29] W. Batten, A. Bahaj, A. Molland, and J. Chaplin, “Experimentally validated numerical method for the hydrodynamic design of horizontal axis tidal turbines,” *Ocean Engineering*, vol. 34, pp. 1013–1020, 2007.
- [30] J. A. Clarke, G. Connor, A. D. Grant, and C. M. Johnstone, “Design and testing of a contra-rotating tidal current turbine,” *Proc. IMechE Vol. 221 Part A: J. Power and Energy*, vol. 221, pp. 171–179, 2007.
- [31] P. L. Fraenkel, “Marine current turbines: pioneering the development of marine kinetic energy converters,” *Proc. IMechE Vol. 221 Part A: J. Power and Energy*, vol. 221, pp. 159–169, 2007.
- [32] L. Myers and A. Bahaj, “Simulated electrical power potential harnessed by marine current turbine arrays in the alderney race,” *Renewable Energy*, vol. 30, pp. 1713–1731, 2005. [7](#), [20](#)
- [33] L. Wang, L. Zhang, and N. Zeng, “A potential flow 2-d vortex panel model: Applications to vertical axis straight blade tidal turbine,” *Energy Conversion and Management*, vol. 48, pp. 454–461, 2007. [8](#)
- [34] D. Egarr, T. ODoherty, S. Morris, and R. Ayre, “Feasibility study using computational fluid dynamics for the use of a turbine for extracting energy from the tide,” in *15th Australasian Fluid Mechanics Conference*, (The University of Sydney, Sydney, Australia), December 2004. [8](#)
- [35] A. Mason-Jones, T. ODoherty, D. M. ODoherty, P. S. Evans, and C. F. Wooldridge, “Characterisation of a hatt using cfd and adcp site data,” tech. rep., World Renewable Energy Congress, 2008. Editor: A. Sayigh. [8](#)
- [36] M. Harrison, W. Batten, L. Myers, and A. Bahaj, “Comparison between cfd simulations and experiments for predicting the far wake of horizontal axis tidal turbines,” *IET Renew. Power Gener.*, vol. 4, pp. 613–627, 2010. [8](#), [36](#)
- [37] R. McSherry, J. Grimwade, I. Jones, S. Mathias, A. Wells, and A. Mateus, “3d cfd modelling of tidal turbine performance with validation against laboratory experiments,” in *Proceedings of the 9th European Wave and Tidal Energy Conference Series*, 2011.
- [38] C. S. Belloni and R. H. Willden, “Flow field and performance analysis of bidirectional and open-centre ducted tidal turbines,” in *Proceedings of the 9th European Wave and Tidal Energy Conference Series*, 2011. [8](#)

- [39] R. Mikkelsen, *Actuator Disc Methods Applied to Wind Turbines*. PhD thesis, University of Denmark, 2003. [8](#), [20](#), [36](#), [41](#)
- [40] J. N. Sørensen and W. Z. Shen, “Numerical modeling of wind turbine wakes,” *Journal of Fluids Engineering*, vol. 124, pp. 393–399, 2002. [8](#), [67](#)
- [41] S. Ivanell, J. N. Sørensen, R. Mikkelsen, and D. Henningson, “Analysis of numerically generated wake structures,” *Wind Energy*, vol. 12, pp. 63–80, 2009. [8](#)
- [42] M. Shives and C. Crawford, “Overall efficiency of ducted tidal current turbines,” in *Proceedings of the OCEANS 2010 MTS/IEEE SEATTLE Conference & Exhibition*, (Seattle, WA.), September 2010. [9](#)
- [43] M. Shives and C. Crawford, “Computational analysis of ducted turbine performance,” in *3rd International Conference on Ocean Energy, 6 October, Bilbao*, 2010. [9](#)
- [44] M. Shives and C. Crawford, “Developing an empirical model for ducted tidal turbine performance using numerical simulation results,” *Proceedings of the Institution of Mechanical Engineers, Part A: Journal of Power and Energy*, 2011. Published Online Oct. 2011. [9](#), [38](#)
- [45] M. Shives and C. Crawford, “Merging blade element momentum theory (bem) with an empirical ducted turbine model,” *Proc. Instn Mech. Engrs Part A: J. Power and Energy*, 2011. Submitted Sep 2011, Submission: JPE1402. [9](#)
- [46] M. Shives and C. Crawford, “Ducted turbine blade optimization using numerical simulation,” in *Proceedings of the 21st International Offshore (Ocean) and Polar Engineering Conference, Maui Hawaii*, June 19-24 2011. [9](#), [97](#)
- [47] B. L. Gilbert and K. M. Foreman, “Experiments with a diffuser augmented model wind turbine,” *Transactions of the ASME: Journal of Energy Resources Technology*, vol. 105, pp. 47–53, 1983. [16](#), [84](#), [117](#)
- [48] C. J. Lawn, “Optimization of the power output from ducted turbines,” *Proc. Instn Mech. Engrs Vol. 217 Part A: J. Power and Energy*, vol. 217, pp. 107–117, 2003. [29](#), [30](#), [31](#), [32](#)
- [49] G. J. van Bussel, “The science of making more torque from wind: Diffuser experiments and theory revisited,” *Journal of Physics: Conference Series*, vol. 75, pp. 1–12, 2007. [16](#), [29](#), [117](#)
- [50] T. Setoguchi, N. Shiomi, and K. Kaneko, “Development of two-way diffuser for fluid energy conversion system,” *Renewable Energy*, vol. 29, pp. 1757–1771, 2004. [85](#), [117](#)
- [51] K. Abe, M. Nishida, A. Sakurai, Y. Ohya, H. Kihara, E. Wada, and K. Sato, “Experimental and numerical investigations of flow fields behind a small wind turbine with a flanged diffuser,” *Journal of Wind Engineering and Industrial Aerodynamics*, vol. 93, pp. 951–970, 2005. [16](#), [85](#), [117](#)

- [52] M. Hansen, J. Sørensen, S. Voutsinas, N. Srensen, and H. Madsen, “State of the art in wind turbine aerodynamics and aeroelasticity,” *Progress in Aerospace Sciences*, vol. 42, pp. 285–330, 2006. [20](#), [36](#)
- [53] F. W. Lanchester, “A contribution to the theory of propulsion and the screw propeller,” *Transactions of the Institution of Naval Architects*, p. 330, Mar. 25 1915. [20](#)
- [54] T. Burton, D. Sharpe, N. Jenkins, and E. Bossanyi, *Wind Energy Handbook*. John Wiley & Sons Ltd., 2001. [20](#), [23](#), [26](#), [29](#), [48](#), [67](#), [71](#), [87](#)
- [55] G. H. *Aerodynamic Theory*, ch. Airplane propellers, pp. 169–360. Dover: New York, 1963. [26](#)
- [56] P. Jamieson, “Generalized limits for energy extraction in a linear constant velocity flow field,” *Wind Energy*, vol. 11, pp. 445–457, 2008. [29](#)
- [57] R. Singh and S. Dinavahi, “Shape optimization of a ducted rotor system for aerodynamic performance,” in *49th AIAA Aerospace Sciences Meeting including the New Horizons Forum and Aerospace Exposition*, (Orlando, Florida), 4 - 7 January 2011. [36](#)
- [58] P. Réthoré, N. Sørensen, and F. Zahle, “Validation of an actuator disc model,” *EWEC, Warsaw*, 2010. [36](#)
- [59] J. T. Conway, “Analytical solutions for the actuator disk with variable radial distribution of load,” *J. Fluid Mech.*, vol. 297, pp. 327–355, 1995. [36](#)
- [60] W. Z. Shen, J. N. Sørensen, and R. Mikkelsen, “Tip loss correction for actuator/navierstokes computations,” *Journal of Solar Energy Engineering*, vol. 127, pp. 209–213, 2005. [36](#), [67](#)
- [61] ANSYS, “Ansys cfd, release 12.0,” tech. rep., 2009. CFX software documentation. [37](#), [54](#)
- [62] G. Corten, “Heat generation by a wind turbine,” in *IEA symposium on the aerodynamics of wind turbines*, vol. 14, NREL, Dec 4-5 2000. [38](#), [66](#), [70](#)
- [63] H. Versteeg and W. Malalasekera, *An Introduction to Computational Fluid Dynamics: The Finite Volume Method*. Pearson Education Limited, 2 ed., 2007. ISBN: 978-0-13-127498-3. [38](#)
- [64] F. R. Menter, “Two-equation eddy-viscosity turbulence models for engineering applications,” *AIAA Journal*, vol. 32, pp. 1598–1605, 1994. [38](#), [39](#)
- [65] F. Menter, “A comparison of some recent eddy viscosity turbulence models,” *Journal of Fluids Engineering*, vol. 118, pp. 514–519, 1996. [38](#)
- [66] J. Bardina, P. Huang, and T. Coakley, “Turbulence modeling validation testing and development,” Technical Memorandum 110446, NASA, April 1997.
- [67] M. I. Yaras and A. D. Grosvenor, “Evaluation of one- and two-equation low-re turbulence models. part i axisymmetric separating and swirling flows,” *International Journal For Numerical Methods In Fluids*, vol. 42, pp. 1293–1319, 2003.

- [68] F. R. Menter, “Review of the shear-stress transport turbulence model experience from an industrial perspective,” *International Journal of Computational Fluid Dynamics*, vol. 23, no. 4, pp. 305–316, 2009. [38](#), [39](#), [111](#), [120](#)
- [69] B. Launder and D. Spalding, “The numerical computation of turbulent flows,” *Comp Meth Appl Mech Eng*, vol. 3, pp. 269–289, 1974. [39](#)
- [70] D. Wilcox, “Multiscale model for turbulent flows,” in *AIAA 24th Aerospace Sciences Meeting. American Institute of Aeronautics and Astronautics*, 1986. [39](#)
- [71] I. Celik, U. Ghia, P. Roache, C. Freitas, H. Coleman, and P. Raad, “Procedure for estimation and reporting of uncertainty due to discretization in cfd applications,” *Journal of Fluids Engineering*, vol. 130, 2008. [46](#)
- [72] ANSYS, “Automatic near-wall treatment for omega-based models, ansys cfx release 12 documentation,” tech. rep., ANSYS, 2009. [46](#)
- [73] J. N. Sørensen, W. Z. Shen, and R. Mikkelsen, “Wall correction model for wind tunnels with open test section,” *AIAA JOURNAL*, vol. 44, pp. 1890–1894, 2006. [51](#), [57](#), [61](#)
- [74] G. Gretton, I. Bryden, S. Couch, and D. Ingram, “The cfd simulation of a lifting hydrofoil in close proximity to a free surface,” in *Proceedings of the ASME 2010 29th International Conference on Ocean, Offshore and Arctic Engineering OMAE2010 June 6-11, Shanghai, China*, 2010. [52](#), [53](#)
- [75] G. Sutherland, M. Foreman, and C. Garrett, “Tidal current energy assessment for johnstone strait, vancouver island,” *Proc. IMechE Vol. 221 Part A: J. Power and Energy*, vol. 221, pp. 147–157, 2007. [59](#)
- [76] B. Polagye, P. Malte, M. Kawase, and D. Durran, “Effect of large-scale kinetic power extraction on time-dependent estuaries,” *Proc. IMechE Vol. 222 Part A: J. Power and Energy*, vol. 222, pp. 471–484, 2008.
- [77] B. Polagye, M. Kawase, and P. Malte, “In-stream tidal energy potential of puget sound, washington,” *Proc. IMechE Vol. 223 Part A: J. Power and Energy*, vol. 223, pp. 571–587, 2009. [59](#)
- [78] C. Garrett and P. Cummins, “Generating power from tidal currents,” *Journal of waterway, port, coastal and ocean engineering*, vol. 130-3, pp. 114–118, 2004. [59](#), [60](#)
- [79] J. Blanchfield, C. Garrett, P. Wild, and A. Rowe, “The extractable power from a channel linking a bay to the open ocean,” *Proc. IMechE Vol. 222 Part A: J. Power and Energy*, vol. 222, pp. 289–297, 2008. [59](#), [60](#)
- [80] C. Garrett and P. Cummins, “The power potential of tidal currents in channels,” in *The Royal Society A*, 2005. [60](#), [61](#)

- [81] J. Blanchfield, C. Garrett, A. Rowe, and P. Wild, “Tidal stream power resource assessment for masset sound, haida gwaii,” *Proc. IMechE Vol. 222 Part A: J. Power and Energy*, vol. 222, pp. 485–492, 2008. 62
- [82] F. Dupont, C. Hannah, and D. Greenberg, “Modelling the sea level of the upper bay of fundy,” *Atmosphere-Ocean*, vol. 43, pp. 33–47, 2005. 62
- [83] Sea Generation Ltd. Marine Current Turbines, “Seagen fact sheet.” Online: <http://www.seageneration.co.uk/downloads.asp>. Accessed: June 2010. 75
- [84] F. White, *Fluid Mechanics*. McGraw Hill, 2003. 75, 76
- [85] M. Shives and C. Crawford, “Mesh and load distribution requirements for actuator line cfd simulations,” 2011. Submitted to Wind Energy, Sep. 2011. 120
- [86] M. Shives and C. Crawford, “Evaluation of discrete blade effects for ducted turbines using an actuator-line cfd method.” *In preparation*, 2011. 120

Appendix A

Turbine Optimization Code

This appendix contains the Matlab code used for optimizing turbines for an arbitrary blockage ratio as described in section 2.6.9. The main function (called AUTORUN.m) is given first, followed by the post processing .cse files needed to run the program.

A.1 AUTORUN.m

```
function OPT=AUTORUN_4(Cnu,CT,TSR,BR)
% initial guess
    Cnu_ini=Cnu;
    TSR_ini=TSR;
    CT_ini=CT;
% step sizes
    dCnu=0.1; Cnu_tol=0.05;
    dTSR=0.5; TSR_tol=0.25;
    dCT=0.05; CT_tol=0.025;
%Define limit on tidal amplitude response
    DeltaR_max=0.05; %5 percent change

    history=[];
%iterate...
    done=0;
    while ~done
    %% CT
        % run first case
        [dat,obj,DR]=run_case(Cnu,TSR,CT,BR);
        data = dat;
        objt = obj;
        DeltaR = DR;

        % run second case
        CT=CT+dCT; %perturb CT
        [dat,obj,DR]=run_case(Cnu,TSR,CT,BR); %run case
        data(end+1,:)= dat;
```

```

objt(end+1) = obj;
DeltaR(end+1) = DR;

%set search direction
[doneCT,CT,drn]=findDrn(DeltaR,DeltaR_max,objt,CT,dCT);
% set oldMax
oldMax=max([objt(DeltaR<DeltaR_max) 0]);

%loop until objt is bracketed
while ~doneCT
    CT=CT+drn*dCT;
    [dat,obj,DR]=run_case(Cnu,TSR,CT,BR); %run case
    data(end+1,:)= dat
    objt(end+1)= obj;
    DeltaR(end+1)=DR;
    %check for bracketing of max
    newMax=max([objt(DeltaR<DeltaR_max) 0])
    if newMax==oldMax && newMax~=0;
        doneCT=1;
    end
    oldMax=newMax;
end
history=[history; data];
save('history','history');
[~,ind]=find(objt==oldMax);
CT=data(ind,2);

%% TSR
clear data objt DeltaR

% run first case
[dat,obj,DR]=run_case(Cnu,TSR,CT,BR);
data = dat;
objt = obj;
DeltaR = DR;

% run second case
TSR=TSR+dTSR; %perturb TSR
[dat,obj,DR]=run_case(Cnu,TSR,CT,BR); %run case
data(end+1,:)= dat
objt(end+1) = obj;
DeltaR(end+1) = DR;

%set search direction
[doneTSR,TSR,drn]=findDrn(DeltaR,DeltaR_max,objt,TSR,dTSR);
% set oldMax
oldMax=max([objt(DeltaR<DeltaR_max) 0]);

%loop until objt is bracketed
while ~doneTSR
    TSR=TSR+drn*dTSR;
    [dat,obj,DR]=run_case(Cnu,TSR,CT,BR); %run case
    data(end+1,:)= dat
    objt(end+1)= obj;
    DeltaR(end+1)=DR;
    %check for bracketing of max
    newMax=max([objt(DeltaR<DeltaR_max) 0])
    if newMax==oldMax && newMax~=0;
        doneTSR=1;
    end
end

```

```

        end
        oldMax=newMax;
    end

    history=[history; data];
    save('history','history');
    [~,ind]=find(objt==oldMax);
    TSR=data(ind,4);

%% Cnu

    clear data objt DeltaR

    % run first case
    [dat,obj,DR]=run_case(Cnu,TSR,CT,BR);
    data = dat;
    objt = obj;
    DeltaR = DR;

    % run second case
    Cnu=Cnu+dCnu; %perturb TSR
    [dat,obj,DR]=run_case(Cnu,TSR,CT,BR); %run case
    data(end+1,:)= dat
    objt(end+1) = obj;
    DeltaR(end+1) = DR;

    %set search direction
    [doneCnu,Cnu,drn]=findDrn(DeltaR,DeltaR_max,objt,Cnu,dCnu);
    % set oldMax
    oldMax=max([objt(DeltaR<DeltaR_max) 0]);

%loop until objt is bracketed
while ~doneCnu
    Cnu=Cnu+drn*dCnu;
    [dat,obj,DR]=run_case(Cnu,TSR,CT,BR); %run case
    data(end+1,:)= dat
    objt(end+1)= obj;
    DeltaR(end+1)=DR;
    %check for bracketing of max
    newMax=max([objt(DeltaR<DeltaR_max) 0])
    if newMax==oldMax && newMax~=0;
        doneCnu=1;
    end
    oldMax=newMax;
end
[ObjMax,ind]=find(objt==oldMax);
Cnu=data(ind,1);
history=[history; data];
save('history','history');
%% Test for overall convergence
clear data objt DeltaR
sprintf(' Cnu=%3.3f CT=%3.3f TSR=%3.3f',Cnu,CT,TSR)
sprintf('Cnu_ini=%3.3f CT_ini=%3.3f TSR_ini=%3.3f',Cnu_ini,CT_ini,TSR_ini)
if abs(Cnu-Cnu_ini)<Cnu_tol && abs(CT_ini-CT)<CT_tol &&
    abs(TSR_ini-TSR)<TSR_tol
    done=1;
else
    %update initial guess for next loop
    CT_ini=CT;

```

```

        TSR_ini=TSR;
        Cnu_ini=Cnu;
    end
end
export_blade(Cnu,TSR,CT);
OPT=[Cnu CT TSR ObjMax];
end

function [Cpmax Pmax]=fit_data(C,P)
    if length(C)==3
        ft_ = fittype('poly2');
    elseif length(C)==4
        ft_ = fittype('poly3');
    elseif length(C)>4
        ft_ = fittype('poly4');
    end
    cf_ = fit(C,P,ft_);
    Cfit=linspace(min(C),max(C),1000);
    Pfit=cf_(Cfit);
    figure(1)
    plot(C,P,'.'); hold on
    plot(cf_,'fit',0.95); hold off
    [Pmax ind]=max(Pfit);
    Cpmax=Cfit(ind);
end

function [doneV,V,drn]=findDrn(DeltaR,DeltaR_max,objt,V,dV)
    doneV=0;
    drn=1;
    if all(DeltaR<DeltaR_max) %both points are below the limit on DR
        if objt(2)<objt(1)
            drn=-1; %(search toward increasing objective)
            V=V-dV; %go back to initial V
        end
    elseif all(DeltaR>DeltaR_max) % both points are above the limit on DR;
        if DeltaR(2)>DeltaR(1)
            drn=-1; % search toward decreasing DR
            V=V-dV; %go back to initial CT
        end
    else % stradling the limit
        if sign(DeltaR(2)-DeltaR(1))==sign(objt(2)-objt(1))
            doneV=1;
        else
            if objt(2)<objt(1)
                drn=-1; %(search toward increasing objective)
                V=V-dV; %go back to initial CT
            end
        end
    end
end

function [L]=is_bracketed(C,Obj,limit,drn)
    if drn==1
        if all(limit==0)
            [~,ind]=max(Obj);
            ObjMax=C(ind);
            if any(C<ObjMax) && any(C>ObjMax)
                L=1;
            end
        elseif all(limit==1)
            disp('search direction is infeasible...terminating')
        end
    end
end

```

```

        return
    else
        L=1; %stop searching because we've hit the limit.
    end
else %drn=-1
    if all(limit==1)
        L=0; % keep going because we need to get below the limit.
    elseif all(limit==0) % this happens when we start above the maximum...
        %...but below the limit.

        %test for a peak...
        [~,ind]=max(Obj);
        ObjMax=C(ind);
        if any(C<ObjMax) && any(C>ObjMax)
            L=1;
        end
    else % we started above the limit, and now are below it.
        % if the function is decreasing with further iteration, we
        % stop.
        if Obj(end)<Obj(end-1)
            L=1; %stop
        else % If it is increasing we continue until a peak.
            L=0; %continue
        end
    end
end
end
end
function export_blade(Cnu,TSR,CT)
    make_export(Cnu,TSR,CT);
    dos('Export')
end
function [dat,obj,DeltaR]=run_case(Cnu,TSR,CT,BR)
    make_ccl(Cnu,TSR,CT);
    make_bat(Cnu,TSR,CT);
    name=sprintf('D1_F%5.4f_CT%5.4f_TSR%5.4f.res',[Cnu CT TSR])
    if ~exist(name)
        dos('Run')
    end
end

dos('Process')
[dat]=read_output();
CT=dat(3);
CPt=dat(5);
CPq=dat(6);
CD=dat(7);

%channel model.

A3_A4=0.6731;
Ac=3.1e5;
%   Ar=BR*Ac*A3_A4;
ab=5.30;
a=4.71;
rho=1024;
Q0=7.5e5;
g=9.81;
c=6.19E-2;
omega=1.4E-4;
beta=7.62;
P0=rho*g*a*Q0;

```

```

R0=ab/a;
NDdrag0=9.89;
NDdrag1=1.1*(CT+CD)*BR*A3_A4* 4/(3*pi)*g*a/(Ac*c*omega)^2;
NDdrag=NDdrag0+NDdrag1;
R=sqrt(2*beta^2 / ( (beta-1)^2+sqrt( (beta-1)^4+4*NDdrag^2 ) ) );
DeltaR=(R0-R)/R;
Pff=NDdrag1*R^3*P0/(2*R0*beta^2);
P=CPq/((CT+CD)*1.1)*Pff;
format short g
dat=[dat P Pff DeltaR];
obj=P;
end

function [dat]=read_output()
fid=fopen('output.txt');
dat = textscan(fid,'%f%f%f%f%f%f','Delimiter',' ',' ','CollectOutput',1);
dat=dat{1};
fclose(fid);
end
function make_ccl(Cnu,TSR,CT)
fid=fopen('params.ccl','wt');
fprintf(fid,'LIBRARY:\n');
fprintf(fid,' CEL:\n');
fprintf(fid,' EXPRESSIONS:\n');
fprintf(fid,' F = %f\n',Cnu);
fprintf(fid,' TSR = %f\n',TSR);
fprintf(fid,' CT = %f\n',CT);
fprintf(fid,' END\n');
fprintf(fid,' END\n');
fprintf(fid,'END\n');
fprintf(fid,'COMMAND FILE:\n');
fprintf(fid,' Version = 12.0.1\n');
fprintf(fid,'END\n');
fclose(fid);
end

function make_export(Cnu,TSR,CT)
fid=fopen('Export.bat','wt');
CFXpath='C:\Program Files\ANSYS Inc\v120\CFX\bin\cfdpost';
command='-batch output_blade.cse D1_F%5.4f_CT%5.4f_TSR%5.4f.res ';
fprintf(fid,[CFXpath command],[Cnu CT TSR]);
fclose(fid);
end

function make_bat(Cnu,TSR,CT)
fid=fopen('Run.bat','wt');
CFXpath='C:\Program Files\ANSYS Inc\v120\CFX\bin\cfx5solve';
str1='-def D1.def -par-local -partition 4 -ccl params.ccl';
str2='-fullname D1_F%5.4f_CT%5.4f_TSR%5.4f';
command= [str1 str2];
fprintf(fid, [CFXpath command],[Cnu CT TSR]);
fclose(fid);
fid=fopen('Process.bat','wt');
CFXpath='C:\Program Files\ANSYS Inc\v120\CFX\bin\cfdpost';
command='-batch process.cse D1_F%5.4f_CT%5.4f_TSR%5.4f.res';
fprintf(fid,[CFXpath command],[Cnu CT TSR]);
fclose(fid);
end

```

A.2 process_header.cse

```

COMMAND FILE:
  CFX Post Version = 12.0
END

# Output header info "Output.txt" file.
! $file = 'output_LAWN.txt';
! open(INFO, ">$file");          # Open for output
! print INFO "A_0, A_1, A_2, A_25, A_3, A_4, A_5, A_6 ," ; # streamtube areas
! print INFO "u_0, u_1, u_2, u_25, u_3, u_4, u_5, u_6 ," ; # u velocities
! print INFO "V_0, V_1, V_2, V_25, V_3, V_4, V_5, V_6 ," ; # V velocities
! print INFO "p_0, p_1, p_2, p_25, p_3, p_4, p_5, p_6 ," ; # pressures
! print INFO "p_tot_0, p_tot_1 ,p_tot_2, p_tot_25 ,p_tot_3, p_tot_4 , p_tot_5...
... , p_tot_6 ," ;
! print INFO "E_0, E_1, E_2, E_25, E_3, E_4 , E_5 , E_6 \n " ; # Energy
! close(INFO);

```

A.3 process.cse

```

COMMAND FILE:
  CFX Post Version = 12.0
END

LIBRARY:
CEL:
  EXPRESSIONS:
    DiskArea = 1/60*pi*(Rmax^2-Rmin^2)
    DiskXave = volumeAve(X)@DISK
    PThrust = volumeInt(-User Momentum Source.Bforce X*Velocity u)@Domain 1
    PThrustCoeff = PThrust/(.5*rho*Uo^3*DiskArea)
    PTorque = volumeInt(-User Momentum Source.Bforce Theta*radius*omega)@Domain 1
    PTorqueCoeff = PTorque/(.5*rho*Uo^3*DiskArea)
    UserFtheta = -User Momentum Source.Bforce Y *z/radius + User Momentum ...
... Source.Bforce Z * y/radius
    Rmax = maxVal(radius)@DISK
    Rmin = minVal(radius)@DISK
    radius = sqrt(y^2+z^2)
    uTheta = -Velocity v *(z/radius) + Velocity w*(y/radius)
    uR = Velocity v *(y/radius) + Velocity w*(z/radius)
    Drag = force_x()@Duct
    DragCoeff = Drag/(.5*rho*Uo^2*DiskArea)
    phi=atan(Velocity u / (r*omega-uTheta))
    ww = sqrt(Velocity u^2 + (radius*omega-uTheta)^2 )
  END
END
END

USER SCALAR VARIABLE: r
  Expression = radius
  Recipe = Expression
END

USER SCALAR VARIABLE: User Momentum Source.Bforce Theta
  Expression = UserFtheta
  Recipe = Expression

```

```

END

USER SCALAR VARIABLE: Phi
  Expression = phi
  Recipe = Expression
END

USER SCALAR VARIABLE: WW
  Expression = ww
  Recipe = Expression
END

USER SCALAR VARIABLE: DCPtorque
  Expression = dCptrq
  Recipe = Expression
END

USER SCALAR VARIABLE: DCPthrust
  Expression = dCpthr
  Recipe = Expression
END

USER SCALAR VARIABLE: Vtheta
  Boundary Values = Conservative
  Calculate Global Range = On
  Component Index = 1
  Expression = uTheta
  Recipe = Expression
  User Units =
  Variable =
  Variable to Copy = Pressure
  Variable to Gradient = Pressure
END

USER SCALAR VARIABLE: Vr
  Boundary Values = Conservative
  Calculate Global Range = On
  Component Index = 1
  Expression = uR
  Recipe = Expression
  User Units =
  Variable =
  Variable to Copy = Pressure
  Variable to Gradient = Pressure
END

! ($x_disk_centre) = evaluate( "volumeAve(X)\@DISK" );
! ($x_disk_min) = evaluate( "minVal(X)\@DISK");
! ($x_disk_max) = evaluate( "maxVal(X)\@DISK");
! ($r_disk_max)= evaluate( "maxVal(r)\@DISK" );
! ($r_disk_min)= evaluate( "minVal(r)\@DISK" );
! ($x_duct_max) = evaluate( "maxVal(X)\@Duct");

# STEP 2: Calculate all the necessary Variables:
! $pi= 3.14159265;
! ($CT_Spec) = evaluate("CT");
! ($TSR) = evaluate("TSR");
! ($A_Disk) = evaluate("DiskArea");
! ($CT_Int) = evaluate("volumeInt(-User Momentum Source.Bforce X)...

```

```

... \@Domain 1/ (0.5 * rho*Uo^2*$A_Disk));
! ($Cp_thrust) = evaluate("PThrustCoeff");
! ($Cp_torque) = evaluate("PTorqueCoeff");
! ($Uo) = evaluate("Uo");
! ($rho) = evaluate("rho");
! ($Cd) = evaluate("DragCoeff");
! ($F) = evaluate("F");

# Output all calculated variables to "output.txt" file.
! $file = 'output.txt';
! open(INFO, ">$file"); # Open for output
! print INFO "$F, $CT_Spec, $CT_Int, $TSR, $Cp_thrust, $Cp_torque, $Cd \n";
! close(INFO);

```

A.4 output_blade.cse

COMMAND FILE:

```

CFX Post Version = 12.0
END

```

LIBRARY:

```

CEL:
  EXPRESSIONS:
    DiskArea = 1/60*pi*(Rmax^2-Rmin^2)
    DiskXave = volumeAve(X)@DISK
    PThrust = volumeInt(-User Momentum Source.Bforce X*Velocity u)@Domain 1
    PThrustCoeff = PThrust/(.5*rho*Uo^3*DiskArea)
    PTorque = volumeInt(-User Momentum Source.Bforce Theta*radius*omega)@Domain 1
    PTorqueCoeff = PTorque/(.5*rho*Uo^3*DiskArea)
    UserFtheta = -User Momentum Source.Bforce Y *z/radius + ...
                ... User Momentum Source.Bforce Z * y/radius
    Rmax = maxVal(radius)@DISK
    Rmin = minVal(radius)@DISK
    radius = sqrt(y^2+z^2)
    uTheta = -Velocity v *(z/radius) + Velocity w*(y/radius)
    uR = Velocity v *(y/radius) + Velocity w*(z/radius)
    Drag = force_x()@Duct
    DragCoeff = Drag/(.5*rho*Uo^2*DiskArea)
    phi=atan(Velocity u / (r*omega-uTheta))
    ww = sqrt(Velocity u^2 + (radius*omega-uTheta)^2 )
  END
END
END

```

USER SCALAR VARIABLE: r

```

  Expression = radius
  Recipe = Expression
END

```

USER SCALAR VARIABLE: User Momentum Source.Bforce Theta

```

  Expression = UserFtheta
  Recipe = Expression
END

```

USER SCALAR VARIABLE: Phi

```

  Expression = phi

```

```

    Recipe = Expression
END

```

```

USER SCALAR VARIABLE: WW
    Expression = ww
    Recipe = Expression
END

```

```

USER SCALAR VARIABLE: Vtheta
    Boundary Values = Conservative
    Calculate Global Range = On
    Component Index = 1
    Expression = uTheta
    Recipe = Expression
    User Units =
    Variable =
    Variable to Copy = Pressure
    Variable to Gradient = Pressure
END

```

```

USER SCALAR VARIABLE: Vr
    Boundary Values = Conservative
    Calculate Global Range = On
    Component Index = 1
    Expression = uR
    Recipe = Expression
    User Units =
    Variable =
    Variable to Copy = Pressure
    Variable to Gradient = Pressure
END

```

```

! ($x_disk_centre) = evaluate( "volumeAve(X)\@DISK" );
! ($x_disk_min) = evaluate( "minVal(X)\@DISK" );
! ($x_disk_max) = evaluate( "maxVal(X)\@DISK" );
! ($r_disk_max)= evaluate( "maxVal(r)\@DISK" );
! ($r_disk_min)= evaluate( "minVal(r)\@DISK" );
! ($x_duct_max) = evaluate( "maxVal(X)\@Duct" );

```

```

LINE:Line 1
    Colour = 1, 1, 0
    Domain List = /DOMAIN GROUP:All Domains
    Line Type = Cut
    Line Width = 2
    Option = Two Points
    Point 1 = $x_disk_centre [m], $r_disk_min [m], 0.00001 [m]
    Point 2 = $x_disk_centre [m], $r_disk_max [m], 0.00001 [m]
END

```

```

! ($TSR) = evaluate("TSR");
!($str)="Line1_TSR_" . $TSR . ".csv";

```

```

EXPORT:
    Export Coord Frame = Global
    Export File = $str
    Export Geometry = On
    Export Type = Generic
    Export Units System = Current
    Export Variable Type = Hybrid

```

```
Include Header = On
Location List = Line 1
Null Token = null
Overwrite = On
Precision = 8
Separator = ", "
Spatial Variables = X,Y,Z
Variable List = Velocity u, Vtheta, Vr, Velocity, WW, Phi
Vector Brackets = ()
Vector Display = Scalar
END
>export
```